

Title	Real-time nondestructive methods for examining battery electrode materials
Authors	Grant, Alex;O'Dwyer, Colm
Publication date	2023-03
Original Citation	Grant, A. and O'Dwyer, C. (2023) 'Real-time nondestructive methods for examining battery electrode materials', Applied Physics Reviews, 10(1), 011312 (38pp). doi: 10.1063/5.0107386
Type of publication	Article (peer-reviewed)
Link to publisher's version	<a href="https://aip.scitation.org/doi/full/10.1063/5.0107386">https://aip.scitation.org/doi/full/10.1063/5.0107386</a> - 10.1063/5.0107386
Rights	© 2023, Author(s). All article content, except where otherwise noted, is licensed under a Creative Commons Attribution (CC BY) license ( <a href="http://creativecommons.org/licenses/by/4.0/">http://creativecommons.org/licenses/by/4.0/</a> ). - <a href="http://creativecommons.org/licenses/by/4.0/">http://creativecommons.org/licenses/by/4.0/</a>
Download date	2024-04-24 16:54:53
Item downloaded from	<a href="https://hdl.handle.net/10468/14292">https://hdl.handle.net/10468/14292</a>


# Real-time nondestructive methods for examining battery electrode materials <sup>F</sup>

Cite as: Appl. Phys. Rev. **10**, 011312 (2023); <https://doi.org/10.1063/5.0107386>

Submitted: 04 July 2022 • Accepted: 03 February 2023 • Published Online: 02 March 2023

 Alex Grant and  Colm O'Dwyer

## COLLECTIONS

 This paper was selected as Featured



View Online



Export Citation



CrossMark

## ARTICLES YOU MAY BE INTERESTED IN

[Effects of gas viscosity and liquid-to-gas density ratio on liquid jet atomization in crossflow](#)  
AIP Advances **13**, 035105 (2023); <https://doi.org/10.1063/5.0129696>

[Fully epitaxial, monolithic ScAlN/AlGaN/GaN ferroelectric HEMT](#)  
Applied Physics Letters **122**, 090601 (2023); <https://doi.org/10.1063/5.0143645>

[In-fiber interferometry sensors for refractive index](#)  
Applied Physics Reviews **10**, 011307 (2023); <https://doi.org/10.1063/5.0105147>



## Applied Physics Reviews

Special Topic: Materials and Technologies  
for Bioimaging and Biosensing

**Submit Today!**

# Real-time nondestructive methods for examining battery electrode materials

Cite as: Appl. Phys. Rev. **10**, 011312 (2023); doi: [10.1063/5.0107386](https://doi.org/10.1063/5.0107386)

Submitted: 4 July 2022 · Accepted: 3 February 2023 ·

Published Online: 2 March 2023



View Online



Export Citation



CrossMark

Alex Grant<sup>1</sup>  and Colm O'Dwyer<sup>1,2,a)</sup> 

## AFFILIATIONS

<sup>1</sup>School of Chemistry, Environmental Research Institute, and Tyndall National Institute, University College Cork, Cork T12 YN60, Ireland

<sup>2</sup>Advanced Materials and BioEngineering Research Centre, Trinity College Dublin, Dublin 2, Ireland

<sup>a)</sup>Author to whom correspondence should be addressed: [c.odwyer@ucc.ie](mailto:c.odwyer@ucc.ie) Tel.: +353 21 490 2732

## ABSTRACT

With the importance of Li-ion and emerging alternative batteries to our electric future, predicting new sustainable materials, electrolytes, and complete cells that safely provide high performance, long life, and energy dense capability is critically important. Understanding the interface, the microstructure of materials, and the nature of electrolytes and factors that affect or limit long-term performance is key to new battery chemistries, cell form factors, and alternative materials. The electrochemical processes that cause these changes are also difficult to probe because of their metastability and lifetimes, which can be of nanosecond to sub-nanosecond time domains. Consequently, developing and adapting high-resolution, nondestructive methods to capture these processes proves challenging, requiring state-of-the-art techniques. Recent progress is very promising, where optical spectroscopies, synchrotron radiation techniques, and energy-specific atom probe tomography and microscopy methods are just some of the approaches that are unraveling the true internal behavior of battery cells in real-time. In this review, we overview many of the most promising nondestructive methods developed in recent years to assess battery material properties, interfaces, processes, and reactions under operando conditions similar in electrodes and full cells.

© 2023 Author(s). All article content, except where otherwise noted, is licensed under a Creative Commons Attribution (CC BY) license (<http://creativecommons.org/licenses/by/4.0/>). <https://doi.org/10.1063/5.0107386>

## TABLE OF CONTENTS

I. INTRODUCTION	1	C. Tracking the optical signature of photonic crystal electrodes in real-time	18
II. HIGH ENERGY OPERANDO X-RAY METHODS FOR BATTERY ELECTRODE MATERIALS ANALYSIS	3	D. Internal sensing of battery response: Fiber Bragg grating (FBG) sensors and probes	21
A. Synchrotron x-ray diffraction (XRD)	3	VI. NUCLEAR MAGNETIC RESONANCE ANALYSES OF MASS SHIFTING IN BATTERY SYSTEMS	25
B. X-ray computed tomography (x-ray CT)	6	VII. ELECTROCHEMICAL-ACOUSTICS: LISTENING TO A BATTERY'S HEALTH	30
III. OPERANDO TRANSMISSION ELECTRON MICROSCOPY (TEM)	8	VIII. BATTERY OPERATION IN A DYNAMIC SERVICE ENVIRONMENT: BUILDING A SENSOR NETWORK	32
A. Cryo-TEM and the importance of sample preparation and stability	10	IX. CONCLUSIONS AND OUTLOOK: WHERE OPERANDO METHODS MATTER TO BATTERY DEVELOPMENT	33
IV. ATOM PROBE TOMOGRAPHY (APT): COMPOSITIONAL PROFILING OF ELECTRODE MATERIALS ATOM BY ATOM	11		
V. OPERANDO OPTICAL SPECTROSCOPIC METHODS	14		
A. <i>In situ</i> Raman scattering of phase changes in battery electrode materials	15		
B. <i>In situ</i> ATR-FTIR for probing electrolyte decomposition at the electrode/electrolyte interface	17		
		I. INTRODUCTION	
		Substantial progress in battery technology is essential if we are to succeed in an energy transition toward a more carbon-neutral, fossil-fuel-free society. Moving toward more sustainable energy harvesting and storage technologies that become part of a circular economy is	

essential. Materials sustainability will become an overriding factor in the years to come, conjointly with consumer demands that are ever-increasing. Under such a scenario, the production of Li-ion batteries is expanding considerably across the globe reviving the issue of finite Li<sup>1</sup> reserves, and the volume of critical raw materials such as cobalt and nickel as pertinent examples. This concern has driven researchers to explore new, potentially more sustainable chemistries, including N-ion,<sup>2,3</sup> metal–air chemistries Li(Na)–O<sub>2</sub>,<sup>4,5</sup> Li–S,<sup>6,7</sup> multivalent (Mg, Ca)<sup>8</sup> redox flow batteries (RFBs), and aqueous-based technologies.<sup>9</sup> Electrode degradation represents one of the important challenges to the development of rechargeable batteries. While the existence of this challenge is well known and widely researched, the electrochemical processes responsible are continually being examined and assessed.<sup>10–14</sup> Unsurprisingly, attempts to understand these processes have involved the analysis of the composite materials. Data of this nature have vastly improved the performance of batteries and the understanding of degradation processes. However, such research has been limited mainly to the study of electrode materials in isolation, i.e., before or after cycling, failing to capture short-lived or metastable processes. There is no surprise that a further understanding of battery materials requires their analysis during operation. These requirements call for state-of-the-art methodologies. Since 2008,<sup>15</sup> many studies have adopted such an approach with great success. However, as it becomes a necessity for batteries to be charged every day, the need for more power has grown at a rate far greater than the improvements made in battery capacity.<sup>16</sup>

New analytical methods and lab-scale capabilities for existing large-infrastructure techniques are needed to probe specific battery chemistries and speed up analysis, screening and prediction of behavior, performance, and safety for future electrification, so that new technologies can be brought to the market more rapidly to meet societal demands. Advances could include the development of remote, noninvasive, and passive *operando* techniques<sup>17</sup> to complement present battery management systems<sup>18</sup>—but a real impact would come from powerful methods that are accessible outside synchrotron facilities and operable in any lab. Right now, the consensus for small and electric vehicle (EV)-level batteries is that failures modes need to be tracked in real-time, and as such, many battery companies are investing in accessories for advanced *operando* methods for their new battery chemistries. A recent commentary in Ref. 19 deals exactly with this need.

Rather than just probing a single material, *operando* techniques have provided an understanding of how the various materials function cooperatively, particularly within the working battery. This has been particularly important for the understanding of the electrode/electrolyte interface. *Operando* imaging and spectroscopic techniques such as nuclear magnetic resonance (NMR),<sup>20</sup> MRI,<sup>21</sup> and electron paramagnetic resonance (EPR)<sup>22</sup> have recently enabled the visualization and quantification of Li (and Na) microstructures. While these measurements do not simultaneously address phase, structural changes, and material arrangement during charge–discharge, they nevertheless offer powerful insight into side reactions and surface chemistries of battery materials. Recently, Co *et al.* addressed the efficiency in charge passed in Sn and other electrode materials to address the issue of side reactions using *operando* NMR and neutron depth profiling to quantify the amount of alloyed or intercalated Li as a function of charge,<sup>23–25</sup> directly imaging the coulombic efficiency of the overall convoluted processes in the anode material. Methods for imaging the movement

of reaction fronts and reaction kinetics are becoming increasingly powerful. *In situ* high-resolution TEM<sup>26,27</sup> has been at the forefront of these advances, providing in-depth insight into interfacial processes and Li-driven local structural changes (for example, in SnO<sub>2</sub> and Si) with a much higher resolution than MRI methods. Significant advances in synchrotron methodologies have allowed spectroscopic, two-dimensional transmission x-ray microscopy, full three-dimensional tomographic reconstructions, and diffraction-based methods to be performed (such as Bragg coherent diffraction imaging), often in parallel; these have been used, for example, to track particle expansion with lithiation,<sup>28</sup> and the evolution of strains and movement of dislocations within particles.<sup>29</sup> If materials exhibit magnetic character, it is also feasible to monitor lithiation-induced changes to magnetic properties as a sensitive probe of charge–discharge dynamics in a few materials, and supercapacitive behavior in hybrid materials with ferromagnetic character.<sup>30,31</sup> Optical methods that probe index changes in materials that undergo intercalation/alloying vs pseudocapacitive charge storage and compensation mechanisms are also feasible in principle.

Insight into the phenomena that underlie the behavior and operation of energy storage materials and devices has the potential to significantly help as a basis for material selection, but to inform us on how materials behave under operating conditions and that influence on overall performance, safety, and longevity. It may generally provide a way of analyzing open questions and performance limitations including degradation mechanisms in a whole range of technologies including electrochromics, supercapacitors, solar cells, photoelectrochemical systems, or water splitting where light–matter interactions are essential. One important consideration in all analytical techniques, some of which are addressed in this review, is the importance of expertise in operation, processing, and interpretation of the data. A recent report on atom-probe tomographic analysis for Li-ion battery materials<sup>32</sup> is a recommended read, where it becomes clear how many parameters that are technique-specific need to be considered for any meaningful analysis of battery materials by such advanced, deeply-probing, and high-resolution methods. Artifacts abound, and expertise in instrumentation, acquisition, processing, and interpretation is critically important.

Figure 1 depicts some of the *operando* methods that have recently been developed over the last two decades and the method that spans the energy spectrum from x-rays through to very low frequency radio waves. Many new methods are being developed specifically for batteries, but the need to analyze important materials, interfaces, and electrochemical reactions seeded the research that led to new *operando* cells, synchrotron techniques, and analytical method assisted by powerful computational approaches, to smaller benchtop/laboratory systems that are also very powerful in their capability. The terms *ex situ*, *in situ*, and *operando* are used throughout this work to describe measurements of battery materials. *Ex situ* measurements involve cycling a cell, stopping the process at a specific state of charge (SOC), and extracting the electrode before measurement. For *in situ* measurements, data collection occurs without extracting the electrode. For *operando* measurements, data collection is performed during electrochemical cycling. *Operando* techniques can be considered a special case of *in situ*, with the two terms often being used interchangeably throughout the literature. In this review, the distinct differences between the two modalities are distinguished with detail on the usefulness of *operando* techniques.<sup>15,33</sup>



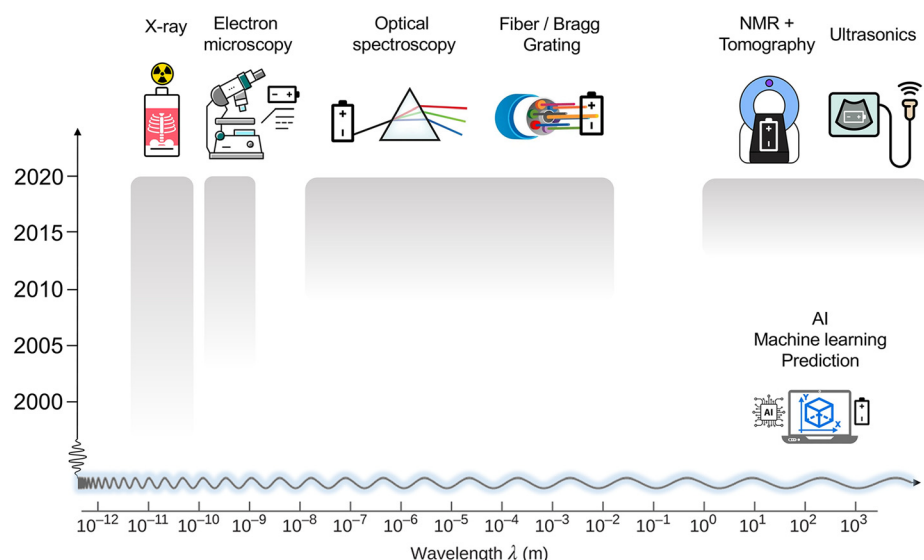


**FIG. 1.** Advancement of operando nondestructive method for examining batteries and battery materials in the last two decades. Specific references for many of these methods can be found throughout this review. Notably, the method spans the breadth of the electromagnetic spectrum, and since 2020, many of these techniques can be done in synchrotron facilities and in laboratory settings with benchtop-sized infrastructure. AI, machine learning, and computational prediction underpin much modern advancements to speed up discovery and troubleshoot potential issues prior to large-scale financial and time-investment.

The objective of this review is to give the reader a useful overview of some of the developments and usefulness of nondestructive methods we now have to examine battery electrode materials in real-time and to help battery researchers who are new to these techniques manage expectations by showing some of their requirements, capabilities, and limitations. We cover many techniques that span the photon energy range from x-rays to acoustic waves. Second, we summarize some promising initiatives and recent results related to battery materials and cell performance and health assessment in real-time. We have grouped techniques according to the region of the energy spectrum of the probing measurement that have been tasked to a range of materials and battery chemistries. Some of the central issues in the application of each technique are addressed, outlining cell assembly considerations, benefits and limitations, materials preparation, resolution/accuracy, and extracted information. This information may prove useful when considering operando measurements, particularly recently reported results but also the required methodology and the common pitfalls to avoid. For each nondestructive method described here, the progression toward useful operando measurement and understanding, and its combination with complementary analytical techniques to monitor the electrochemical processes occurring in electrochemical cells, is of vital importance to the development of the next generation of batteries.

## II. HIGH ENERGY OPERANDO X-RAY METHODS FOR BATTERY ELECTRODE MATERIALS ANALYSIS

### A. Synchrotron x-ray diffraction (XRD)

X-ray diffraction (XRD) is an analytical technique often used to obtain detailed information about the structure of crystalline materials, and the chemical and physical properties they possess. Battery electrode materials are very often crystalline, with highly ordered architectures that allow control of ion and electron transport throughout. As a result, XRD is a powerful technique for characterizing these materials when conducted and analyzed with due care and rigor for measurement and interpretation. Traditional lab-based XRD methods are useful for determining the phases of crystalline electrode materials. The

quality of the data can be evaluated by two primary variables. The signal to noise ratio (SNR) is affected by several properties but is primarily dependent on the intensity of the x-ray beam. The second is peak width, usually quantified using the full width half maximum (FWHM), which is a function of the beam diameter. Smaller beam diameters result in the reduction of the FWHM and sharper peaks. Synchrotron XRD proves to be a superior approach in its characterization capabilities, but requires large-scale facilities typically. Its superiority can be summarized by the four main advantages over the traditional lab-based approach: (1) Greater beam intensity creating more intense peaks with an improved signal to noise ratio (SNR), (2) higher collimation that reduces angular beam divergence and increases the monochromatic character of the beamline, (3) the degree to which the beam is parallel is improved which removes the need for focusing geometry that can be inaccurate at low angles, and (4) improved peak: background ratio for samples that produce background fluorescence, unlike the pre-sample monochromators often used in traditional setups. For operando battery measurements, where the target samples may be difficult to access due to cell components that can cause beam attenuation, the enhanced accuracy and response provided through the synchrotron approach is useful.

A variety of approaches can be taken in the application of XRD to battery systems in operando to examine electrode materials. The basic concept is to evaluate the change in diffraction pattern over time during electrochemical cycling. Such work has been performed for anode and cathode materials for lithium-ion systems<sup>34</sup> along with a range of potentially more sustainable battery chemistries including sodium-ion,<sup>35,36</sup> potassium-ion,<sup>37</sup> and lithium-sulfur.<sup>38,39</sup> In Kirshenbaum *et al.*,<sup>40,41</sup> the approach is taken a step further. Energy-dispersive x-ray diffraction (EDXRD) was used to gain insight into the composition of a Li/Ag<sub>2</sub>VP<sub>2</sub>O<sub>8</sub> cell. EDXRD is suitable for *in situ* analysis of materials due to its rapid data collection rate and fixed scattering angle, the latter allows for high-accuracy measurement of lattice parameters that are present in the material. In the study, *in situ* EDXRD is performed at two discharge rates and the non-discharged cell is combined with *ex situ* x-ray absorption spectroscopy (XAS)

measurements to determine the optimal conditions for a conductive network to be formed that results in spatial resolution of the electrochemical reduction process within the electrode inside an intact electrochemical cell.

The presence of heterogeneities in electrode materials is common, especially when mass loading is enhanced when incorporating structures with increased thickness. The spatial resolution of the EDXRD is acquired through the cross-section of the cell, perpendicular to the surface of the face-to-face electrode configuration, from the Li metal counter electrode through the electrolyte to the cathode. Given that a gradient in current density and lithium-ion flux is unavoidable, and that the phases of both electrode and electrolyte species are determined by the electrochemical reactions that often depend on the degree of lithium uptake, heterogeneity in the crystalline phases detected across the cell are expected. To improve measurement consistency, the measurements are performed at multiple locations across the width of the cell to identify any asymmetries which may be present.

Consequently, short-lived, metastable phases are monitored, which were not previously accessible. One of the most important aspects of the data here is the ability to track structure formation

within the cell materials. The EDXRD data provide insight into the locations at which different phases occur, with a tomographic-like profile of the cell, shown in Fig. 2. Using these data combined with impedance measurements, changes in battery resistance can be analyzed. The study of both the structural changes and impedance in the cell using electrochemical impedance spectroscopy (EIS) simultaneously during cycling enables rationalization of the changes in battery resistance, which determines the nature of the discharge mechanism. Compilation of these results provides an overview of the conductive pathways formed from reduction products and the impact on the discharge mechanism. The two techniques prove complementary and the relationships between cathode reduction, electrochemical cell discharge, and impedance are established.<sup>42,43</sup> Insight into the electrochemical and structural processes that can occur are gained with the determination of the conditions required for an optimal conductive network in the cathode and the elucidation of a rate-dependent discharge mechanism. The advantages of combining the data obtained from *ex situ* and *in situ* techniques are evident from the results.

As discussed by Kirshenbaum *et al.* above, *in situ* XRD provides the ability to detect certain phases that occur at different SOC's of a

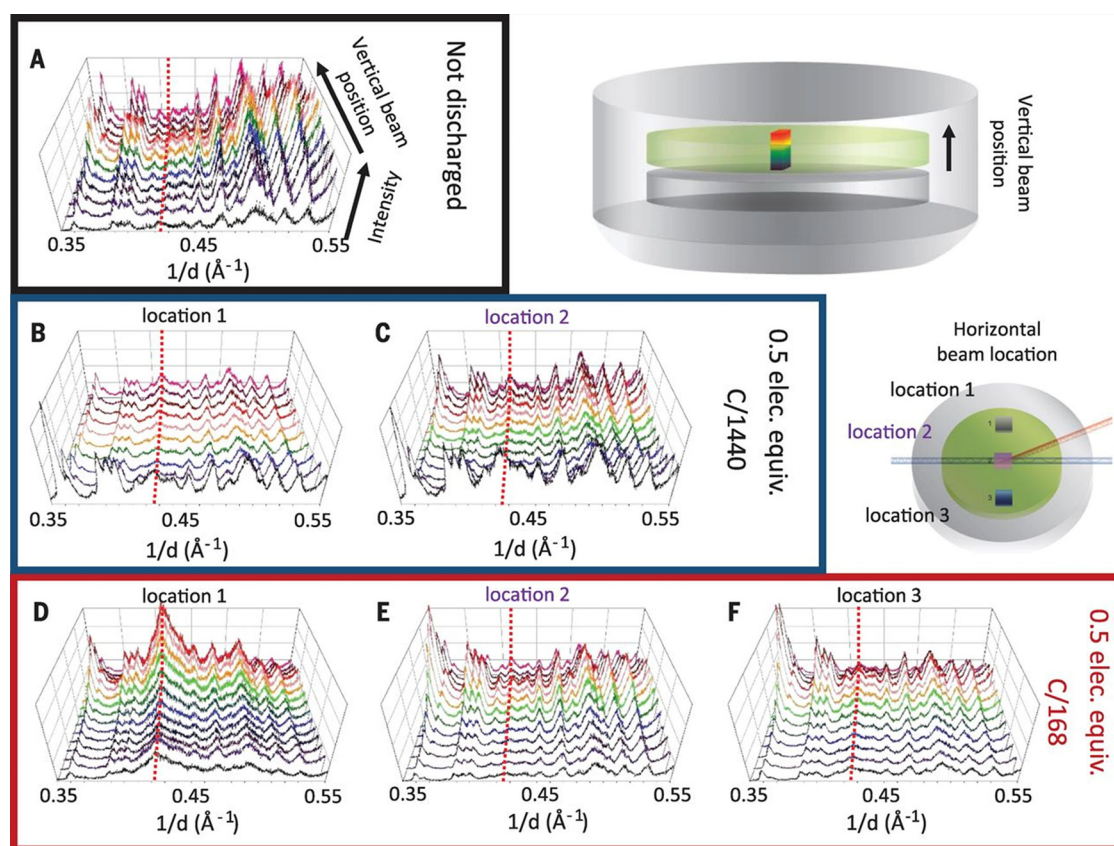


**FIG. 2.** Spectra resulting from spatially resolved *in situ* EDXRD measurements within three coin cells: (a) A non-discharged cell, (b) and (c) two different locations within a cell discharged to 0.5 electric equivalent at a rate of C/1440, and (d)–(f) three different locations within a cell discharged to 0.5 electric equivalent at a rate of C/168. Spectra were obtained every 20 mm through the cathode; for clarity, only half of the scans are presented in the figure. Spectra toward the top of the figure (red hues) were obtained within the side of the cathode closer to the stainless-steel coil cell top, and spectra toward the bottom of the figure (black hues) were obtained closer to the Li anode. Adapted with permission from Kirshenbaum *et al.*, *Science* **347**, 149 (2015). Copyright 2015 American Association for the Advancement of Science.

battery including material phases that are difficult or sometimes impossible to be reliably detected *ex situ* in a postmortem analysis after cell disassembly. However, the lifetimes of certain processes are shorter than the time taken to disassemble the cell and perform the required measurements and others are extremely sensitive to changes in their local environment, which can include access to changes in electrolyte, salt concentration (even when carefully contained in battery-grade storage environments) and especially to water and ambient air for more typical postmortem analyses.<sup>44</sup> Therefore, operando techniques are more useful in capturing this information. In Liu *et al.*,<sup>45</sup> operando XRD with high temporal resolution was used to analyze metastable structures formed during the high-rate cycling of  $\text{LiFePO}_4$  electrodes and determine the effects of strain vs compositional variation. These results are compared to simulated XRD patterns of some of the

structures predicted to form during cycling. Disagreement between data indicates the formation of metastable structures not detected *ex situ*, i.e., particles with lattice parameters that vary from the predicted composition. The results are also used to quantify the compositional variation during cycling. The operando XRD patterns (Fig. 3) show the absence of any particle interface (disappearance of Bragg reflections corresponding to second particle), indicating that strain effects did not occur. Based on work prior to this study, reactions in the electrode material were predicted to proceed via a process that would cause, using conventional wisdom, poor battery performance, while these measurements indicate the contrary. The utilization of operando XRD here provides the ability to explain this disagreement, by capturing processes that could not be detected previously using *ex situ* or even *in situ* methods.

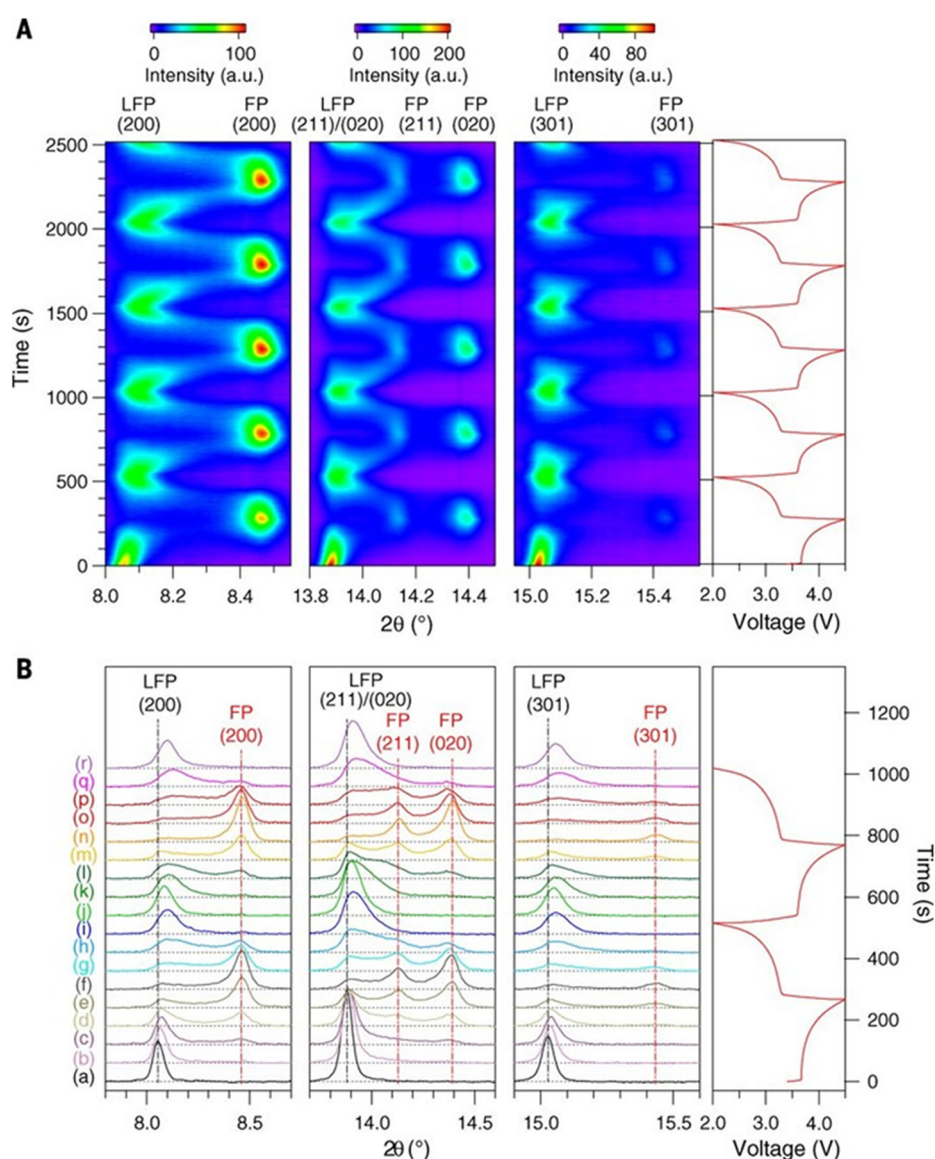


**FIG. 3.** *In situ* XRD patterns during galvanostatic charge and discharge at a rate of 10 C. (a) Diffraction patterns for (200), (211), (020), and (301) reflections during the first five charge-discharge cycles. The horizontal axis represents the selected  $2\theta$  regions, and time is on the vertical axis. Diffraction intensity is color coded with the scale bar shown on top. The corresponding voltage curve is plotted to the right. LFP,  $\text{LiFePO}_4$ ; FP,  $\text{FePO}_4$ . (b) Selected individual diffraction patterns during the first two cycles and voltage profile. The baseline is represented by horizontal dashed gray lines. Black vertical lines mark the positions of  $\text{LiFePO}_4$  peaks at the start of reaction; red vertical lines mark the position of  $\text{FePO}_4$  peaks formed during the first cycle. Reproduced with permission from Liu *et al.*, *Science* **344**, 1252817 (2014). Copyright 2014 American Association for the Advancement of Science.



## B. X-ray computed tomography (x-ray CT)

The operando synchrotron XRD discussed so far provides a host of useful information on battery electrode materials including the degree of crystallinity and lattice parameters of species with their evolution over time. Such information can be used to enhance understanding of how electrochemical cycling affects the constituent materials. However, the benefits of the application of x-ray microscopy to battery systems have provided the community with high-resolution models that stand as a clear visual representation of the constituent materials.

These models are provided in the form of tomographic profiling of the electrochemical cell. A considerable advantage of the microscopy approach is that it does not have to be performed in synchrotron facilities but can be incorporated into a lab setting. In Lu *et al.*, a novel x-ray nano-computed tomography (CT) dual-scan superimposition (DSS) technique is used to probe some of the key parameters of electrode materials that affect battery performance.<sup>46</sup> A 3D volume of a

Li-ion half-cell is reconstructed with an NMC111 cathode vs a Li metal anode, and achieved at the nanoscale. The study investigated how the structural characteristics of the cathode, such as porosity, tortuosity, and thickness, affected electrochemical processes within the cell such as SoL, electrolyte salt concentration ( $C_{\text{EY}}$ ), Li-ion flux, and charge transfer at different rates. Adaptations to the initial microstructure are also made to probe the evolution of the same electrochemical processes in novel microstructure designs.

Figure 4 shows the computed evolution of the half-cell during discharge at three different rates of 1.25, 2.5, and 5 C, from top row to bottom row. Each individual schematic depicts the half cell with current flow in the through-thickness direction. The top corresponds to the region of the cathode closest to the separator. The bottom represents the region closest to the current collector. Each column represents one of the key electrochemical parameters of the cell. In the first two columns of Fig. 4, SoL and electrolyte salt concentration of the cell at 50% depth of discharge (DoD) is shown. At the lowest rate, there is

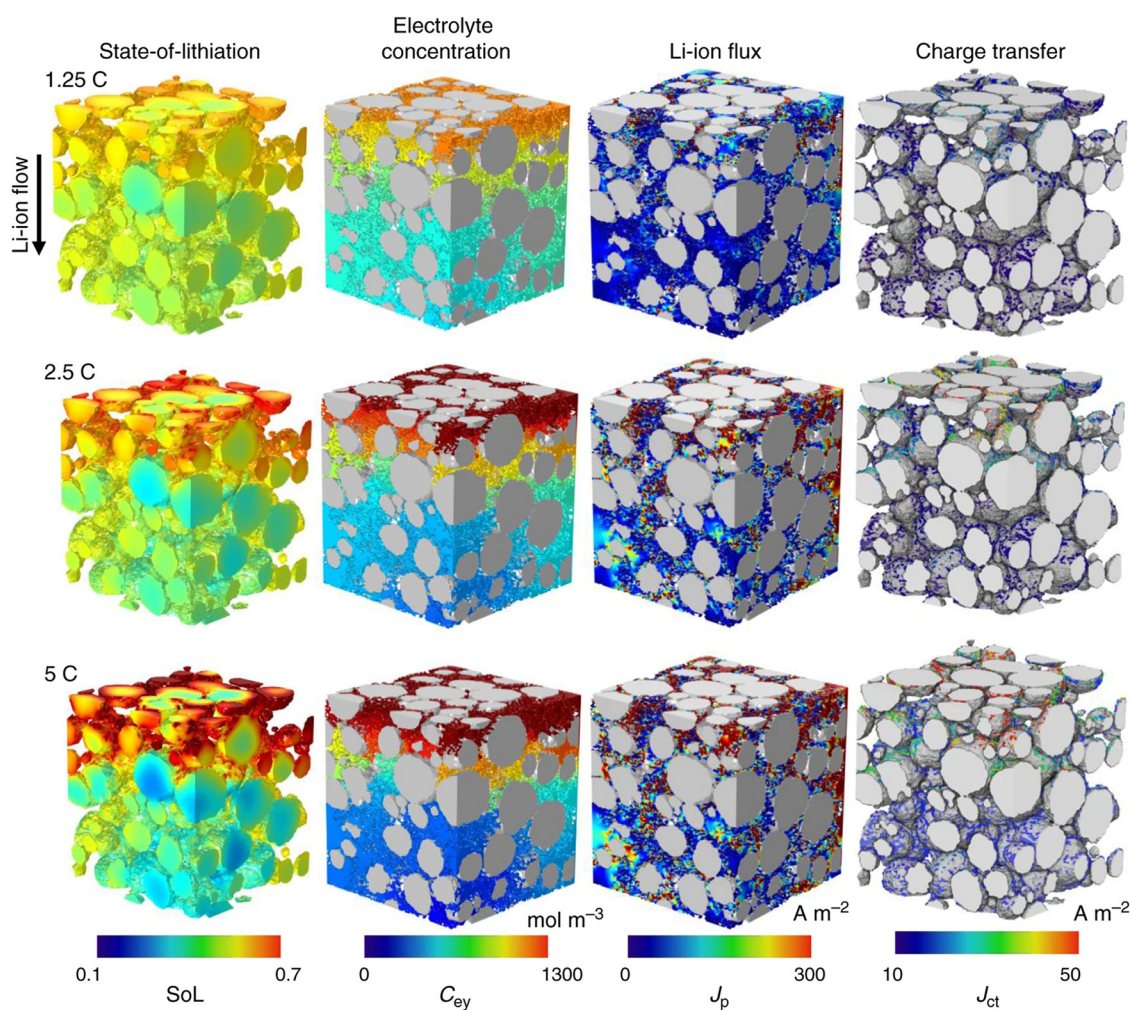


**FIG. 4.** Simulated discharge of the reconstructed cathode and an ideal lithium anode (half-cell) at 1.25, 2.5, and 5 C. The ionic current flows from the top (separator side) to the bottom (current collector side). Field variables at 50% depth-of-discharge (DoD) are shown here. Reproduced with permission from Lu *et al.*, Nat. Commun. **11**, 2079 (2020). Copyright 2020 authors, licensed under a Creative Commons Attribution (CC BY) License.

a uniform distribution observed in each case. As the rate is increased, a severe gradient develops due to the competition between mass transport dynamics and reaction kinetics. Lithiation occurs only where the active material, NMC particles in this case, are exposed to the Li ions in the electrolyte from Li salts. As the cell is discharged at low rates, the Li ions flow along the electrode slowly, maximizing the amount of active material they access. As the rate is increased, Li ions bombard the active material closest to the separator, maximizing charge transfer in this region. Consequently, mass transport is slow, meaning that the ions are unable to supply reactant into deeper regions of the electrode at a sufficient rate. NMC close to the current collector are therefore not utilized, resulting in severe capacity loss in the cell.

The third column shows the distribution of  $\text{Li}^+$  ion flux  $J_p$ . At low C-rates (1.25 C), the flux is evenly distributed. At higher C-rates (above 2.5 C), heterogeneity is evident due to the non-uniformity of the pore microstructures, with much higher flux in narrow pores. High flux causes local Ohmic heating, which can lead to electrolyte decomposition and thermal runaway. The fourth column shows the charge transfer  $J_{CT}$  which represents reactivity. The reactivity distribution is shown on a particle-by-particle basis, with reactivity more homogeneous at low C-rates.  $J_{CT}$  is much higher close to the separator than near the current collector, due to the mass transport limitation already mentioned.

The simulations based on the reconstructed cathode microstructure show that the inhomogeneous lithiation that occurs during cycling occurs primarily due to the broad distribution of particle size. As a result, changes in both the level of porosity and pore size in the direction of lithiation lead to a variation in lithium-ion diffusion path lengths. The imbalanced utilization of NMC lowers the energy density of the cell, which inhibits the long-term structural integrity of the electrode. Subsequent simulations were performed to investigate the use of next generation electrode designs, exploring the effects from the manipulation of particle size, pore size distribution, and electrode compression, to probe the effects of specific structural alterations to the performance of the cell.

A full interrogation of the causes of inhomogeneous lithiation based on the microstructural size distributions of the electrode and how this leads to poor battery performance is provided. The gradients of the electrolyte concentration and SoL increase with C-rate and depth of discharge, highlighting the issues that occur in battery performance at higher rates. It is particularly evident that particle size, pore size, and the level of porosity are the main factors that determine the distribution and direction of flow of lithium ions during discharge. Uneven intercalation between particles occurs as a result, leading to the underutilization of capacity and reduced power density. The study also describes the effects of calendaring on the microstructural evolution of the electrodes, a further look at the process can be found elsewhere.<sup>47</sup> Overall, the DSS computational technique and modeling used here represents a truly nondestructive method for investigating electrode degradation mechanisms based on the distribution of electrode particles within the cell.

Given that x-ray computed tomography has moved to the lab, analysis of battery materials' absorption coefficients is possible with voxel sizes down to  $\sim 50$  nm (a voxel is a single data point on a periodically spaced, three-dimensional grid and represents the material and local region properties in terms of their opacity to x-rays). The most recent approaches combine artificial intelligence and analysis

techniques including machine learning, with nano-CT on the lab scale. The motivation has been to develop powerful and accurate predictive models of the electrochemical response of battery materials and electrodes, from variations to microstructure and composition variations that can be visualized in 3D with postmortem analysis and predictive models for new materials or existing materials under various operando conditions. X-ray CT has superior resolution compared to nano-CT imaging, but developments in high-resolution nano-CT systems are under way. The technique is a nondestructive tool and provides opportunities for operando investigations in battery materials and solid-state battery interfaces and solid electrolytes, to name a few. Combining nano-CT imaging data and computational modeling, reconstructed volumes, and parameters such as pore tortuosity, particle size, etc. can be extracted and incorporated into the models to simulate electrochemical response. Machine learning and related approaches are necessary to obtain accurate and representative volume of the material under examination in CT images. Some recent reviews have outlined the details and opportunities of x-ray CT<sup>48,49</sup> and also computationally supported nano CT imaging<sup>48</sup> for battery research. The importance of data quality, interpretation, and curation is a consistent requirement in the application of CT imaging for battery materials analysis and extracting meaningful data requires careful workflow and data processing. Opportunities exist not only for 3D visualization but also for obtaining digital twins of battery electrodes to watch their behavior in real-time and translate this knowledge to the prediction of similar materials under different conditions, or for screening new materials of battery chemistries with particle size and interface-level resolution in real-time in 3D.

As a representative example, Scharf *et al.*<sup>49</sup> showed how *in situ* x-ray micro-CT in combination with electrochemical battery cell characterization could be used to interrogate how gassing at the current collector influence the performances of Zn-AgO batteries. Their results and process, representatively overviewed in Fig. 5, revealed that oxygen evolution reaction (OER) and hydrogen evolution reaction (HER) gas evolution depended on the choice of current collector material. While the likelihood of gas evolution processes could, in principle, be extracted from basic electrochemical knowledge of this metal in such an electrolyte, the micro-CT provided useful additional quantification on z-axis volumetric expansion within the electrode. Simply changing the current collector made an obvious improvement in performance giving a high cycling capacity of  $12.5 \text{ mA h cm}^{-2}$  for more than 325 cycles in a  $4 \text{ cm}^2$  form factor, corresponding to volumetric energy density of  $100.6 \text{ W h l}^{-1}$ . The development here of the *in situ* cells is also important for future application of micro-CT and related methods, as the cell construction is a necessity to allow accurate probing by CT instrumentation and they showed how the approach could provide meaningful examination of cell degradation over long-term cycling.

*In situ* and operando x-ray techniques represent a powerful array of tools that can be used to investigate the electrochemical behavior of battery electrode materials at different states of charge or discharge/during cycling with high energetic and spatial resolution. As most battery materials are crystalline, their examination using x-ray methods provides information on changes to their structure, which can be correlated with electrochemical processes and overall battery performance. The major disadvantage of this family of tools is their inability to detect amorphous phases, such as electrolyte species and some constituents of the solid electrolyte interphase (SEI) layer. Involving



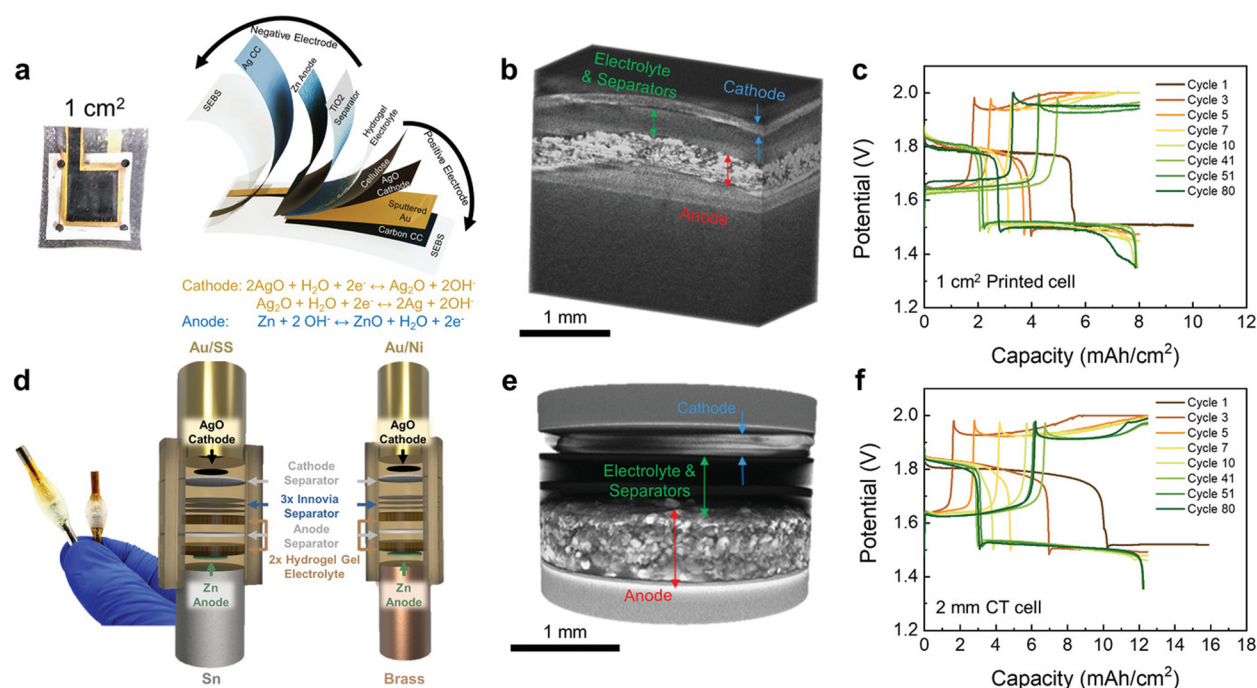


**FIG. 5.** Cell design and performance of a Zn-AgO printed cell (a) and *in situ* CT cell (d). 3D x-ray CT tomographic reconstructions (b) and (e), and electrochemical performance (c) and (f) for Zn-AgO printed cell (top row) and *in situ* CT cell (bottom row). Adapted with permission from Scharf *et al.*, *Adv. Energy Mater.* **11**, 2101327 (2021). Copyright 2017 Wiley-VCH.

computational methods to enable digital twins with accurate processing of the material volumes being imaged is essential so that examination of representative cells can provide predictive capabilities for new materials and batteries. For researchers investigating battery materials who wish to take advantage of the capabilities offered by operando x-ray methods, awareness of the benefits and some limitations are important for consistent and representative data. Table I is a summary of some of these key aspects. Establishment of the correct operando cell design is of paramount importance for obtaining consistent responses that represent the type of cell under investigation and to avoid artifacts in data or interpretation. In cross-cutting methodologies where the experience and approach in disciplines merge, data curation, interpretation, and application are as important as the careful experimental design and measurement. So too is the need for expertise in the measurements technique to ensure correct sample preparation, measurement conditions, data acquisition, instrument calibration, and more. From statistical principal component analysis of “data cubes,” to careful sample positioning and understanding of instrumental effects in x-ray data, such techniques are powerful for answering open questions for battery science when the expertise and the instrumentation together are applied to generate new knowledge.

### III. OPERANDO TRANSMISSION ELECTRON MICROSCOPY (TEM)

Operando methods for studying materials and processes in Li-ion batteries in a transmission electron microscope (TEM) since ca. 2012.<sup>57,58</sup> The initial open-cell holders allowed *in situ* measurements, and also some operando investigations under vacuum. Some of the

cell types were limited, requiring solid state electrolytes, or suffered from electron beam polymerization or damage, and others demonstrated the concept using materials that were somewhat atypical for Li-ion batteries (at least commercial or near-commercial chemistries). However, the technique proved to be useful in interrogating nanoscale and (in some cases) atomic-scale resolution of real-time changes to materials during discharging and charging, and readers are referred to some original papers and reviews.<sup>59</sup> A notable disadvantage of the open-cell method was the localized contact to the electrode, which limited the active mass involved in the electrochemical process. It did show new possibilities for investigating the interface in high resolution and spawned the development of closed cell operando TEM.

Closed-cell versions of cell holder for operando TEM were iteratively developed, with continuous improvement in capabilities to allow measurements with more common liquid electrolytes and electrode materials, while improving the sensitivity and contrast that was limited in earlier designs due to more severe electron scattering from metallic materials.<sup>60</sup> Liquid electrolytes in the TEM were developed by Muller *et al.* to have a flow electrolyte configuration<sup>61</sup> with a glassy carbon electrode, following from the silicon nitride membrane container approach for single Si nanowire (NW) measurements in the Si-Li metal cell demonstrated by Wang *et al.*<sup>62</sup> There were several other variations on the sealed liquid cell design for battery measurements (see Fig. 6) in the TEM, come including graphene instead of SiN<sub>x</sub> to reduce scattering and improve contrast in the materials under analysis, particularly when thick liquid electrolytes were used to generate more realistic comparison to the type of battery cell under consideration.<sup>63,64</sup> These closed cell variations for operando TEM revealed some useful



**TABLE I.** Overview of state-of-the-art *in situ* and operando x-ray techniques applied to battery systems, referencing the cell design and some of the key characteristics related to each technique. SOC = state of charge; DoD = depth of discharge.

Technique	Operando cell setup	Capabilities	Limitations	Local resolution
Synchrotron x-ray diffraction (XRD)	AMPIX cell <sup>45,50</sup> Tubular RATIX cell <sup>51</sup> Windowed coin cell <sup>52,53</sup> Li-O <sub>2</sub> capillary cell <sup>54</sup> Custom Li-S pouch cell <sup>55</sup>	Average structural information Crystallinity Phase purity  Atomic position Lattice parameter	Higher cost/access for routine measurements Requires standard reference data  Limited information for amorphous materials	0.01°
Synchrotron energy dispersive XRD (EDXRD)	Standard coin cell <sup>41,56</sup>	Tomographic profiling with depth of discharge Spatial resolution of species evolving during cycling Rapid data collection	Beam profile attenuated by coin cell steel casing Beam damage in constant data acquisition mode	<20 μm <sup>a</sup>
X-ray computed tomography (x-ray CT)	Computed reconstructions of target cell components <sup>46,48,49</sup>	Spatial resolution of: (i) Porosity (ii) Surface area (iii) Tortuosity (iv) Particle distribution (v) Charge transfer gradient (vi) State of lithiation (SOC/DoD)	Curation of “clean” data and precise interpretation necessary Detailed algorithms and various software packages required	~10 nm

<sup>a</sup>Spatial resolution in this case represents the sensitivity to which x-ray diffraction signals can be correlated with location within the electrode.

new insight into battery material behavior and high-resolution data on the nature of some important interfaces with the electrolyte. Real-time lithiation was observed using the important LiFePO<sub>4</sub> cathode material while dendrite growth, and Li stripping and

thinning mechanisms were observable using electron microscopy under charging and discharging conditions. Since then, many other findings have reported the detail of observations that readers can refer to for specifics.<sup>64</sup>

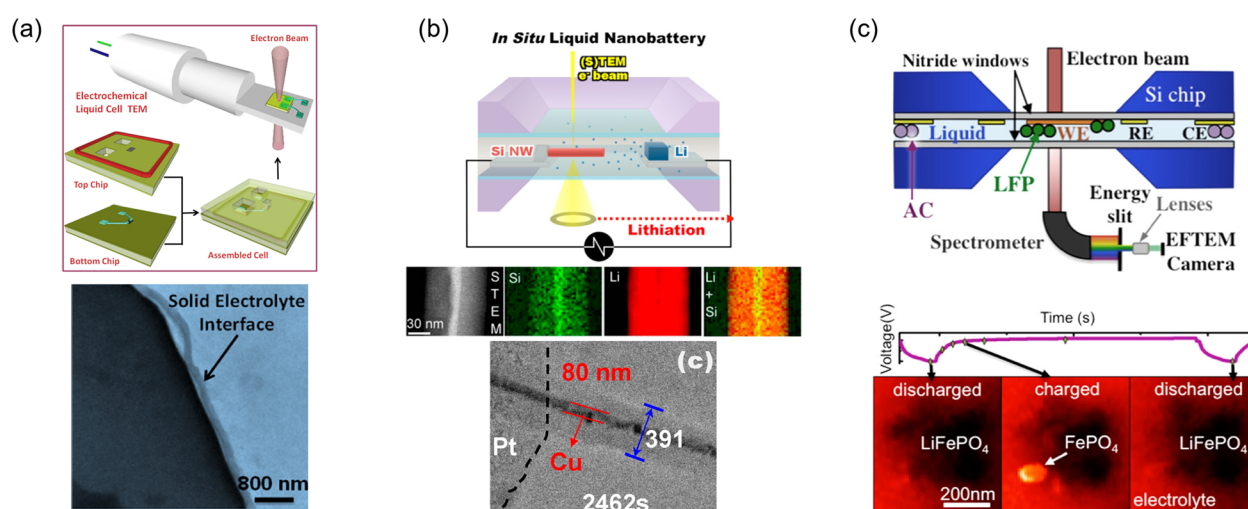


**FIG. 6.** (a) Setup for *in situ* liquid electrochemical cell to examine electrode–electrolyte interfaces. Adapted with permission from Zeng *et al.*, Nano Lett. **14**, 1745 (2014). Copyright 2014 American Chemical Society. (b) A liquid electrochemical operando cell (Si NW electrode) using SiN<sub>x</sub> membranes of ~50 nm in thickness to seal the liquid, while still allowing transmission of the high energy electrons for imaging. This liquid cell allowed elemental analysis and imaging of Li<sub>x</sub>Si around a Si NW electrode. Adapted with permission Gu *et al.*, from Nano Lett. **13**, 6106 (2013). Copyright 2013 American Chemical Society. (c) SiN<sub>x</sub> membraned liquid cell holder to allow operando EFTEM of LiFePO<sub>4</sub> cathodes. Adapted with permission from Holtz *et al.*, Nano Lett. **14**, 1453 (2014). Copyright 2014 American Chemical Society.

### A. Cryo-TEM and the importance of sample preparation and stability

Cryogenic electron microscopy, pioneered by Taylor and Glaeser<sup>65</sup> was originally developed to solve the challenge of beam and vacuum-sensitive biological cells and macromolecules. Dehydration and structure collapse are caused in vacuum, while certain features of biological and also sensitive battery materials required approaches to limit exposure to the electron beam. Before looking at some of the advances the cryo-TEM has offered, the beam-sensitivity issue had to be solved. Reducing beam power or electron density was key to preventing additional chemical processes on materials, at interfaces, and within certain electrolytes. To obtain a high SNR is also important, and to do this, the field adapted methods used in other fields to acquire movies containing thousands of short frame exposures at lower beam current. Often used in astronomical imaging for deep sky objects and for planetary imaging, the method known as “lucky imaging” involves the acquisition thousands of short exposures as movies with additive stacking algorithms used to integrate the final exposure to improve the SNR and mitigate beam damage or beam-induced modification to the materials-under-test. Wang *et al.* outlined an approach that details the steps from sample preparation (in this case electrodeposited lithium metal) to loading into the TEM, with caveats for the surface polishing of the active material deposited on grids for examination.

One pertinent example from Wang *et al.*, where cryo-EM was used to analyze the nature of Li metal anodes and SEI formation, in addition to cathode–electrolyte interphase (CEI) formation on  $\text{LiMn}_{1.5}\text{Ni}_{0.5}\text{O}_4$  cathode materials.<sup>66</sup> The technique avoided the problem

of Li reactivity under an electron beam.<sup>67</sup> This report showed an example of SEI on electrodeposited Li and tracked the morphology of the deposited Li and the crystalline lithium fluoride, oxide, and carbonates components of the SEI. Li *et al.* in 2017 showed a detail study of SEI formation and the nature of the dendrite structure using cryo-TEM<sup>68</sup> using a specially designed method to freeze the sample [Figs. 7(a) and 7(b)], and it was one of several papers analyzing the SEI this way that shed light on the link between the composition, crystallinity and morphology of this complex but critically important interfacial overlayer in Li-ion batteries. They directly observed the interactions of Li with the interphase and the growth of the dendrites that are very problematic in cells, due to short circuiting issues. Dendritic lithium ribbons exhibited crystalline structure [Figs. 7(c) and 7(d)], often with various termination crystallographic facets and formed kink defects during their growth. The morphology was dependent on the type of electrolyte additive used, and in the case of fluoroethylene carbonate (FEC), a more-ordered SEI nanostructure was formed, with a multilayered structures [Fig. 7(e)].<sup>69</sup> By comparison to directly imaged SEI at the lithium interface in standard electrolyte, they postulated that the stability often seen with FEC with some anodes is due to this mechanically more robust layered SEI structure, visible for the first time using cryo-EM. LiF known to improve cyclability is difficult to detect in electron microscopy, and efforts to image directly compound of lighter, lower scattering elements such as F, C, S, and O will help considerably in operando electron microscopy based techniques.

Corroborating measurements at cryogenic temperatures for reactive and sensitive materials is still important to ensure that the vitrified

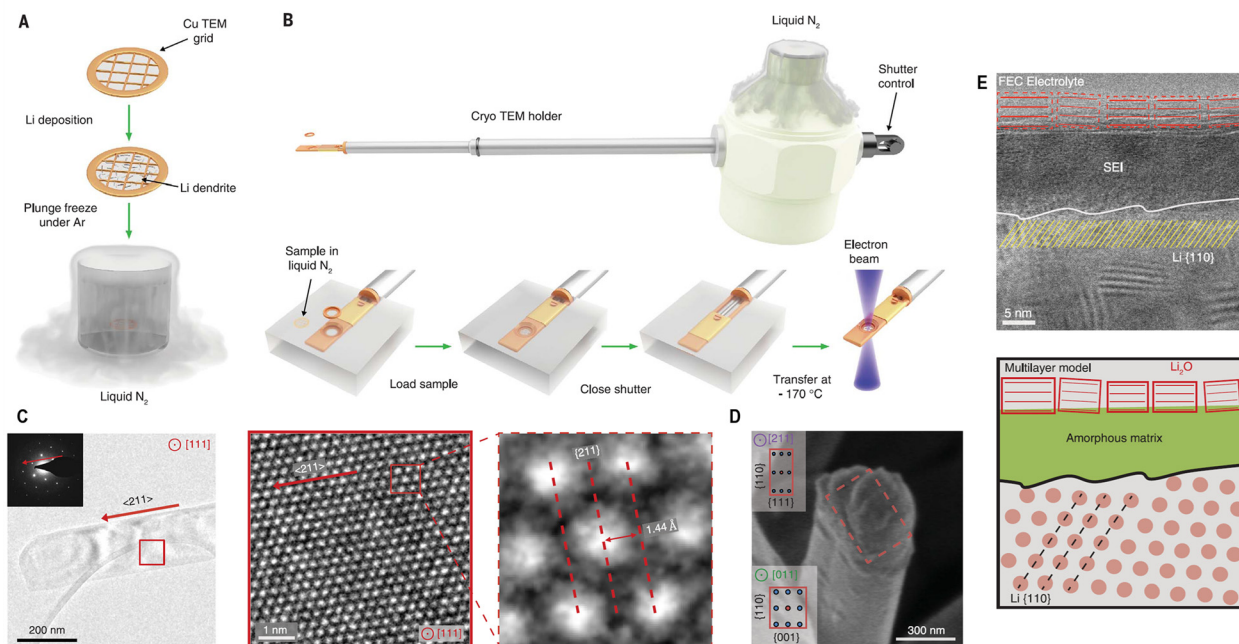


**FIG. 7.** (a) Setup where Li metal dendrites are electrochemically deposited directly onto a Cu TEM grid and then plunged into liquid nitrogen after battery disassembly. (b) The specimen is then placed onto the cryo-TEM holder in liquid nitrogen, kept isolated and at  $-170\text{ }^{\circ}\text{C}$ . (c) TEM of Li metal dendrites growing along the  $\langle 211 \rangle$  directions with corresponding SAED pattern (electron dose rate  $< 1\text{ e } \text{\AA}^{-2}\text{ s}^{-1}$  for  $\sim 30\text{ s}$ ). (d) Cross-sectional structure of a dendrite with faceting. The inset diagrams are atomic projections from  $[211]$  and  $[011]$  zone axes corresponding in shape to the cross-sectional structures from cryo-SEM. (e) Atomic-resolution image and schematic of the multilayered SEI structure on Li dendrites in FEC-containing electrolyte. Electron dose rate  $\sim 1000\text{ e } \text{\AA}^{-2}\text{ s}^{-1}$  for  $\sim 30\text{ s}$ . Adapted with permission from Li *et al.*, *Science* **358**, 506 (2017). Copyright 2017 American Association for the Advancement of Science.

and frozen material represents that of its room temperature counterpart and that no phase changes or other changes occur during cooling, and that operando measurements track processes that do occur in a cell. Cryo-TEM, cryo-FIB, and cryo-STEM have unveiled some important findings on Li metal anodes, sulfide cathodes, and SEI composition and the obtained data, so far, set clear requirements and sanity checks for electron microscopy/spectroscopy operando measurement in reactive setting, such as battery cells. However, electron-based operando methods may help identify various (and often elusive) lithium (super)oxide and polysulfide mechanisms in electrolytes and the changes in chemical speciation from electrolyte to surfaces using spectroscopic methods. Some of these requirements are consistent with other operando techniques, and correlation and consistency between reports will require fully detailed measurements parameters.

TEM methods for operando investigations will likely take on correlative approaches involving complementary techniques, such as tomography, holography, 4D TEM,<sup>70</sup> and others to probe not only the structure and compositions at various SOD or DOD, but to potentially watch, identify, and quantify fast (electro)chemical processes at the atomic scale. These developments will take time and likely be limited to certain material-electrolyte combinations. Very complex operando techniques that are developed with new modalities and tackle some of the limitations of earlier methods may prove to be warranted as new battery chemistries are proposed where a much shorter discovery-to-deployment timeframe is needed compared to Li-ion technology.

#### IV. ATOM PROBE TOMOGRAPHY (APT): COMPOSITIONAL PROFILING OF ELECTRODE MATERIALS ATOM BY ATOM

The techniques discussed thus far utilize x-ray and electron beam radiation, which can often result in instability in sensitive battery electrode materials due to beam damage. Atom probe tomography (APT) can be used for compositional mapping of materials in three dimensions with sub-nanometer resolution using an electric field. A combination of field ion microscopy (FIM) and time-of-flight mass spectrometry (TOFMS) permits single particle detection capabilities,<sup>71</sup> summarized in Fig. 8.

Unlike traditional microscopic methods where magnification is provided via the control of radiation paths, APT utilizes an electric field with a high curvature and is performed using either a straight flight-path instrument<sup>72</sup> or reflectron-fitted instrument.<sup>73</sup> Taking advantage of both microscopy and spectrometry, complementary information concerning both the atomic structure and atomic species of the specimen is provided.

APT is partially destructive in nature as the imaging and identification of the corresponding ion involves their removal from the surface of the specimen. However, given that APT can provide atomic scale information, surface destruction can be minimized, providing an accurate profile of the composition of the material under optimal conditions. The removal of atoms from the material is also beneficial, providing access of the atom probe to layers beneath the surface. APT is, therefore, not only a surface technique but can provide three-dimensional compositional profiling to volumes of  $10^3$ – $10^6$  nm<sup>3</sup>, corresponding to billions of atoms.<sup>74</sup>

Battery electrode materials tend to be a form of lithium-based metal oxide and are often semiconductors. Field evaporation process models were developed mainly for metals, but in the application of

APT to less conductive materials, the difference in regime must be accounted for. An in-depth overview of the concept and inception of APT, along with the challenges and limitations associated with its analysis of metals compared to less conductive materials, is provided elsewhere.<sup>71</sup> When the required electric field is applied in the atom probe, the reaction of the specimen is to shift its positive and negative charges to form an equal and opposite electric field, a process known as screening. For metals, the screening depth is typically less than 0.1 nm. As a result, only atoms at the actual surface experience the maximum electric field strength. For semiconductors, the screening depth is much greater, found to be  $\sim 2$  nm for silicon.<sup>75</sup> The change in depth is due to the lower number density of electrons, which is reduced by a factor of  $10^7$  that weakens the screening effect. The greater field penetration causes bending of the electron band structure (band bending). These effects become more pronounced for more electronically insulating materials. Given that the screening effect in semiconductors reduces their response to the high voltage pulsing of the electric field used to induce field ionization for APT, alterations are made.

Laser pulsing is incorporated to the setup when APT is applied to nonmetals. Given that the electronic response is not sufficient, the incident laser thermally activates the ionization process.<sup>76</sup> The temperature change induced by the laser pulse causes tunneling of electrons into the specimen surface while the corresponding positive ions are accelerated along the field lines to the detector. Unsurprisingly, laser pulsing has associated difficulties. A host of additional processes must then be considered, such as interactions between the laser beam and electric field, including absorption, carrier diffusion and recombination,<sup>77</sup> and thermal diffusion.<sup>78</sup> The increased field penetration depth for semiconducting metal oxides mean that sub-surface atoms are field evaporated, rather than just those at the actual surface that lowers the spatial resolution of the technique. The molecular structure of semiconducting materials also affects the resolution of APT.

Field evaporation of molecular ions and cluster ions occurs, particularly problematic for compound semiconductors such as oxides but can also occur in the monatomic case such as Ge, Si, and Sn. These clusters result in a high proportion of multiple events rather than the single event detection desired.<sup>79</sup> Field evaporation of molecular ions also causes their dissociation in the presence of the electric field. This results in neutral molecules, which go undetected by the atom probe, further affecting resolution.

The predominant issue in the application of APT to battery electrode materials is process-driven *in situ* delithiation, caused by the governance of the technique by an intense electric field. Most battery electrode materials are reactive metal oxides, so careful handling and transfer is required. Operando implementation of APT to battery systems has yet to be achieved, given the myriad of difficulties associated with the application of the technique to materials in general. Among these difficulties are the effects of the processes used in preparation of the specimens for analysis, along with the environment to which they are exposed during transport. Sample preparation is highly specific, usually performed using electropolishing or focused-ion beam methods. The specimen must be needle-shaped due to the curvature of the electric field.

A recent work used APT to probe pristine lithium-containing anode and cathode materials and addressed the efficacy of two of the conventions that are typically followed in its practice,<sup>32</sup> namely, cryogenic specimen preparation and the use of ultra-high vacuum (UHV)

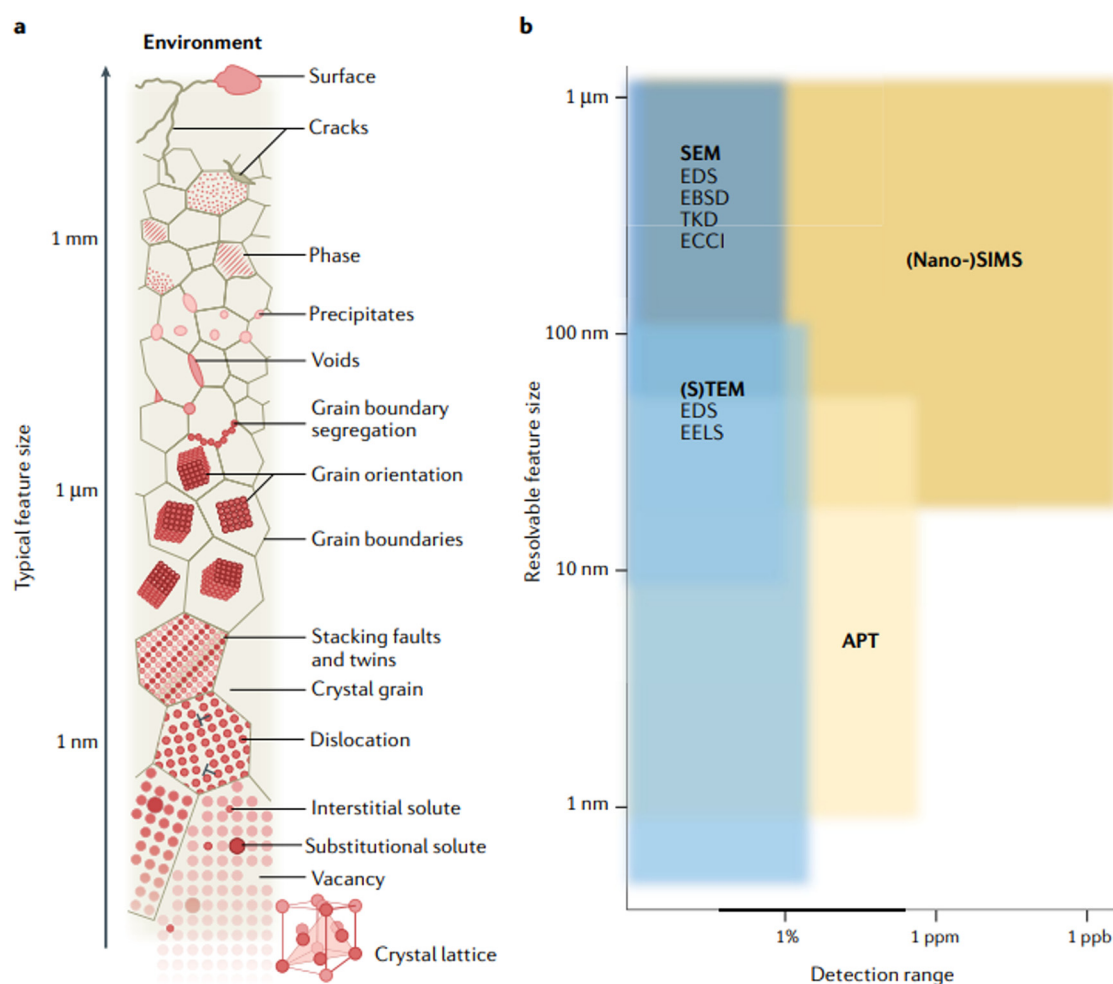


**FIG. 8.** Features of microstructured materials with their relative sizes and some analytical techniques used to resolve them. (a) A range of common structural features of interest, from the atomic arrangement of a crystal lattice, through a range of crystalline defects, phases, and grains, to imperfections at the surface. (b) Sensitivity and analyzable feature size for some structural analysis techniques. Atom probe tomography (APT); Electron backscattered diffraction (EBSD); Electron-channeling contrast imaging (ECCI); Energy-dispersive x-ray spectroscopy (EDS); Electron energy loss spectroscopy (EELS); Scanning electron microscopy (SEM); Secondary ion mass spectrometry (SIMS); (Scanning) transmission electron microscopy [(S)TEM]; Transmission Kikuchi diffraction (TKD). Reproduced with permission from Gault *et al.*, Nat. Rev. Methods Primers 1, 51 (2021). Copyright 2021 Springer Nature.

during transport. These conventions are followed due to the belief based that they mitigate some of the associated difficulties, primarily, unwanted *in situ* delithiation. Preparation methods and transport are performed with and without these difficulty-mitigating steps for several widely used electrode materials to assess their importance. The highly involved specimen preparation and experimental setup is detailed, specific to each material. APT is then performed under a range of experimental conditions for each of the materials. Figure 9(a) shows the 3D atomic composition profiles under a range of pulse energies and two different cryogenic temperatures. Significantly different composition profiles are generated in each case, indicating the importance of choosing the optimal preparation conditions. Figures 9(b) and 9(c) compare the effects of transport under UHV and in ambient air. Specimen transport in air resulted in lithium composition close to its nominal value, consistent along the full probe length of the

specimen while those specimens transported under UHV resulted in a non-uniform composition profile that fluctuated much further from the nominal value. The results prove that previously established transport conventions are not completely reliable. UHV transport is typically used to prevent the adsorption of atmospheric species onto the surface of the specimen, which can occur very quickly. For example, a single layer of  $O_2$  can adsorb onto the surface of reactive metals in less than 0.3 s while adsorption can take up to 70 days under UHV conditions. However, the efficacy of the UHV can be questioned here due to evidence in results from this investigation which show that both naturally occurring intrinsic shielding and intentional extrinsic shielding can enhance protection from the electric field. The adsorbed species under ambient conditions may act as a shield from the electrostatic field of the probe and prevent field penetration. The aforementioned lithium migration is the primary challenge inherent to the analysis of



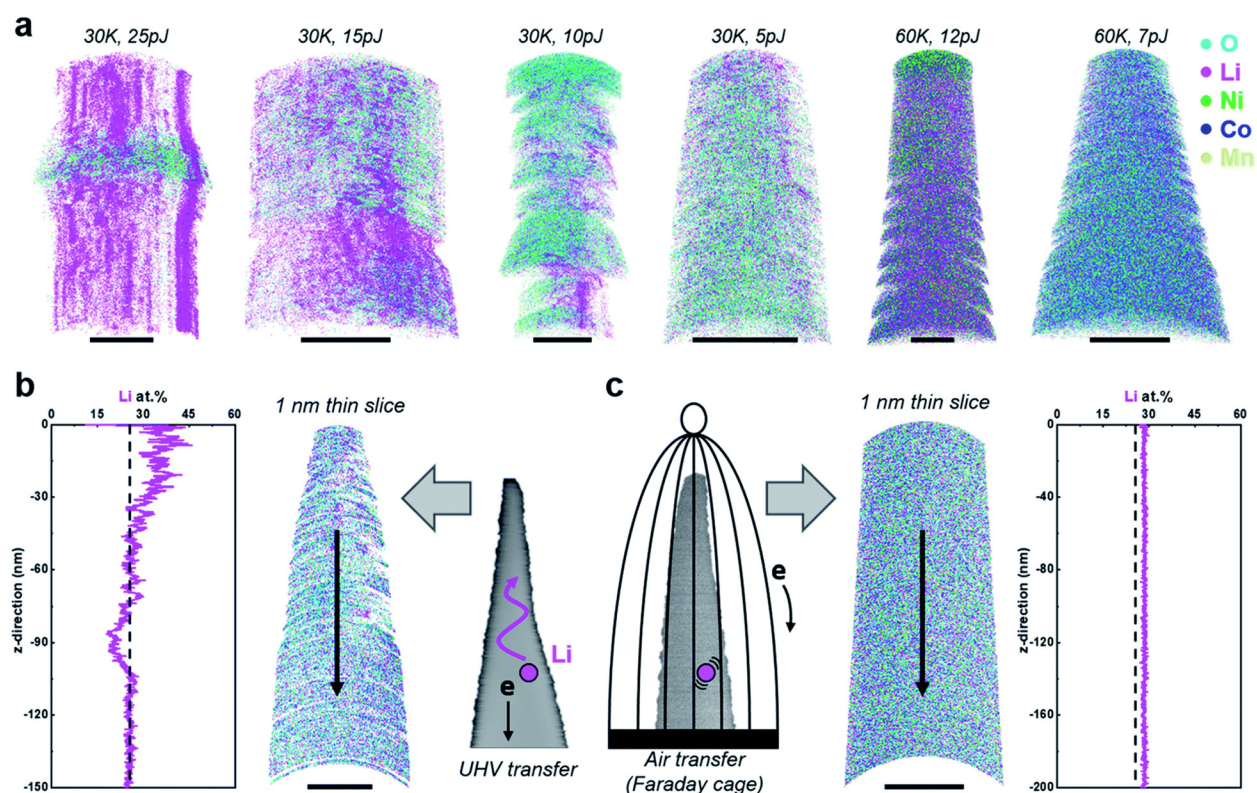


**FIG. 9.** (a) 3D atom maps of NMC811 samples obtained under a range of pulse energies and cryogenic specimen temperatures after UHV transferring. Scale bars are all 10 nm. APT results from (b) UHV and (c) air transferred samples. The nominal Li composition of NMC811 in each of the 1D composition profiles are indicated by the black dashed lines. Both APT measurements were performed at a base temperature of 60 K and a pulsed laser energy of 5 pJ. Scale bars in the atom maps are (b) 20 and (c) 50 nm. Reproduced with permission from Kim *et al.*, J. Mater. Chem. A **10**, 4926 (2022). Copyright 2020 authors, licensed under a Creative Commons Attribution (CC BY) License.

alkalis by APT. The purpose of the electric field is to trigger the field evaporation of surface atoms, making the prevention of unwanted atomic migration difficult.

Cryogenic specimen preparation (sharpening) is performed usually because (1) as it has been shown to reduce damage to beam-sensitive materials and prevent contamination of unwanted species and (2) increases resolution of images. Vibration of atoms about their rest position can cause aberrations to trajectories cause artifacts in the form of blurred images. Cryogenic cooling also combats some of the previously mentioned issues typical of semiconducting metal oxide battery materials, such as thermal diffusion and band bending.<sup>80</sup> Temperatures are usually in the range of 20–80 K. The key outcome, as evident in Figs. 9(a)–9(c), is that cryogenic specimen temperatures are important to enhance the quality of the compositional profiles. However, a material-specific optimal temperature must be found, approximated in the case of NMC811 at 60 K.

Maximizing knowledge of behavior at the nanoscale is achieved by performing APT with complementary microscopy and spectroscopy techniques. In 2015, APT under UV laser pulsing of LMO<sub>2</sub>-based (M = Mn, Ni, Co) cathode nanoparticles was performed alongside STEM, scanning x-ray transmission microscopy (STXM) and near edge x-ray absorption fine structure (NEXAFS). APT reconstruction

revealed the distribution of Li, Mn, and O at the nanoscale.<sup>81</sup> STEM imaging revealed the atomic scale structure, and STXM imaging combined with NEXAFS spectroscopy provided insight into the chemical state of the elements. Integration of this powerful host of techniques can thereby result in a comprehensive understanding of composition, structure, and chemical state at the nanoscale. However, access to such a wide range of instrumentation is often unavailable to most battery researchers. In 2021, application of STEM and APT to commercially used NCM cathode material demonstrated that the combination of these two advanced microscopy techniques provides sufficient information to directly correlate atomic-scale structural changes to electrochemical performance.<sup>82</sup> The primary outcome was that irreversible structural modifications occur once lithium leaves the cathode during charging. Intercalation of lithium back into the cathode during subsequent discharges is inhibited. These structural obstructions could partially explain the infamous decrease in capacity after the first cycle in Li-ion battery systems, and analogies can be drawn to other battery chemistries, such as Na-ions and K-ions.

One important aspect of the APT process in keeping with the theme of this review is in the selection of laser parameters used for experiments. Laser wavelengths used in the literature are typically near-UV to UV and the choice has major implications on the

**TABLE II.** Summary of a select few examples of materials investigated using operando electron microscopy and atom probe tomography measurements.

Technique	Electrode material	Capabilities	Limitations	Local resolution	
Electron microscopy	Silicon <sup>68</sup>	Atomic resolution imaging	Beam damage	< 1 nm	
	LiFePO <sub>4</sub> <sup>61</sup>	Energy filtered spectroscopy Imaging of interfaces	Complex sample holders for liquid electrolytes		
	LiNi <sub>x</sub> Mn <sub>y</sub> O <sub>z</sub> <sup>66</sup>		Limited electrode interfacial area under test		
	Germanium <sup>87</sup>		Contrast and SNR limitation from material thickness/Z number		
	LiMn <sub>2</sub> O <sub>4</sub> <sup>88</sup>	Crystal structure changes	Limited active material manipulation		Secondary electron surface reactions/radical formation
LiCoO <sub>2</sub> <sup>89</sup>	Composition mapping				
Atom probe tomography	LTO anode <sup>32</sup>	3D nanoscale compositional profiling	Need for cryo-operation	<1 nm	
		Atomic species detection and quantification	Highly involved specimen-specific sample preparation involving FIB lift out and cryogenic cooling under vacuum		
		Evaluation of surface and bulk properties at the nanoscale	Process-driven <i>in situ</i> delithiation		
		Grain boundary evaluation	Complexities in semiconducting materials:		
	NMC cathode <sup>82</sup> L(N)MO cathode <sup>81,90</sup>	Stacking fault detection	• Increased screening depth		
		Single ionic event detection	• Interactions between laser pulse and electric field		
		Segregation of impurities	• Lower surface electron density		
		Multi-scale defect detection			

species-specific information provided. An investigation into the effects of laser pulse energy and wavelength on APT of LFP cathode material demonstrated the difference in results between the use of 355 (UV) and 532 nm (green) lasers at an energy of 50 pJ per pulse.<sup>83</sup> The green laser resulted in the selective loss of lithium corresponding to a ~33% deficiency with a minor oxygen deficiency. The authors suggest that the loss of lithium was likely a result of the selective direct current evaporation of lithium between or after pulses. For the UV laser, results were much more favorable, with Li, Fe, and P present in close to nominal ratios. Meanwhile, oxygen loss was greater at up to 10% at. Laser pulse energy was then lowered from 50 to 1 pJ, which increased oxygen concentration to nearer its stoichiometry.<sup>84</sup> The results indicate that for those interested in the application of APT to lithium-based battery electrode materials, a UV laser source is most suitable to minimize *in situ* delithiation from the atom probe. However, it must be reiterated that experimental conditions for APT are typically material dependent. Green laser energy is absorbed less efficiently than UV for many lithium-based materials due to their inherent optical absorption properties with a bandgap at 196 nm (6.34 eV),<sup>85</sup> while alternative wavelengths may be more suited to lithium-free materials such as TiO<sub>2</sub>, given that its electronic bandgap lies at ~374 nm (3.2 eV).<sup>86</sup>

For the battery researcher, APT is a powerful addition to the arsenal of techniques used to characterize electrode materials. Given that modern electrode materials are typically nanoparticulate or nanostructured, the sub-nanometers resolution of structural features enabled by APT is highly applicable. Complex specimen preparation and process-driven artifacts in produced images limit its performance. However, the ability to provide insight into the changes that occur between individual ions is invaluable to understanding battery systems that operate

based on their movement (Table II). Operando APT of battery electrode materials during electrochemical cycling is yet to be achieved, to our knowledge.

## V. OPERANDO OPTICAL SPECTROSCOPIC METHODS

Moving from the higher energy end of the spectrum to optical wavelengths provides access to a host of phenomena that occur in battery materials and can often be achieved in the lab setting, removing a necessity for large-scale facilities. While x-ray methods and APT provide valuable information at an atomic level, optical spectroscopic or “spectroelectrochemical” techniques provide the ability to probe surface characteristics at both the nanoscale and macroscopic level using electromagnetic radiation in the ultraviolet (UV) to infrared (IR) range in a nondestructive fashion.

For applications to battery systems, the most common of these techniques are Raman spectroscopy followed by IR spectroscopy. More recently, the potential of direct UV-visible spectroscopy to decipher macroscopic changes in electrode materials has also been realized. A prerequisite for all operando optical techniques is a novel cell design to provide access to the incident beam. In a recent review of operando optical spectroscopic studies of batteries, a distribution of literature available concerning individual focus areas is provided, the focus areas in order of decreasing occurrence are lithium intercalation, polysulfide formation/shuttling, non-Li-ion electrode reactions, SEI formation/degradation, electrode structure, and electrolyte reactions/decomposition. Our review of operando techniques is focused on their application to battery electrode materials. Consequently, particular variations of the three aforementioned optical techniques of Raman, IR, and UV-Vis and their application to electrode materials are



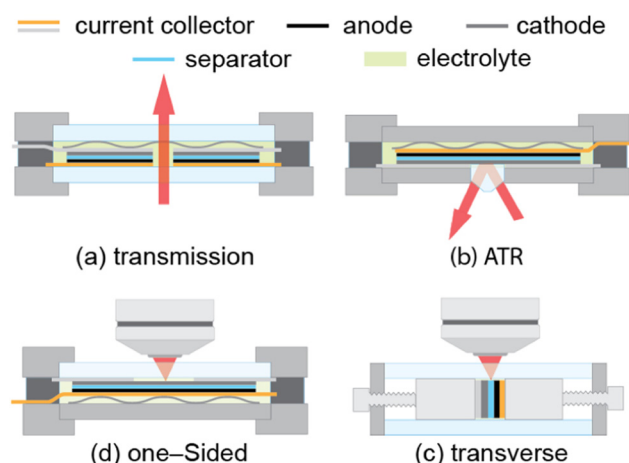


**FIG. 10.** Operando spectrochemical cell designs for optical spectroscopic methods grouped into the four primary configurations often reported in the literature. Reproduced with permission from Meyer *et al.*, *J. Electrochem. Soc.* **168**, 090561 (2021). Copyright 2021 authors, licensed under a Creative Commons Attribution (CC BY) license.

addressed. In most cases, designs involve the target anode or cathode material, a thin separator, and small electrolyte volumes. For probing electrode materials, electrolyte volumes must be chosen such that the spectroscopic response of electrolyte species is minimized to prevent significant attenuation of signals originating from electrode species. While specific cell designs vary between groups and approaches, they can be grouped into four primary configurations: transmission, attenuated total reflection (ATR), one-sided, and transverse as depicted in Fig. 10.<sup>91</sup>

### A. *In situ* Raman scattering of phase changes in battery electrode materials

Raman spectroscopy is commonly used to determine the composition of both crystalline and amorphous materials. The technique is based on the energy exchange and direction change associated with light incident on a molecule. The molecule gains energy and the energy of the photons scattered from the molecule can be measured to determine the composition of the molecule. These energies are observed as peaks on a Raman scattering spectrum, each peak corresponding to a specific molecular bond vibration or optical phonon for Raman-active molecules. For a molecule to be Raman-active, there must be a net change in its polarizability upon excitation. The technique is particularly useful for multi-layered materials such as the porous metal oxides often used in battery electrodes.<sup>92</sup> Information can be revealed on crystal structure, electronic structure, lattice vibrations, and flake thickness of layered materials and can be used to probe the strain, stability, charge transfer, stoichiometry, and stacking order.<sup>93</sup> The correlation between the capacity of intercalation in an electrode to the degree of disorder in the material can also be determined.<sup>41</sup> Such characteristics can be analyzed during cycling once an appropriate operando cell design is incorporated.<sup>94</sup> Window materials used include sapphire, KBr, diamond, and fluorite glass  $\text{CaF}_2$ .<sup>95</sup> The cells are referred to as spectroelectrochemical cells, providing the ability to perform electrochemical and optical measurements simultaneously.<sup>96</sup>

The most common Raman laser frequencies are 532, 638, and 785 nm, with 1064 nm used in certain cases. Sapphire or quartz is typically the window materials chosen, both with adequate transparency in this range. In choosing beam frequency, the two priorities are (1) to maximize Raman intensity leading to maximal SNR and (2) to minimize fluorescence such that masking of Raman signals produced by the electrode/electrolyte material is prevented. Lower energy lasers often require high power and longer exposure times to enhance SNR, which may lead to beam associated sample damage. The target sample and its associated properties must also be considered prior to beam choice as each material can produce certain artifacts in the Raman spectra obtained. For example, nanoparticle size has a significant effect on the associated Raman signal. Most industrial cathode materials consist of nanoparticulate powders. Small nanoparticles tend to fluoresce, meaning lower energy lasers (such as 785 nm) are a more appropriate choice to avoid significant background luminescence. For more sensitive electrode materials such as silicon wafers, higher energy lasers (such as 532 nm) require lower laser power and shorter accumulation times compared to a near-IR beam, with appropriate care to account for photoluminescence emission in crystalline nanoscale silicons due to quantum confinement.

In terms of the interpretation of operando Raman spectra, there are four primary spectral features that can be used to elucidate structural changes from an electrochemically modified material.<sup>97</sup> (1) The appearance of a new band, which indicates the presence of a new Raman mode or transformation of a previous phase to a new one, and (2) the shift of vibrational mode, which indicates changes in particle size and corresponding interlayer spacing. Red shifts to lower wavenumbers indicate an expansion or lengthening of the constituent bonds of the corresponding phase, while blue shifts to higher wavenumbers indicate a contraction or shortening of the constituent bonds, or crystal structure modification by alloying, intercalation, etc., (3) a change in spectral band profile such as a change in bandwidth, indicative of the degree of order in the probe area. Increasing bandwidth during operando measurements represent a shift toward disorder in the system, and (4) changes in band intensities. The origin of band intensity fluctuations are more difficult to track and can be a result several changes to a material. Common causes include a change to the concentration of the corresponding phase or blocking of the original signal due to interference from other species, e.g., intensity changes or band convolution from Raman modes of electrolyte or surface species on the material-under-test.

In Nakagawa *et al.*,<sup>98</sup> the changes in the surface crystallinity of edge plane HOPG (graphite) anodes are probed using *in situ* Raman spectroscopy. The corresponding spectra show that surface crystallinity is significantly lowered within only a single charge/discharge cycle. The combination of these results with considerations of the intercalation mechanism of  $\text{Li}^+$  provides information on the structural degradation of the graphite surface. Conventional Raman spectroscopy is limited to near-surface regions predominantly, depending on the optical characteristics (scattering, absorption, etc.) at the incident probe wavelength. More intricate adjustments are required to permit deeper penetration. Like the techniques mentioned previously, *in situ* Raman measurements require a more complex electrochemical cell. Here, a three-electrode cell was equipped with an optically flat window made of Pyrex glass to permit light transmission.<sup>41</sup>

In Zhu *et al.*,<sup>99</sup> *in situ* Raman and *in situ* XRD are used to probe electrode degradation mechanisms in a lithium-sulfur battery, see Fig. 11.

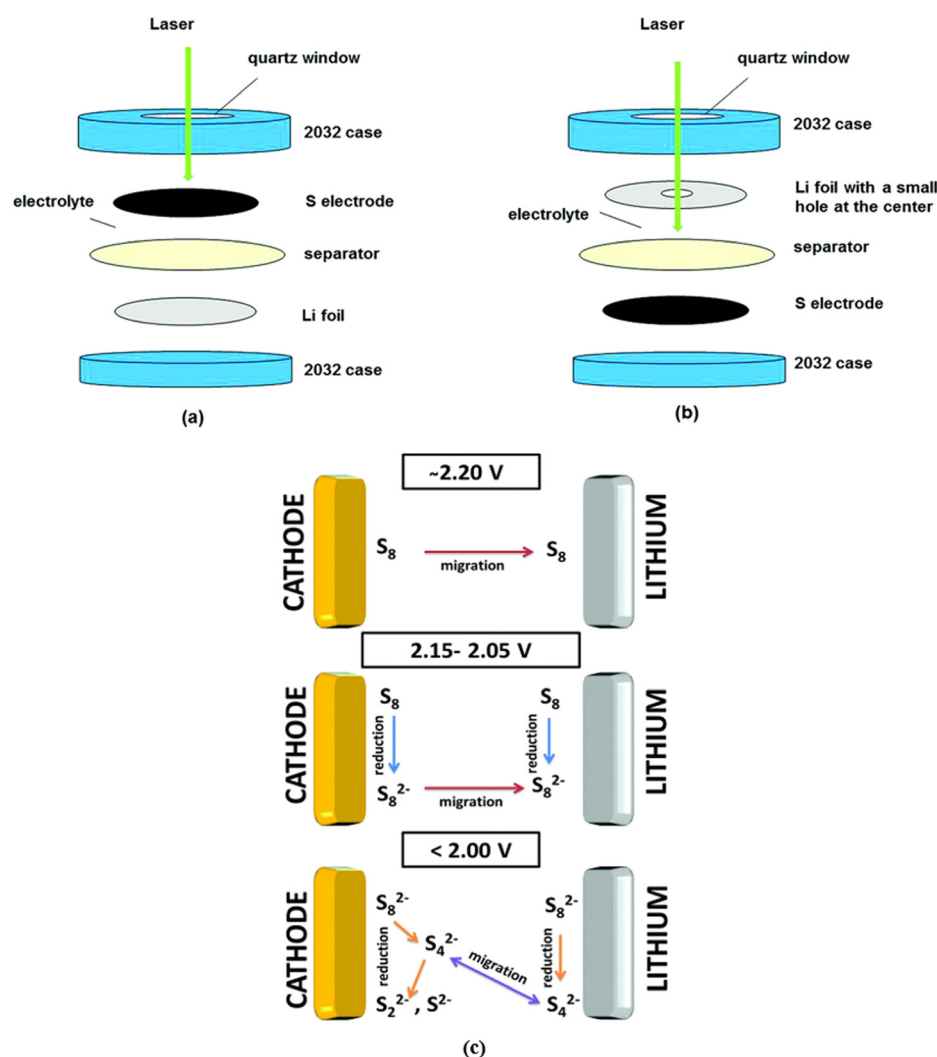


FIG. 11. *In situ* Raman cell designs for monitoring changes in (a) the cathode and (b) electrolyte near Li metal. (c) Schematic of the reduction process from *in situ* Raman measurements at both the cathode and Li metal sides depicting the evolution of polysulfide species in a Li-S battery. Reproduced with permission from Zhu *et al.*, Sustainable Energy Fuels 1, 737 (2017). Copyright 2017 Royal Society of Chemistry.

Lithium-sulfur (Li-S) batteries have a very high theoretical capacity of  $1675 \text{ mA h g}^{-1}$ , but there are significant issues with the associated discharge mechanism.

In that work, analysis of the mechanism is based on the influence of the electrolyte on the dissolution of sulfur and polysulfides was outlined. The short lifetimes of the polysulfide species provide the rationale for the use of operando measurements during discharging or charging. While the same species are detected in each case, the rates of polysulfide formation and diffusion to the anode depend on the electrolyte and the associated ionic mobilities of the various species in the electrolyte. *In situ* Raman scattering measurements of the Li-S battery in an ionic liquid electrolyte (LiTFSI-PY13-FSI) and ether-based electrolyte (LiTFSI-DOL-DME) were performed for Fig. 11(c) provides a summary of the evolution of the polysulfide species occurring at both cathode and anode.

The Raman spectroscopy performed here provides a clear picture of the discharge mechanism of a Li-S battery, the effects of the chosen electrolyte and compares the phase changes of ionic species in the

electrolyte in the vicinity of both the sulfur cathode and Li metal anode. The cell designs used allow measurements to be performed nondestructively in real-time, capturing the true behavior of the system during discharge. Application to more traditional battery systems containing common electrolytes is straightforward. The Li-ion transport dynamics at particle level are revealed via *in situ* Raman spectroscopy in Wei *et al.*<sup>100</sup> for a battery containing a  $\text{LiFePO}_4$  cathode and electrolyte composed of  $\text{LiPF}_6$  in ethylene carbonate (EC) and dimethyl carbonate (DMC) through the examination of Raman peaks originating from the C-O stretching vibration in EC. The Li-ion concentration at the cathode surface was found to fluctuate based on the redistribution of  $\text{Li}^+$  within the pore space of the electrode.

All-solid-state lithium-ion batteries (ASSBs) have also attracted attention.<sup>101–103</sup> However, the major concern with these systems is the instability of the interface between the sulfide solid electrolytes and the electrodes. Once again, the electrochemical processes that govern the evolution of the interfacial layers require *in situ* measurements, preferably those that can also provide nondestructive information in

real-time. *Ex situ* and *in situ* Raman spectroscopy is used in Zhou *et al.* to probe degradation mechanisms at the electrode/solid electrolyte interface in real-time.<sup>104</sup> *In situ* and *ex situ* Raman spectroscopy are applied in tandem to probe the evolution of sulfide species during discharge once again. With a one-sided cell design, they demonstrated that *in situ* Raman measurements can access the lithium/solid electrolyte interface, and the solid/solid interfaces within the layers of the composite positive electrodes. Clever adaptations are made to the cell design that expands the range of electrode-related phenomena that occur during cycling. Metallic coatings are applied to the borosilicate window, which then act as current collector between electrode and solid electrolyte. A 50 nm copper (Cu) coating is applied to investigate the extent of lithium plating that occurs at the electrode/solid electrolyte interface. The Cu coating effectively acts as a substrate for lithium plating while simultaneously maximizing access of the Raman beam to the plating process. A 50 nm gold (Au) coating with transparent area at the center is then applied to examine the stability of LiCoO<sub>2</sub>. The study stands as a demonstration of the versatility of some operando cell designs and shows the value of *in situ* Raman spectroscopy to understand the effects of cycling on the interfaces within ASSBs and the consequential routes to electrode degradation. Given that *in situ* Raman can be used at a microscale level with the appropriate beam width, application to thin film ASSBs can thus clarify local structural changes at multiple locations within the cell. An example of such is demonstrated in Matsuda *et al.*,<sup>105</sup> where micro Raman spectroscopy is used to interrogate the local material structure at either side of the LiCoO<sub>2</sub> cathode by acquiring measurements at the front and back of the cell.

The implementation of operando Raman spectroscopy to investigate battery electrode degradation can shed light on the structural changes of the materials as a consequence of the electrochemical processes which occur during charge and discharge of a battery. Most success is found when *ex situ* Raman measurements are used to streamline the *in situ* or operando experiments. Its use in tandem with other complementary techniques could provide a detailed characterization of structural–electrochemical relationships. Given the correct cell design, application to a wide range of state-of-the-art battery designs including Li–S batteries, ASSBs, and thin film batteries is possible in a small-scale lab setting.

### B. *In situ* ATR-FTIR for probing electrolyte decomposition at the electrode/electrolyte interface

Fourier transform infrared spectroscopy (FTIR) is based on the absorption of infrared light over the wide spectral range of  $\sim 14\,300\text{--}20\text{ cm}^{-1}$ . In most battery systems, the solvents used as electrolytes are dominated by chemical bonds with energies in the IR spectral range. Light absorbance as a function of wavelength is calculated to produce a series of absorption peaks. The peaks are caused by excitations of molecular vibration, rotation/vibration, lattice vibration modes, or a combination of each. Each corresponding frequency can be correlated with specific functional groups, while infrared peak intensity can be linearly correlated with the amount of species in the sample.<sup>106</sup>

One of the key issues that arises in the battery performance assessment and battery materials analysis is the monitoring of organic species, particularly at the SEI layer. Widely used techniques, such as x-ray photoelectron spectroscopy (XPS), provide some information on

organic and inorganic SEI species but are difficult to implement in operando.<sup>107</sup> NMR provides more information on organic solvents but cannot be incorporated to probe the solvents at the surface of the electrode and monitor the SEI layer.

*In situ*/operando FTIR spectroscopy can be employed at the electrode surface and proves very powerful in the analysis of organic species in real-time, identifying the composition and structure of species within the cell based on the identification of the functional groups present. One of its main uses being the monitoring of electrolyte solvents, including the gaseous products formed upon oxidation and reduction of the electrolytes near the electrode interface.<sup>108</sup> Information can then be provided on the electrochemical changes that occur in the solvents during cycling, such as solvation and desolvation.<sup>96,109</sup> Using this information, an insight into the impact that these processes have on the electrodes and species in the vicinity of the electrodes such as the SEI layer can be obtained in real-time, some of which are schematically represented in Fig. 12.<sup>110,111</sup> Four sampling techniques are used: transmission, specular reflectance, diffuse reflectance, and attenuated total reflection (ATR).<sup>112</sup> While each sampling techniques has its benefits, ATR-FTIR is most often incorporated for operando measurements of battery electrode material interfaces with the electrolyte. While transmission FTIR measurements are useful for bulk properties, ATR-FTIR is essentially independent of sample thickness, constituting an internal-reflection-based method with a typical penetration depth of  $0.2\text{--}3.0\text{ }\mu\text{m}$ .<sup>113</sup> ATR-FTIR measurements are enabled by an ATR sensor of suitable optical material. The material must be optically transparent to the frequency of incident energy so that none of the useful radiation is absorbed. The material must also have an index of refraction greater than the surrounding media, so that total internal reflection occurs, with the sensor essentially acting as a waveguide. Typical sensor materials include ZnSe, diamond, Ge, Si, and KRS-5. Decision

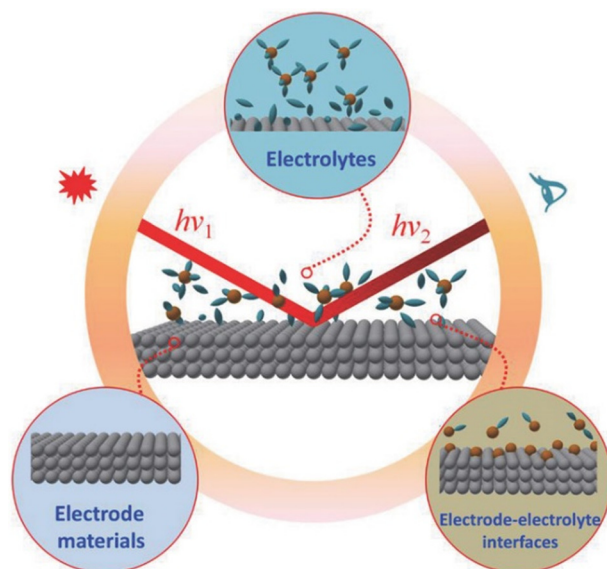


**FIG. 12.** Schematic of conventional spectroscopic methods in secondary battery studies focusing on the electrode/electrolyte interface. Reproduced with permission from Deng *et al.*, *Small Methods* **2**, 1700332 (2018). Copyright 2018 Wiley-VCH.



on the choice of these materials is dependent on the region of interest within the IR range (near-IR, mid-IR, or far-IR).<sup>114</sup>

As with other techniques described thus far, a challenging aspect of using *in situ* FTIR to monitor cell degradation is the cell design. With the correct cell design, *in situ* FTIR spectroscopy can be applied to a range of battery systems. In the analysis of battery materials, the technique serves mainly to provide insight into the  $\text{Li}^+$  dynamics at the electrode/electrolyte interface, a situation where ATR-FTIR can be very useful.<sup>115</sup> A schematic of a representative setup is shown in Fig. 13(a). In contrast to traditional FTIR spectroscopy, surface sensitivity is enhanced. The precise penetration depth depends on wavelength, incident angle, and the electrode material along with any interfering electrolyte species and cell components.<sup>116</sup>

The high surface sensitivity of the method and its dependence on multiple light reflections mean that it is extremely useful for probing composite and multi-layered materials such as those used in battery systems, remaining useful irrespective of the battery chemistry. In Marino *et al.*, ATR-FTIR spectroscopy is used to probe conversion-type electrode materials.<sup>117</sup> These materials demonstrate interesting performance in terms of capacity but are associated with poor Coulombic efficiency. Poor Coulombic efficiency is usually related to the relentless formation and desolvation of the SEI during conversion and back-conversion reactions. The setup is shown in Fig. 13(a), with a diamond prism used as a waveguide for the ATR-FTIR approach, an  $\text{NiSb}_2$  electrode, and  $\text{LiPF}_6$  electrolyte dissolved in EC and DMC. The measurements are obtained in the vicinity of the electrode/electrolyte interface.

Figure 13(b) shows the corresponding IR spectra obtained at a rate of 1 C during first discharge. By examining the IR spectra and comparing to known values in the literature, the origin of each of the peaks from species present in both the electrode and the electrolyte. The shift in the peaks of the spectra during cycling means that dynamic evolution of the lithium concentration in the electrolyte can be followed. Tracking of the formation and desolvation of the SEI layer is also achieved. The operando measurements confirm the phase separation of the conversion materials during discharge and the nanostructuring of the electrode.

Mentioned repeatedly in this review is the promising performance of silicon electrodes and their applicability to next generation battery systems. The ATR-FTIR approach is applied to thin-film amorphous silicon electrodes in operando in Corte *et al.*,<sup>118</sup> providing information into the characteristic performance issues related to the reaction of silicon to lithiation and the composition of the SEI layer formed. ATR-FTIR assesses the thickness of the SEI layer, which increases during lithiation and partially reduces during delithiation. Question marks remain over applicability of the approach to silicon-based electrodes since they are commonly in (nano)dispersed form, included in a composite with additives and binder, given that ATR-FTIR spectroscopy is most useful with thin film materials. Nevertheless, the study improves understanding of the processes that govern silicon lithiation and can be applied to any thin film electrode material that does not demonstrate excessive IR absorption. This issue often arises in the study of pure metals. As a result, metal oxides are very suitable for IR analysis.

ATR-FTIR spectroscopy proves useful in its ability to probe causes of battery electrode degradation by analyzing SEI formation on the electrode interface during cycling. While its use is demonstrated here for the analysis of silicon electrode-based systems,<sup>115</sup> the technique can be applied to several battery technologies even beyond lithium-ion, such as lithium-oxygen, sodium-ion, and potassium-ion.<sup>119–121</sup> A compendium that reviews optical spectroscopy as a tool for battery research can be found in Köhler *et al.*, with a particular focus on UV-visible and IR spectroscopy.<sup>122</sup> Applications to thin film, multi-layered battery electrode materials demonstrate the power of operando ATR-FTIR, providing detailed insight into the evolution of the SEI layer, which has a significant impact on conversion-type battery electrodes.<sup>123,124</sup>

### C. Tracking the optical signature of photonic crystal electrodes in real-time

The performance and longevity of battery systems are determined primarily by the structural and electrochemical changes that occur within the component materials. In comparison to planar deposits of electroactive material, color-coded, thin-film battery

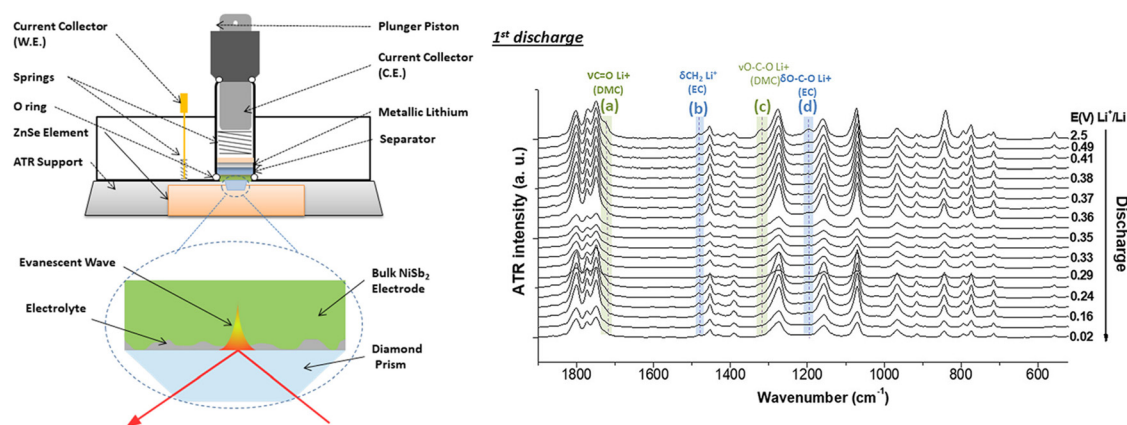


**FIG. 13.** (a) Schematic of the electrochemical cell used for the *operando* ATR-FTIR experiment. (b) *Operando* IR spectra obtained during the first discharge of  $\text{NiSb}_2$  electrode at a rate of 1 C with 1 M  $\text{LiPF}_6$  in EC:DMC (1:1) + 2% v/v VC electrolyte. Reproduced with permission from Marino *et al.*, J. Phys. Chem. C **121**, 26598 (2017). Copyright 2017 American Chemical Society.

materials enable real-time diagnostics by observing their “structural” color,<sup>125</sup> caused by a phenomenon known as the photonic bandgap (PBG).<sup>126–129</sup> When light is incident on a periodic material with a period on the order of the wavelength of incident light, photons within the PBG are reflected, producing the observed structural color.<sup>130,131</sup> The observed coloration can be correlated with a specific optical signature for each material, so optical measurements can be used to characterize their structure.<sup>132–134</sup> Such measurements have been widely used for battery materials in recent years<sup>108,135–138</sup> and are extremely useful for porous electrode structures such as photonic crystals (PhCs).<sup>110,139–144</sup> Because periodically porous materials can be fashioned from self-assembly methods through to electron beam lithography and many methods in between that give exquisite control over complexity, the wider research community can grow materials with a tunable PBG without the need for expensive equipment or complex fabrication techniques.<sup>145</sup> An adjustable PBG in a material gives the opportunity to monitor small changes in material properties using angle-resolved reflectance or transmission measurements.<sup>146</sup> We see PhCs in a wide variety of disciplines, including optical,<sup>147–149</sup> energy storage,<sup>110,123</sup> and biological<sup>150–152</sup> and medical devices.<sup>153,154</sup> Such structures can also behave as optical waveguides,<sup>155</sup> refractive index sensors,<sup>156,157</sup> biosensors<sup>153,158</sup> and also provide opportunities for tuning solar absorption.<sup>159,160</sup> More recently, they have been assessed as binder and conductive additive-free structured electrode materials in Li-ion batteries.<sup>108,135–138</sup>

The study of more complex redox processes, alloying and conversion, and the need to optimize more established chemistries has motivated the development of new analytical operando techniques that allow study of the fundamental mechanisms by which these materials operate, together with the kinetics of these processes.<sup>45,161–165</sup> Inverse opal (IO) PhCs have been widely researched as anode materials for lithium-ion batteries (LIBs). Composition changes, Li doping, potential-dependent electrochromism, cation insertion rate-dependent dielectric constant modification, and the photonic signatures of lithium insertion into an ordered 3D structure can be achieved by making battery electrode materials in the form of IOs.<sup>108</sup> Some studies have analyzed their optical reflectance and transmission.<sup>16,19,96</sup> As a result, there is a large body of data available when choosing potential anode or cathode materials. An extensive review of IOs and their applications to energy storage mechanisms can be found elsewhere.<sup>166</sup> Despite this, optical characterization of IO battery electrodes *in situ* or in operando has not been achieved.

Fundamentally, despite some clear parallels between materials science, electrochemistry, and photonic spectroscopies, these disciplines have not yet been combined and brought to bear on new electrode designs in emerging alternative energy storage materials neither for performance-related device improvements,<sup>167</sup> nor fundamental assessment of new modalities, analytics, or diagnostics of electrochemical materials response—the research community needs to explore interdisciplinary approaches to drive the next innovation in portable energy storage, especially when new materials and new ways of manufacturing batteries, such as 3D printing, become more advanced.<sup>168–170</sup>

Most transmission/reflectance studies<sup>171</sup> of IO anodes have been carried out prior to cell assembly.<sup>96</sup> This is mainly due to the challenge presented by the closed nature of standard electrochemical cells. While high intensity x-rays can penetrate appropriate metal casings, photon energies in the optical frequency range require alternative operando

cell strategies. In common with Raman scattering and FTIR spectroscopies, optical spectroscopy measurements require less intuitive cell designs to facilitate light penetration to the electrode over a suitable area to ensure suitable SNR for the spectroscopic data. Such adaptations have been made in Loneragan *et al.*, where the optical transmission of IO anodes are examined when placed in a range of solvents.<sup>172</sup>

Tracking the optical signature of PhC electrodes in operando may be an effective, low-cost route to probing their degradation mechanisms nondestructively in real-time. Progress is being made in developing the correct methodology for achieving these measurements, with particular attention to consistent cell assembly and internal pressure that does not alter the periodicity of the periodically porous material, nor inhibit volumetric or other changes that can occur during reversible ion (de)intercalation. To achieve success, factors such as cell design, light-electrolyte interaction, and electrode response to the degree of lithiation must be considered. Like the XRD and acoustic fingerprints observed for battery materials, the optical fingerprint of PhC nanostructures may prove an important asset for further understanding of the physical and chemical processes that govern battery performance. A first step in describing the optical behavior of ordered porous battery electrodes is a model system to examine charge storage mechanisms, in built stresses, and volumetric changes; moreover, the intrinsic benefit or scaled porosity to ionic diffusion, electrical conductivity, and material interconnectedness is accurate data in battery electrolytes. For an inverse opal photonic crystal of any material, such as the example shown in Fig. 14, the following summarize the basic relationships that are useful in characterizing the photonic bandgap and its dependence on surrounding environment (air or solvent), effective refractive index, and the angle of incidence for reflectance or transmission signal in a typical angle-resolved reflectance/transmission setup.

For a crystal plane (hkl) with interplanar spacing  $d_{hkl}$ , an IO material with an effective refractive index  $n_{\text{eff}}$ , some solvent of refractive index  $n_{\text{sol}}$  filling the pores, a Bragg resonance order  $m$  and some angle  $\theta$  between the incident light and the normal to the crystal plane surface, the transmission minimum  $\lambda_{hkl}$  can be found via the Bragg–Snell model as follows:  $\lambda_{hkl} = \frac{2d_{hkl}}{m} \sqrt{n_{\text{eff}}^2 - n_{\text{sol}}^2 \sin^2 \theta}$ , a plot of the observed minimum wavelength squared vs the sine of the angle of incidence squared should yield a linearly regressive plot with a slope  $\mu_0 = -4d_{111}^2 n_{\text{sol}}^2$  and an intercept  $\gamma_0 = 4d_{111}^2 n_{\text{eff}}^2$ . From this, the interplanar spacing  $d_{111}$  and hence the center-to-center pore distance  $D$  can be found via the slope. The effective refractive index  $n_{\text{eff}}$  of the IO material can be estimated by dividing the intercept by the slope. Currently, there are several methods used in a wide variety of literature to approximate the effective refractive index of composite materials.<sup>173,174</sup> The Drude model for inverse opal systems can be formalized as  $n_{\text{eff}} = \sqrt{n_{\text{IO}}^2 \phi_{\text{IO}} + n_{\text{sol}}^2 \phi_{\text{sol}}}$ . The parallel model for an inverse opal system can be written as  $n_{\text{eff}} = n_{\text{IO}} \phi_{\text{IO}} + n_{\text{sol}} \phi_{\text{sol}}$ . For an inverse opal system,  $n_{\text{IO}}$  refers to the refractive index of the crystalline IO material,  $n_{\text{sol}}$  is the refractive index of the surrounding medium,  $\phi_{\text{IO}}$  constitutes the volume filling fraction of IO material in the system, and  $\phi_{\text{sol}}$  is the volume filling fraction of the surrounding medium. For inverse opal photonic crystal filled with a solvent, a Bragg–Snell relation in terms of the Drude model for  $n_{\text{eff}}$ :  $\lambda_{\text{min}}^2 = 4d_{111}^2 [n_{\text{IO}}^2 \phi_{\text{IO}} + n_{\text{sol}}^2 (1 - \phi_{\text{IO}})]$ . Specific details are found elsewhere<sup>175</sup> for a variety of solvents and substrates, but the principle allows, in general, the PBG to be a trackable parameter caused by material and effective index modification when it

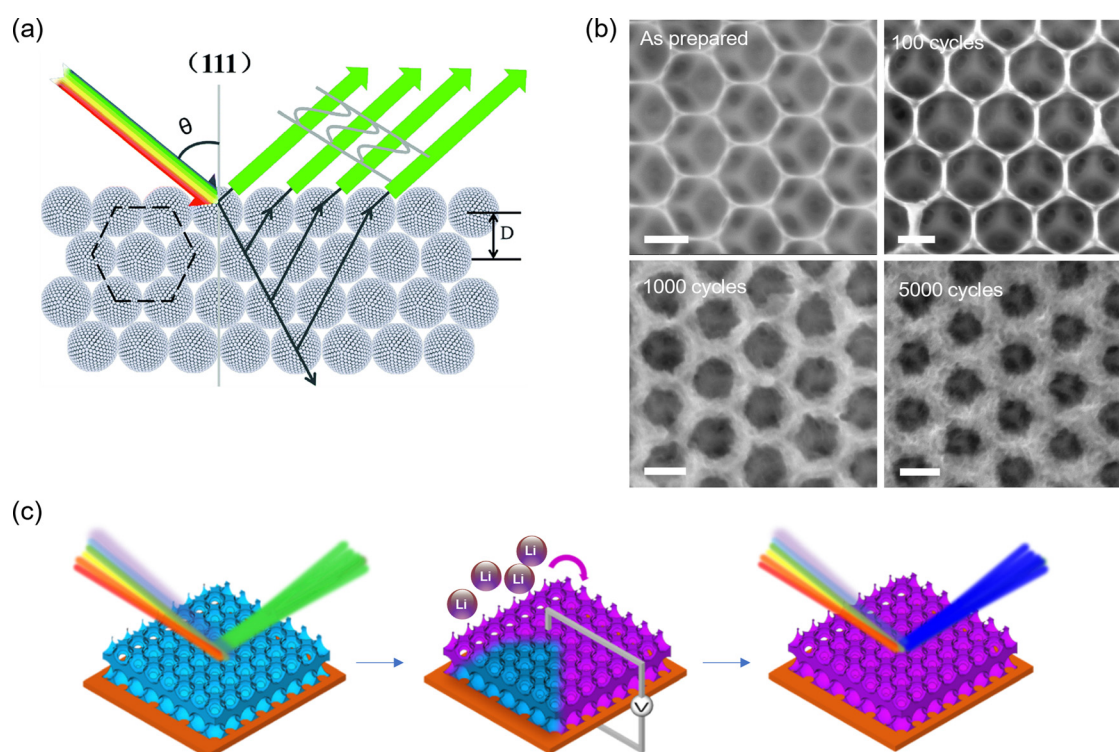


**FIG. 14.** (a) Schematic of the PBG in an opal photonic crystal, selectively reflecting a narrow band of photon energy. Light within the PBG is reflected from the crystal, determined by the lattice constant, proportional to the sphere diameter  $D$ . Reproduced with permission from Wang *et al.*, *J. Mater. Chem. C* 7, 11972 (2019). Copyright 2019 Royal Society of Chemistry. (b)  $\text{TiO}_2$  inverse opal materials used as an anode in a Li-ion battery showing interconnected volumetric swelling as lithiated titanate over 100, 1000, and 5000 cycles. Scale bar = 200 nm. (c) Schematic representation of operando angle-resolved reflectance measurement of a photonic bandgap during reversible lithiation. Adapted with permission from McNulty *et al.*, *Adv. Energy Mater.* 7, 1602291 (2017). Copyright 2017 Wiley-VCH.

undergoes electrochemical modification or changes during cycling in a battery cell. Adaption to closed coin cells or similar form factors has yet to be established.

Tracking variation in photonic crystal materials in real-time spectroscopically allow, in principle, tracking of changes to effective refractive index, periodicity, and conductivity as a function of cycling parameters in voltammetric or galvanostatic conditions. Volumetric swelling and lithiation/sodiation would vary the refractive index contrast and periodicity, shifting the photonic bandgap predictably for a material that is structurally well-defined. In addition, the change or erasure of periodicity, for materials where large cyclic volumetric changes occur, would indicate whether ordered arrangement or *in situ* pulverization and relief of new surfaces is a contributory cause to coulombic efficiency, capacity loss, or a limitation in charge rate behavior for a fixed thickness. These approaches are currently being developed for relevant battery materials to tackle open questions in materials that are assembled with coating morphology and mass loadings that are more relevant to battery cells in various form factors.

The solvents chosen are typical of those used for electrolytes in both industry and research. The study can be considered a preliminary *ex situ* experiment that provides insight into the effects of potential electrolytes on the incident beam. Just as seen for all techniques discussed thus far, this *ex situ* information can be used going forward to streamline operando experiments. A transparent “flooded” cell is used

in the study, a design previously used for electrochemical performance assessment of PhC anodes in excess electrolyte. The cell design allows light penetration such that measurements can be obtained nondestructively. While this constitutes a step in the right direction by studying the materials in the assembled cell, optical measurements in real-time are required to provide a better insight into battery performance. 3D structured electrochemical energy storage (EES) materials do not require pristine, defect-free large-scale arrays<sup>176</sup> of electroactive deposits as would be required in photonics<sup>177</sup> that use semiconductive inverse opals for optics, telecommunications, optical interconnects, and silicon photonics, as pertinent examples.

Optical techniques applied to functioning battery materials *in situ* are rare and typically are used to examine the structure of electrolyte compositions of the synthetic preparation of materials.<sup>178–180</sup> Only recently, photonic crystals have been used to enhance the photo-absorption characteristics of perovskite halide solar cells using structural color to tune the absorption across the entire visible spectrum.<sup>181</sup>

While such measurements have not been obtained for IO anodes, operando optical analysis has been achieved for graphite anodes.<sup>182</sup> In 2016, Ghannoum *et al.* used an optical fiber sensor (OFS) to obtain information about the interaction of near infrared light with graphite during its electrochemical lithiation process in a lithium-ion pouch cell. Here, the optical transmission measurements were confined to the overall intensity of the optical signal as a voltage. Further work by



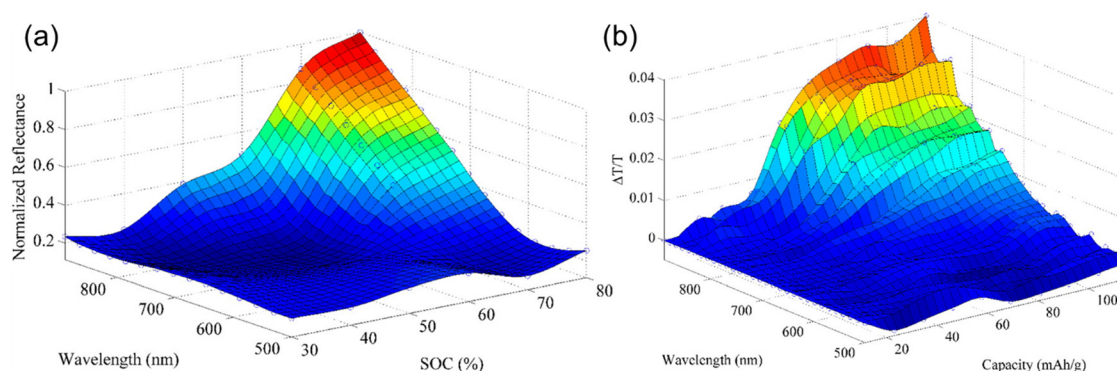


**FIG. 15.** (a) *In situ* optical reflectance measurements of lithiated commercial graphite electrodes at various states of charge. (b) Operando optical transmission measurements of graphite electrodes during lithiation. Reproduced with permission from Ghannoum *et al.*, ACS Appl. Mater. Interfaces **8**, 18763 (2016). Copyright 2016 American Chemical Society.

Ghannoum *et al.* in 2020 provided a more extensive optical characterization of the system.<sup>183</sup> As shown in Fig. 15, reflectance spectroscopy measurements of lithiated commercial graphite anodes at various states of charge were obtained. To obtain the measurements, the graphite anodes were extracted, and the cells disassembled in an inert environment. Next, an OFS was embedded like the previous study, this time in a custom-designed Swagelok cell. Fiber evanescent wave spectroscopy (FEWS)<sup>184</sup> was used to provide operando optical transmission measurements during lithiation of the graphite anode. Reflectance and transmission measurements both demonstrate that there is a direct correlation between the wavelengths reflected/transmitted and SoC. The results further highlight the need to monitor these changes in optical activity under operando conditions. After some adaptations, the approach used here may be the key to obtaining operando optical transmission/reflectance measurements of IO anodes.

Other recent approaches have used operando terahertz time-domain reflectometry spectroscopy<sup>185</sup> (THz-TDS) to investigate solid electrolyte interphase evolution on silicon anodes. THz-TDS operates in the  $10^{11}$ – $10^{13}$  Hz frequency range<sup>186</sup> as a nondestructive mode. It is based on characterization of the dielectric nature of the sample under test. For battery materials research, THz compatible windows are readily available, and can be integrated into various form factor cells such as coin cells or larger split cells for larger window aperture. The amplitude and phase of the electric field provide the information based on attenuation of the reflected THz field following sample interactions. In this study, Krotkov *et al.* examined an anode comprising silicon nanoparticles, some binder, and a small addition of conductive carbon. In Fig. 16, the basic setup for this approach is summarized along with data from an experiment that allow operando tracking of SEI formation at the surface of the silicon nanoparticles during cycling, with a pronounced dependence on the time between charge-discharge of cycles. They found that certain parts of the SEI tend to dissolve during rest periods if the film was not fully formed prior to the restart of the polarization, particularly for elements of the SEI that are unstable at higher voltages as the charging voltage increases. The measurements show that SEI formation and reformation after dissolution is not only dependent on fresh surface formation that occurs after pulverization or cracking from repeated volumetric changes. The signal is clear for

SEI dissolution following some cracking of the underlying silicon, but that SEI stability at different voltages is not consistent and shown through changes in the effective dielectric constant of the anode during cycling.

#### D. Internal sensing of battery response: Fiber Bragg grating (FBG) sensors and probes

There are measurement systems in composites research that use fiber Bragg grating sensors within composite matrices and laminates of materials to perform operando measurement of stress-strain and other mechanical properties.<sup>187</sup> These were developed to avoid some limitation of attachment-type sensors, often based on cantilevers that give uniaxial information (depending on its orientation on the composite or device), and in many cases is limited to device-level information. Recent reports<sup>188,189</sup> have begun to implement FBGs inside battery cells, to get at real-time assessment of the interplay between chemical, mechanical, thermal, and other properties and their relationship under specific battery cycling conditions. Fiber Bragg gratings used in this way are assessed by monitoring changes to reflectance or a specific splitting of reflectance peaks caused by birefringence.<sup>190</sup>

Real-time monitoring of the dynamic chemical and thermal behavior of a battery becomes important when safety and reliability are paramount in new cell chemistries or form factors. Blanquer *et al.* integrated FBG into 18650 and pouch cells to directly monitor temperature, strain, and hydraulic pressure and showed they could be correlated with battery state-of-health and indeed state-of-charge. Careful adjustment of the morphology of the fiber was necessary to enable spectral changes from temperature and pressure in a manner that allowed them to be decoupled. The method summarized in Fig. 17 was then shown to provide operando information on SEI formation and structural evolution of the electrodes. Further details on specific analyses can be found in Ref. 188. Other work has addressed the possibility of direct SEI formation tracking under operando conditions, notably the work of Louli *et al.* where operando pressure measurements quantified lithium inventory loss to irreversible cell volume expansion while physically detecting SEI growth during cycling.<sup>191</sup>

The same group also adapted the approach by using multiple sensors (Fig. 18) to measure cell-generated heat during cycling and

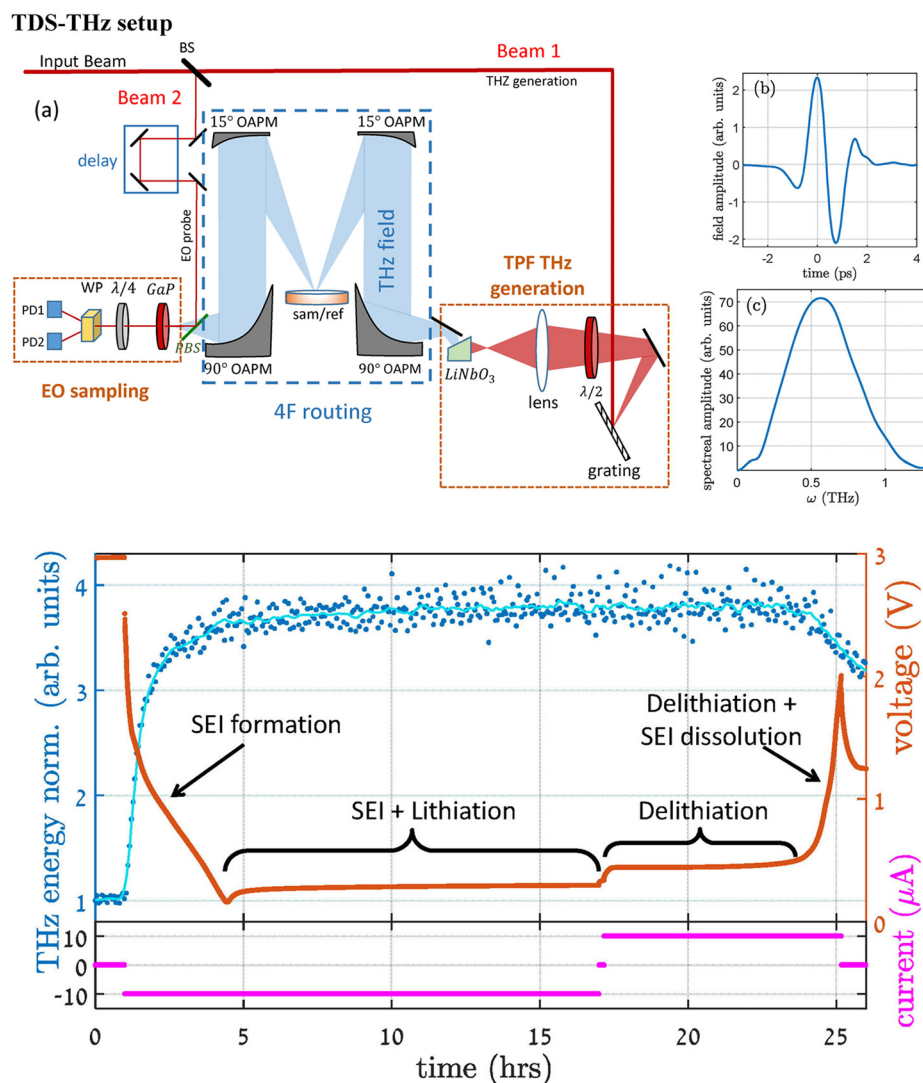


**FIG. 16.** (Top) (a) Schematic of the time-domain THz spectrometer setup in reflection mode with the battery cell placed at prime focus. (b) An example of a THz signal in the time domain together with its associated amplitude spectrum. Electro-optic sampling module includes a pellicle beam splitter (PBS), a Gallium Phosphate crystal (GaP), quarter-wave plate, a Wollaston prism (WP), and two photodiodes. (Bottom) The THz signal (blue dots) in the time domain during a single full cycle. The cycle comprised the discharge (1–17 h) followed by charging (18–26 h). The cell voltage is shown in orange and the current in magenta. Reproduced with permission from Krotkov *et al.*, *Batteries Supercaps* **5**, e202100183 (2022). Copyright 2022 authors, licensed under a Creative Commons Attribution (CC BY) License.

compared the operando measurements to those by isothermal calorimetric measurements.<sup>189</sup> One major motivation from a practical standpoint is that current heat generation and dissipation measurement techniques are slow, require larger infrastructure, and are limited to measurements outside the cell. The authors detail the basis of their heat mapping models, factoring a zero-dimensional model that was scalable (Fig. 18). Three separate FBGs were used to measure ambient, internal, and surface temperatures of the cell by monitoring temperature dependent spectral shifts. Using a benchmark method to quantify temperature variations as a function of time following a galvanostatic pulse to the cell and extrapolation of model parameters, the approach allows the derivation of the rate of heat generated by the cell and heat flow rates under any electrochemical conditions.

Because of the sensitivity and relative accuracy of these approaches, it is conceivable that adaptations may allow for better thermal management systems, modification of electrolytes, and other factors bespoke for new cell chemistries during directly

measuring such quantities and properties within an actual cell under cycling conditions. One very practical advantage is the ability to monitor the cell under more aggressive cycling conditions (higher charging rates for example) and to decouple heat transfer and heat accumulation in real-time within 18 650 cells, and possibly other form factors too.

Another important consideration in some battery materials such as alloying phases with large volume changes during reversible Li reactions, and interfaces in all solid-state batteries (ASSBs) is the measurement and quantification of stresses and their relationship to materials and their interfaces. These effects are critical for long life performance, and this is especially important for ASSBs that use solid materials and electrolytes with pristine interfaces and no porous component to buffer any changes in internal stresses. Using FBGs and moving the sensing capability inside the battery has obvious potential benefits for localized measurements compared to sensors located outside the entire cell.

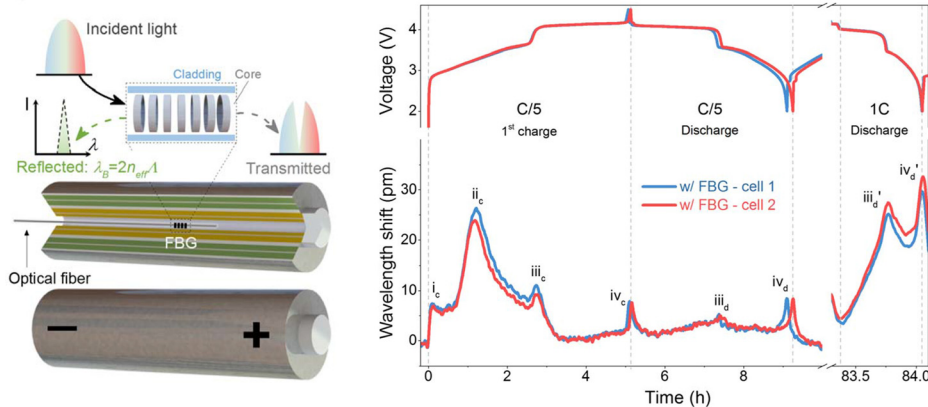


**FIG. 17.** (Left) Schematic representation of the integration of optical fiber into a 16850 battery cell. (Right) The time-resolved voltage of the cell and spectral shift from the FBG for two separate cells over a single C/5 charge-discharge cycle and also after a discharge at 1C. Spectral reflectance maxima first charge at C/5. The wavelength shift is relative to the wavelength at time = 0 h on the first charge at C/5. Adapted with permission from Huang *et al.*, Nat. Energy 5, 674 (2020). Copyright 2020 Springer Nature.

In work by Blanquer *et al.*, FBG sensors installed into Swagelok battery cells were used to directly measure internal stress evolution in liquid and solid-state electrolyte systems. Following Bae *et al.*, whose approach showed operando strain measurements using an optical fiber

grating in lithium-ion battery electrodes,<sup>192</sup> Fig. 19 summarizes the overall approach using a liquid-based electrolyte in this case, where the spectral shifts were measured at specific states of charge and discharge as time-resolved data. The optical signal was monitored during

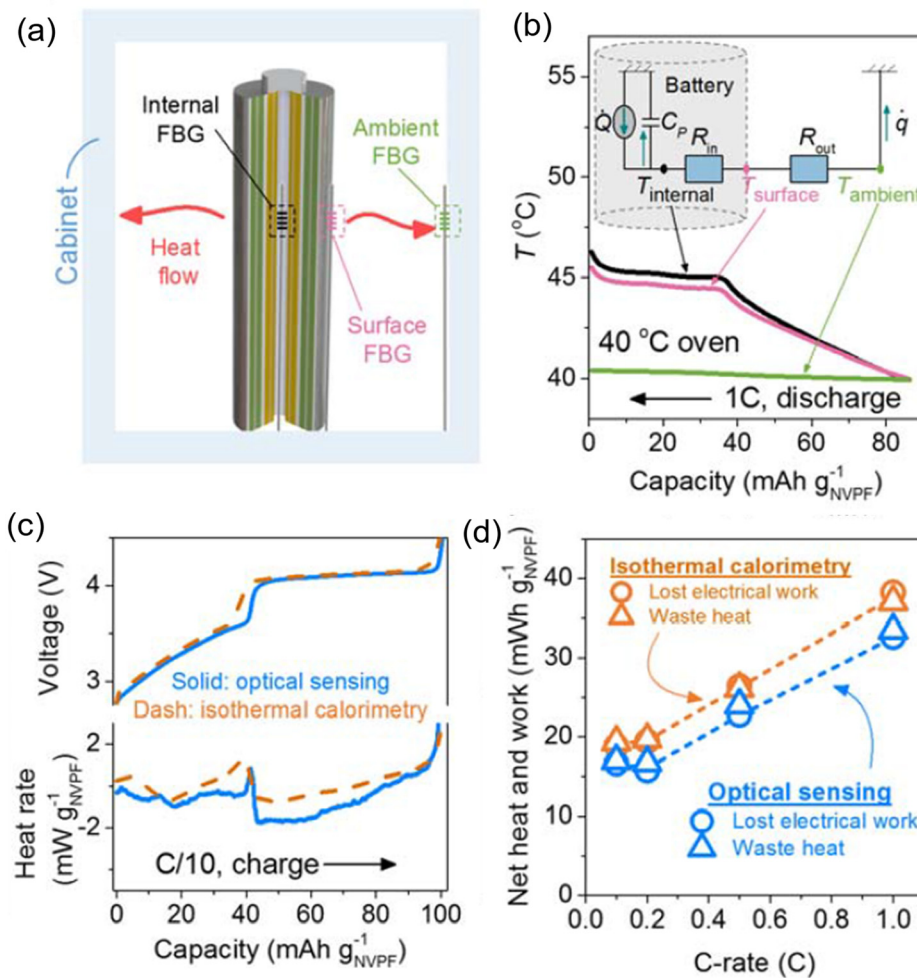


**FIG. 18.** (a) Schematic of an optical sensing calorimetry experiment. (b) The thermal equivalent circuit (inset) and the measured variables including the internal ( $T_{\text{internal}}$ ), the surface ( $T_{\text{surface}}$ ), and the ambient ( $T_{\text{ambient}}$ ) temperatures as a function of time at a discharge rate of 1C. (c) The comparison of rate of heat generation from the optical fiber method (18 650, blue solid lines) and the isothermal calorimetry (coin cell, orange dash lines) measured by the authors at a charge of C/10. (d) Comparison of waste heat and lost electrical work between the FBG approach (18 650, blue) and the isothermal calorimetry (coin cell, orange). Adapted with permission from Huang *et al.*, Nat. Energy 5, 674 (2020). Copyright 2020 Springer Nature.



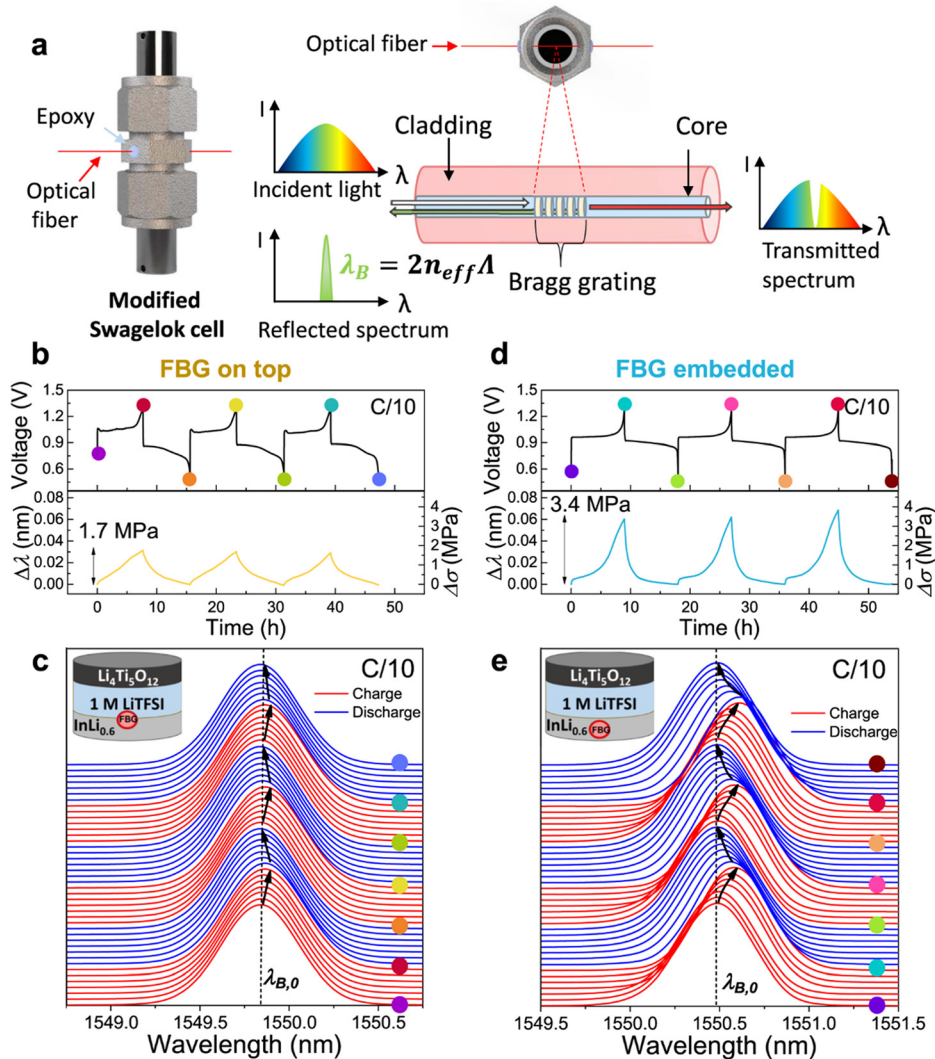


**FIG. 19.** (a) Integration of an FBG into an in-house-modified Swagelok cell with a graphical summary of the working principle of an FBG optical sensor. (b) Time-resolved voltage (top) and  $\Delta\lambda_B$  and  $\Delta\sigma$  (bottom) evolution from the FBG sensor of an  $\text{InLi}_{0.6}$ -LTO cell in a 1 M LiTFSI in DOL:DME electrolyte. The FBG was put at the anode/electrolyte interface. (c) Reflectance spectra from the FBG sensor located at the anode/electrolyte interface for the cycles shown in (b). (d) and (e) Analogous plots to (b) and (c), for a cell with the FBG sensor embedded within the  $\text{InLi}_x$  electrode. Reproduced with permission from Blanquer *et al.*, Nat. Commun. 13, 1153 (2022). Copyright 2022 authors, licensed under a Creative Commons Attribution (CC BY) License.

battery cycling, further translated into stress and correlated with the voltage profile. While the details specific to the alloying compound (In, Si) can be found in Ref. 188, we summarize here for readers some of the basic parameters that allow for spectral shift, conversion to stress data, and the basis for birefringence observations that underlie this technique. Measurements that build on these fundamentals may be possible for certain cells where open questions remain about particular materials, interfaces, or diagnostics. This may need new thinking for FBG placement, or indeed other techniques that allow operando tracking of optical responses unique to the materials, such as photonic crystals or periodically patterned electrodes. When light travels through the optical fiber, the FBG sensor acts as a reflector for a specific wavelength, namely, the Bragg wavelength ( $\lambda_B$ ), which is defined as  $\lambda_B = 2n_{eff}\Lambda$ , where  $n_{eff}$  is the effective refractive index of the FBG in its immediate environment and  $\Lambda$  is the Bragg grating period. Any temperature (T), hydraulic pressure (P), or strain ( $\epsilon$ ) change detected by the FBG sensor changes the value of  $n_{eff}$ ,  $\Lambda$  or both, which causes a shift of the reflection maxima.

Then, under a condition when the FBG is strained one can describe the shift of  $\Delta\lambda_B$ <sup>193–195</sup> as

$$\Delta\lambda_B = \left\{ 1 - \frac{n_{eff}^2 [p_{12} - \nu(p_{11} + p_{12})]}{2} \right\} \epsilon,$$

where  $\Delta\lambda_B$  is the spectra shift compared to the initial measurement,  $p_{11}$  and  $p_{12}$  are the strain-optical coefficients of the fiber being used together with the Poisson ratio,  $\nu$ . As such, the longitudinal strain measured spectrally can be converted simply to stress using Hooke's law according to  $\sigma = \epsilon E$ , using  $E$  which is the Young's modules of the fiber. In some cases, cycling a battery material may involve other directional strains, mimicking a transverse (or non-longitudinal strain) that causes a birefringent reflectance peak splitting<sup>196</sup> from different light polarization and effective index, according to Gafsi *et al.*<sup>197</sup>

$$B = \frac{|n_{||} - n_{\perp}|}{n_{eff}} = \frac{|\Delta n_y - \Delta n_x|}{n_{eff}} + B_0,$$

where  $n_{||}$ ,  $n_{\perp}$ ,  $n_y$ , and  $n_x$  represent indices for directions related to external force and the index changes due to different polarization.  $N_{eff}$  is the base effective index prior to modification. There are necessary calibrations required to effectively deconvolute peak splitting that are detailed in several publications and in Ref. 188 for calibration curves obtained for the cell at open circuit voltage (OCV). In summary, this method provides additional resolution in the analysis of *in situ* stresses in longitudinal and transverse directions with reference to the FBG on ASSB electrodes during cycling.

Operando stress measurements using FBGs has significant potential to track chemico-mechanical processes inside electrodes and at their interfaces, both for probing fundamental questions on material behavior during cycling and as a diagnostic toolset for new materials under various cycling conditions. This is important for ASSBs that rely on well-defined interfaces and tracking stress build up, in general, will require adaption of the technique to place FBG probes at optimum regions in any form factor cell that could benefit from accurate operando stress build up measurements. The key difference in the application of FBG sensing to battery systems compared to the other operando techniques discussed in this review is the incorporation of the probe inside the cell itself.

Many of the optical and spectroscopic techniques described here are inherently useful for particular measurements of electrode materials. For battery researchers and material scientists/electrochemists wishing to add these measurements to battery or energy storage device analysis suites, we have summarized some parameters that are worth considering. These range from considerations of cell assembly and electrode arrangement, resolution, benefits, limitations, and processes that could occur due to the nature of the operando optical measurement itself (Table III).

## VI. NUCLEAR MAGNETIC RESONANCE ANALYSES OF MASS SHIFTING IN BATTERY SYSTEMS

Moving to the lower energy region of the spectrum, radio frequencies can also be used to assess battery response or performance. Nuclear magnetic resonance (NMR) spectroscopy can characterize materials based on the electron density by applying an external magnetic field of strength  $B_0$  to measure the frequency at which atoms in the material achieve resonance. Magnets are rated by the radio frequencies used to cause resonance between the target nuclei and the magnetic field. The resonant frequency of the nucleus relative to the applied field is known as the chemical shift, usually measured in parts per million (ppm). Electrons orbiting the atomic nucleus naturally oppose  $B_0$ , referred to as shielding the nucleus, which determines the chemical shift. The method is useful for atoms with nonzero nuclear spin. External interactions refer to those which involve the nuclear spins (rotational movement of nucleus around its axis) and the magnetic field. Internal interactions determine the NMR spectra, dictating signal shift and line shape. These internal interactions are described in detail elsewhere.<sup>44</sup> NMR itself is not phase sensitive. For structure determination, NMR spectra must therefore be used with line shape analysis and known shift ranges.

NMR offers insight into particle sizes, crystal structure, surface changes, phase analysis, oxidation states of elements, and electrochemical performance of battery materials. While XRD provides similar information for crystalline materials, NMR proves useful for amorphous materials also.<sup>45</sup> Given batteries consist of complex material

systems under continuous modification in charging and discharging, predictions of the properties of battery materials using theoretical approaches, such as density functional theory<sup>204</sup> and Hartree Fock computational methods, have been effective and useful predictors in tandem with NMR experiments.<sup>205,206</sup> The combination of NMR and diffraction methods can be extremely powerful, as the techniques provide short-range, local structure information, and long-range information, respectively. Insight into crystal and electronic structure can be provided simultaneously. NMR proves useful regardless of the charge storage mechanism, given that alloying, conversion, and intercalation mode cathodes all involve significant structural changes and phase transformations during cycling.

Real-time, nondestructive NMR measurements are required to adequately assess the evolution of the battery during electrochemical cycling. For *in situ* NMR measurements, self-relaxation processes are minimized, high chemical specificity can be achieved for both crystalline and amorphous materials, and both short-lived and metastable phases can be tracked. *Ex situ* NMR can be used to streamline the *in situ* experiments by selecting the relevant NMR parameters to study for well characterized materials. The *in situ* approach has its limitations; it is performed under static conditions such that sample spinning is not an option. Therefore, cell design, hardware, detection, and analysis methods require additional development.

In Key *et al.*,<sup>207</sup> a range of NMR techniques used to probe local structural changes during discharge of crystalline silicon in a working LIB are described. Figure 20 shows the stacked *in situ* NMR spectra obtained, at a range of capacity levels, revealing the change in composition of the electrodes at each SoC. The work outlines the benefits of using the combination of NMR and diffraction methods as a diagnostic tool for battery electrodes. Similarly, the advantages of using the combination of *in situ* and *ex situ* analysis are shown, along with the accompanying complications that arise in the setup of the required system. The data obtained provided the ability to streamline *in situ* NMR measurements. The *in situ* NMR measurements detected phases that were not observed in the *ex situ* data, a clear indication that amorphous phases form during the cycling of Si electrodes in LIBs. Dynamic processes that are short lived or metastable and therefore not accessible via *ex situ* methods are captured. While analysis can prove difficult due to the extremely short timescale of the interactions involved, NMR is well suited to nanosecond to sub-nanosecond time domains.

The key result here is that the combination of *in situ* and *ex situ* NMR with knowledge of the structural and electrochemical processes at work provides a useful way of investigating the processes that occur in the vicinity of the electrodes in an LIB, especially processes related to the formation and passivation of the SEI layer. The requirement for a more sophisticated methodology design for *in situ* measurements compared to traditional NMR measurements is evident, including the inclusion of a flexible electrochemical cell to facilitate the *in situ* probe.

In applying NMR to battery materials, the interfaces between the electrodes and the species with which they react (e.g., electrolyte and SEI layer) have a significant impact on performance. Decomposition products are one of the primary factors that dictate ion transport through interfaces and the electrolyte, ultimately determining energy density. Interference in NMR spectra is often caused by dendrite formation, which can lead to short circuiting and battery failure. Efforts to combat these effects in various battery systems are widely

**TABLE III.** Novel cell designs and key characteristics for experimental optimization in the application of operando optical spectroscopy techniques to battery systems.

Technique	Operando cell setup	Capabilities	Limitations	Local resolution
Raman spectroscopy	One-sided: Pyrex window <sup>98,198</sup> Quartz window <sup>99</sup> ECC-Opto-Std with borosilicate window <sup>104</sup>	Phase detection Degree of disorder at molecular level Nanoparticle size Indication of degree of crystallinity	Applicable only to polarized species Interference to electrode signals due to electrolyte species	0.5–1 $\mu\text{m}$
FTIR spectroscopy	ATR-FTIR cell based on: Single-crystal Si, Ge <sup>115,118</sup>  Diamond/ZnSe/steel ATR module <sup>117</sup> Si wafer window <sup>199</sup> Diamond disk <sup>200</sup> KBr window <sup>201</sup>	Transmission measurements provide bulk information on bulk properties of electrode/electrolyte  ATR provides high surface sensitivity measurements at the electrode/electrolyte interface  Spectral identification of organic and inorganic species on surfaces or in liquids/electrolytes	Applicable only to species with a net change in dipole moment Detectors can require cryogenic cooling-liquid nitrogen (e.g., MCT for mid-IR) and liquid helium (e.g., Si, Ge bolometers for far-IR) Requires computational processing via Fourier transform  Issues with side-by-side electrode geometry and electrolyte wetting  Possibility of higher resistance current collectors not mimicking real-world cell behavior	0.001–4 $\text{cm}^{-1}$
Optical spectroscopy	Transmission/reflectance: Flooded glass cell <sup>175</sup> Modified Swagelok cell <sup>202</sup>  “Coffee bag” cell with glass window <sup>203</sup>	Optical fingerprint monitoring  Macroscopic stress evaluation Detection of changes to the photonic lattice parameters including inter-planar spacing Indication of swelling and electrode material degradation Determination of degree of disorder Detection of luminescence and quenching from nanomaterials Thickness variation from angle-resolved data and effective index measurements	Requires highly ordered materials for a photonic bandgap  Attenuation of photonic response by cell components and electrolyte species Flooded cell can result in delamination of electrode material Reflectance mode cells require large incident angle measurements which deviate from Bragg–Snell model Careful measurement of reflectance, transmittance, extinction (where relevant) and background signals	$\sim 0.3 \text{ nm}$
Fiber Bragg grating (FBG) sensors and probes	FBG-embedded modified Swagelok cell <sup>188,189</sup> FBG-embedded composite laminate <sup>187,190,192</sup>	Optical and calorimetric sensing  Internal sensing of materials  Access to stress-strain and mechanical properties High sensitivity Stable under aggressive cycling conditions	Highly dependent on form factor, specific fiber design for each battery	n/a

researched.<sup>208–211</sup> This phenomenon occurs in lithium and sodium cells with metallic anodes during cycling. One of the limitations of NMR is that the penetration of RF fields used to excite nuclear transitions is severely limited through metal samples because of an effect known as skin depth. Skin depth is assumed to be an order of

magnitude larger than dendrite thickness. Therefore, signals penetrate dendrites fully but appear constant relative to the signal of the bulk metal.<sup>212</sup> Identification of microstructural characteristics, growth mechanisms, and contributory factors is required to minimize this interference during *in situ* NMR experiments to provide a better



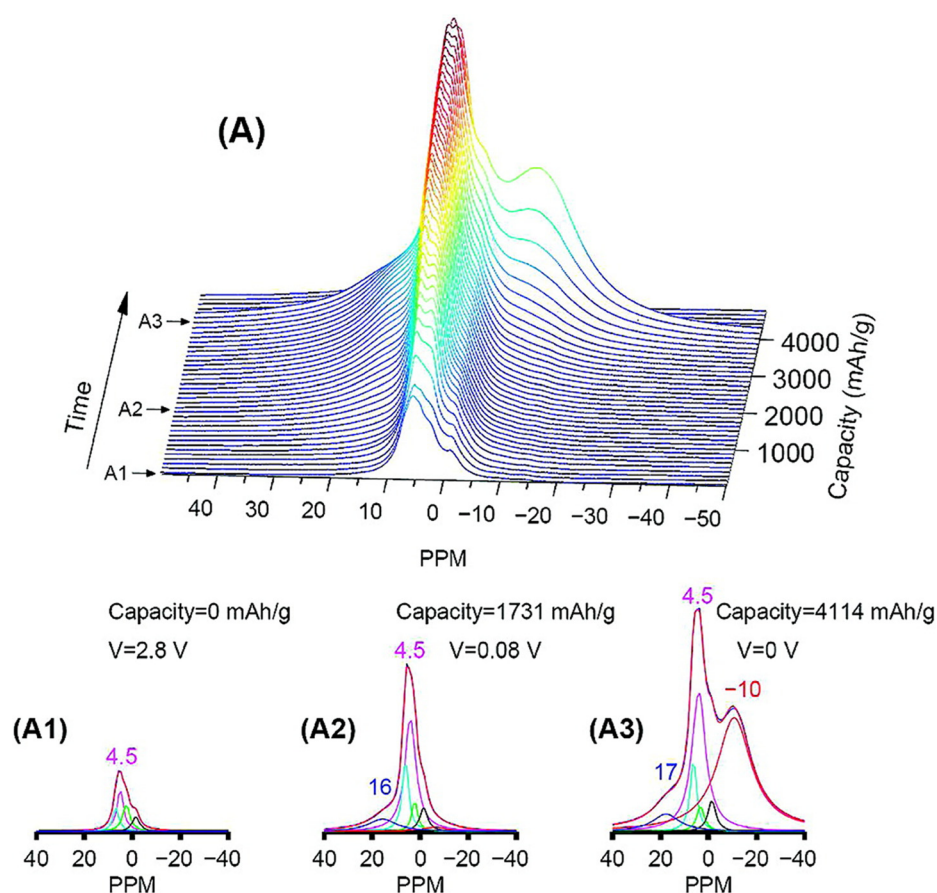


**FIG. 20.** (A) Stacked plots of *in situ*  $^7\text{Li}$  static NMR spectra of the first discharge of an actual crystalline Si vs  $\text{Li}/\text{Li}^+$  battery (the color bar shows the relative intensity scale for the spectra). (A1)–(A3) Deconvoluted spectra at various discharge capacity values of interest. Reproduced with permission from Key *et al.*, J. Am. Chem. Soc. **131**, 9239 (2009). Copyright 2009 American Chemical Society.

insight into the evolution of the microstructures leading to electrode degradation.

Lithium metal batteries (LMBs) are being investigated with renewed interest for higher energy density future battery systems.<sup>213–215</sup> Lithium metal is well known to have the highest theoretical specific capacity of all lithium-ion anodes and low negative potential. In LMBs, charging and discharging involves the deposition and stripping of Li metal for each process, respectively. Capacity retention, cycling stability, and fire hazards are the key issues for in service LMBs, which can all be attributed to Li dendrite growth, but many examples of these batteries are deemed safe. Li dendrite growth and the factors that affect it for LMBs being investigated in new form factor cells or at nonstandard temperature, or at higher charging rates can be difficult to accurately track and examine in real-time during battery operation. Figure 21 depicts the stages of Li dendrite growth in tandem with SEI formation, the predominant mechanism leading to short circuiting in LMBs.

Gunnarsdóttir *et al.* demonstrated an *in situ* NMR metrology where an anode-free LMB setup was employed.<sup>216</sup> The typical Li metal anode was absent, meaning that Li was plated directly onto a bare copper current collector from a  $\text{LiFePO}_4$  cathode. The build-up of dead Li and the evolution of the SEI layer were tracked by *in situ* NMR. While traditional performance analysis techniques detect only the capacity losses of the system, *in situ* NMR can be used to deconvolute

individual capacity drops to pinpoint their sources. *In situ* NMR can detect the bulk magnetic susceptibility (BMS) shifts caused by Li metal and determine the location and environment of the sources of capacity losses by providing information on the density of surface coverage of the current collector in its various environments. In this study, the environment is varied using different electrolytes and coatings. SEI

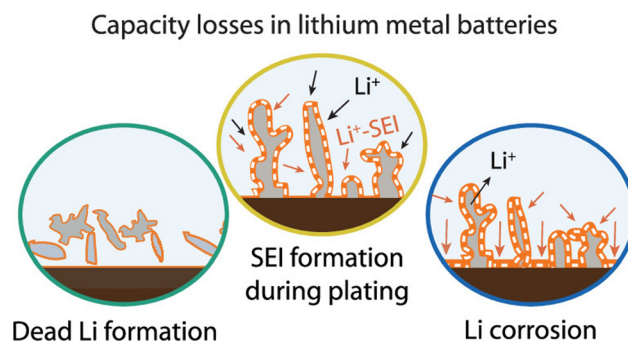


**FIG. 21.** Lithium dendrite growth: Schematic depicting the SEI build-up and dead Li formation at the electrode/electrolyte interface. Reproduced with permission from Gunnarsdóttir *et al.*, J. Am. Chem. Soc. **142**, 20814 (2020). Copyright 2020 authors, licensed under a Creative Commons Attribution (CC BY) License.

formation is of paramount importance during cycling of a battery, yet its evolution can either be key in optimizing performance or detrimental to it. By monitoring the surface coverage of the current collector, the effects of the SEI layer on performance can be determined. Figure 22(a) shows the Cu-LiFePO<sub>4</sub> cell before cycling, and the NMR spectrum shows the diamagnetic peak corresponding to the SEI and Li<sup>+</sup> ions, with the spectrum region associated with Li metal highlighted to show its absence.

The schematics in Figs. 22(b)–22(d) show the cell at different stages of cycling, with a depiction of the accumulation of dead Li over time. The NMR spectra associated with each stage are also shown. For a system with no dead Li deposited, peaks in the NMR spectra acquired after discharge are suppressed or absent, i.e., the stripping phase. The spectra clearly demonstrate the build-up of dead Li as the number of cycles increase. A continuation of this trend would lead inevitably to contact between anode and cathode, resulting in short circuit and system failure. The results of this study highlight the significant advantages in using *in situ* NMR metrology to analyze battery degradation processes such as Li dendrite growth. The anode-free cell removed some of the complications of NMR methods for battery cells,

like the issue of spacing between electrodes within the cell and effectively locating Li metal build-up. Potential solutions were also examined in the form of metal coatings, additives, and artificial SEI. Once again, *in situ* NMR applied to the anode-free setup can be used to track the dead Li formation for each environment. Going forward, the versatility of this approach is evident. Small alterations can allow its extension to Li–S and Na metal batteries and operando studies. The fact that disassembly of the cell was not required means that the approach in this study can be added to the arsenal of nondestructive techniques for monitoring battery electrode degradation mechanisms in real-time.

The geometry and composition of commercially used battery cells render many direct NMR methods less effective in examining battery performance. The spacing between electrode layers and conductive casings prevent the penetration of the radio frequencies required to induce nuclear transitions. In Pigliapochi *et al.*,<sup>217</sup> an ultrafast, inside-out magnetic resonance technique is used for the assessment of rechargeable cells. Here, cell classification is performed via a single shot free induction decay (FID) NMR spectrum acquisition of the liquid compartments surrounding the cell. Changes in magnetic

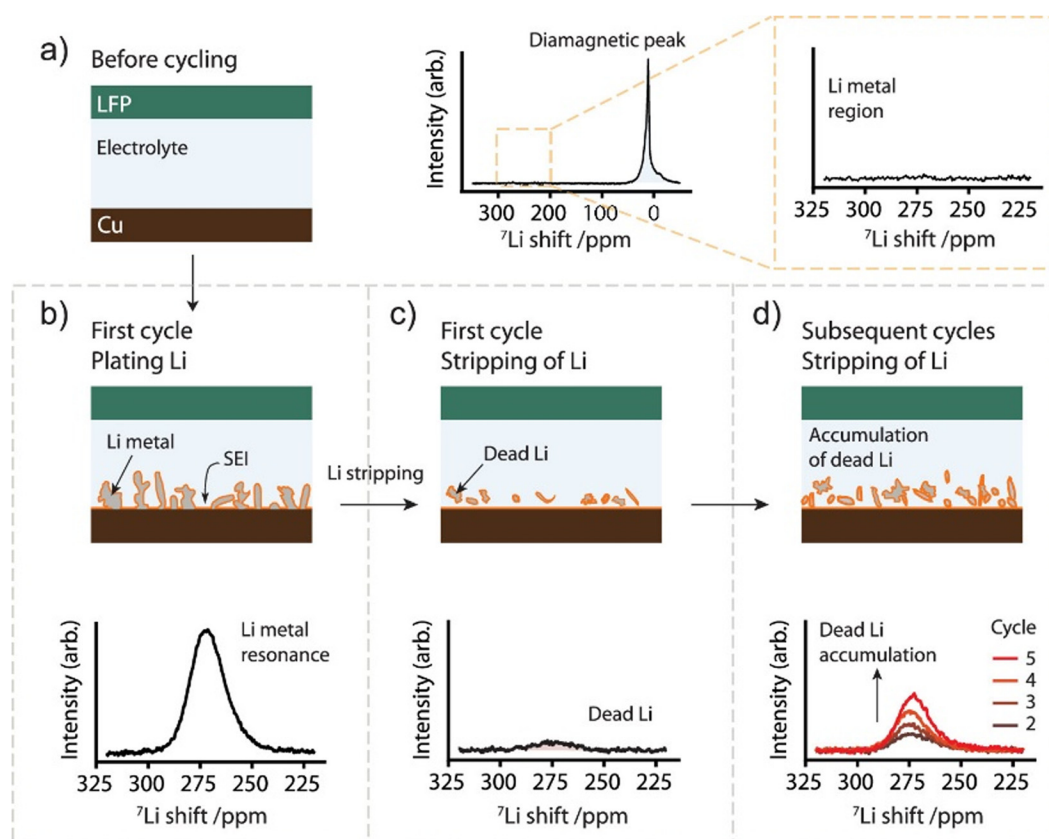


**FIG. 22.** Schematic of the <sup>7</sup>Li *in situ* NMR technique used to study dead Li formation and the resulting <sup>7</sup>Li NMR spectra. (a) The Cu-LiFePO<sub>4</sub> (LFP) cell before cycling and the corresponding <sup>7</sup>Li NMR spectrum showing the resonance of the diamagnetic Li (the SEI and Li<sup>+</sup> ions) and the absence of the Li metal peak. (b) Charging the cell results in Li deposition, as shown in the <sup>7</sup>Li NMR spectrum of the Li metal region. (c) At the end of discharge, the Li metal signal can still be observed, which is attributed to dead Li. (d) Further cycling of the Cu–LFP cell results in an accumulation of dead Li over the next cycles (cycle 2–5), the intensity of the Li metal signal increasing at the end of stripping in each cycle. Reproduced with permission from Gunnarsdóttir *et al.*, J. Am. Chem. Soc. **142**, 20814 (2020). Copyright 2020 authors, licensed under a Creative Commons Attribution (CC BY) License.

susceptibilities occur due to changing oxidation states in the electrode materials during charge and discharge. The method provides a non-invasive cell classification based on cathode material, volume of electrolyte, and cycle life, while also presenting an overview of the ageing model of the system. A schematic of the operando cell design is shown in Fig. 23(a). The system is simply placed inside an NMR probe with its  $z$  axis aligned with the magnetic field. The cell was probed using inside-out magnetic resonance imaging (ioMRI), described in detail elsewhere,<sup>218</sup> prior to NMR measurements. However, there are limitations to the ioMRI approach. As strongly magnetic materials, like those used as battery cathode materials, cause distortions in the magnetic imaging. The limitations of the ioMRI technique can be avoided using FID NMR spectroscopy.<sup>219</sup> Instead of obtaining a series of images, spectra are acquired in one fast, single-shot readout lasting less than a second. The speed of the technique allows access to the fast relaxation regime, negating the effects of large magnetic field gradients. Figure 23(b) shows the  $^1\text{H}$  NMR spectra obtained at 2.5 V for the three cells of different cathode materials. The  $^1\text{H}$  NMR spectra acquired at successive states of charge in one of the cells is shown in Fig. 23(c). The change in chemical shift and signal intensity due to lithiation during the charging cycle is indicated by the black arrow.

Principal component analysis (PCA) is used to classify groups of measurements based on the few strongest-contributing features of the dataset, which are the principal values, and is useful in the diagnosis of energy storage mechanisms.<sup>220</sup> The results from PCA applied to the  $^1\text{H}$  NMR spectra acquired are presented in Fig. 23(d). A clear trajectory with charging is observed for each cell. The trajectories of cells of the same cathode component and different electrolytes or cell age are grouped together (blue lines), while there is a significant difference between cells of different cathode components. The PCA analysis shows that cell classification based on cathode materials as a function of state of charge is an effective approach while electrolyte amount and cell age have little influence on the results.

The ultrafast inside-out NMR technique is depicted as a fast, robust, nondestructive method for examining battery electrode materials *in situ*. The versatility of the setup means that it can be extended to operando studies in the future. The applicability of *in situ* NMR and MRI techniques to commercial cells has proven difficult to date, calling for novel adaptations to their methodology.

The application of NMR to battery materials proves powerful for determining particle dimensions, oxidation states of constituent elements, and changes at the surface. Its applicability to both crystalline

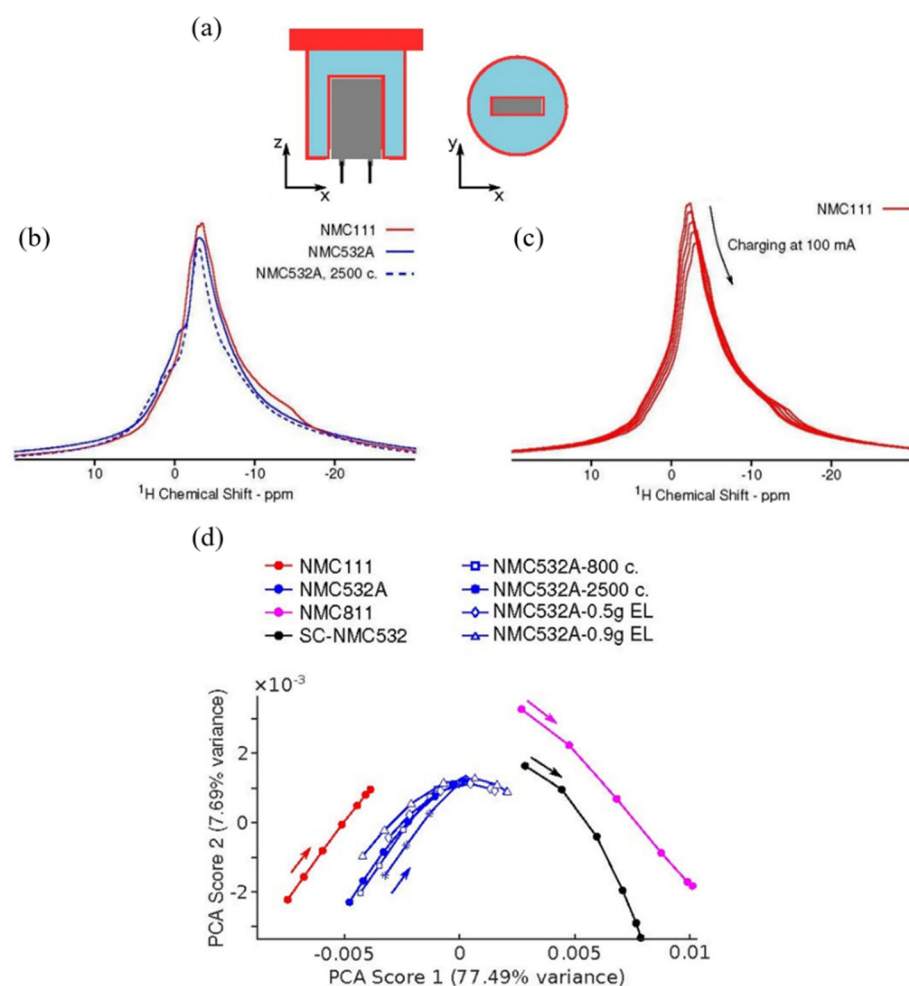


**FIG. 23.** (a) Schematic of 3D-printed holder (red) used for ioMRI and NMR. The holder contains the cell (gray), which is surrounded by water compartment (light blue). The system is placed inside an NMR probe with the  $z$ -axis aligned with the static magnetic field. The vertical and horizontal cross sections are shown left and right, respectively. (b)  $^1\text{H}$  NMR spectra taken at 2.5 V for cells containing, as cathode: NMC111 (red line), NMC532A (blue solid line), and NMC532A already undergone 2500 cycles prior to the MRI (blue dashed line). (c)  $^1\text{H}$  NMR spectra taken at intervals during charging of the cell containing NMC111 as cathode. The black arrow shows the direction of shift of the spectra as the cell undergoes charging. (d) Principal component analysis (PCA) performed on the  $^1\text{H}$  NMR spectra of all the cells. Each arrow indicates the direction of the trend(s) of the corresponding color as the cell is charged. Adapted with permission from Pigliapochi *et al.*, Batteries Supercaps 4, 322 (2020). Copyright 2020 Wiley-VCH.



and amorphous materials is useful, such as in cases where XRD has been used for phase detection and failed to capture the full picture due to the presence of non-crystalline phases, such as those corresponding to SEI species and intermediate phases that occur especially in conversion materials during cycling. For metallic materials, NMR provides the ability to spatially resolve areas in which build-up of dead Li (or Na, K, etc.) occurs. Its widespread incorporation for battery system analysis is limited by the difficult nature of cell design, with dimensions on an insufficient scale to accommodate the radio frequency penetration that is required to induce nuclear transitions. In the case of NMR, the local resolution is directly proportional to the signal acquisition duration, which determines the linewidth of the corresponding peaks.<sup>221</sup> Resolution is species dependent, where spectral regions of overlapping peaks prove difficult to deconvolute. Traditionally deconvolution can be simplified in cases where magic angle spinning (MAS) NMR can be used instead of its static counterpart. However, MAS NMR cannot be used for *in situ* measurements of current battery technologies. For *in situ* measurements, the spatial resolution is limited by the length of the radio frequency detection coil inserted into the cell.<sup>222</sup> The nondestructive nature of NMR is a significant motivation for its application to sensitive, thin film battery materials, especially for the researcher concerned about beam damage inherent to electron microscopy and x-ray techniques.

## VII. ELECTROCHEMICAL-ACOUSTICS: LISTENING TO A BATTERY'S HEALTH

In recent years, the advantages of radio frequencies have also been demonstrated using electrochemical-acoustic methods to monitor the properties of battery materials, particularly SoC and state of health (SoH). Most of the techniques discussed thus far involve the interaction of the material with a form of electromagnetic energy—x-rays, UV-vis range photons, and infrared light. One of the main disadvantages common between these techniques is their applicability to electrolytes and gaseous species due to their poor scattering properties.<sup>141,223</sup> Acoustic measurements are obtained by applying a series of ultrasonic pulses to the system which can be monitored nondestructively in real-time. Evidence points toward a relationship between ultrasonic transmittance parameters and battery SoC/SoH.<sup>109,224,225</sup>

Ultrasound transmission is highly sensitive to gas, porosity, and the mechanical properties of materials. The general approach used to probe battery SoC includes examination of the relationship between ultrasonic transmittance and the evolution of some of the key physical parameters of the materials.<sup>108,175,226</sup> Changes in the physical dynamics of the system affects the electrochemical activity in the cell and ultimately determines both SoC and SoH.

Operando acoustic time-of-flight (ToF) modeling and experiments are employed in Hsieh *et al.* to correlate structural changes to electrochemical performance.<sup>227</sup> The overarching advantages of the technique are in its simplicity and universal applicability. A combination of modeling and experimental measurements creates a framework relating the distribution of density within a battery system to its SoC and SoH. A representative battery stack used for modeling is shown in Fig. 24(a), with the same setup used for experimental measurements.<sup>228</sup> The setup consists only of the battery and two transducers, one operating in pulse/listen mode and the other only in listen. Unlike the other techniques discussed in this review, the effectiveness of acoustic measurements is independent of the battery chemistry or

form factor. The SoC–density relationship can be interrogated since density within the cell affects the speed of the penetrating ultrasonic waves. The speed of sound  $c_s$  through a solid material is a function of the elastic modulus  $E$  and density of the medium  $\rho$ , given by the Newton–Laplace equation  $c_s = \sqrt{\frac{E}{\rho}}$ . Therefore, these two properties

govern the speed of the ultrasonic waves that travel through each layer of battery material. A description of the computational model used to simulate the battery stack can be found elsewhere. Strong correlations between SoC and distribution of density within the cell are shown. Furthermore, SoC–density correlations indicate underlying physical processes that occur in electrodes during cycling. A layer-by-layer examination describes mechanical degradation (and evolution) within the cell. Figures 24(b)–24(i) summarize the results of the study, with a clear correlation between the acoustic and electrochemical properties of the LiCoO<sub>2</sub>/graphite pouch cell during galvanostatic cycling.

Figure 24(e) shows the sum of all transmitted and reflected waves received by the transducers in green and red, respectively. As the battery is discharged, acoustic absorption increases, which results in a decrease in transmitted and reflected intensity. An exception occurs at end of discharge. The authors attribute this to the capacity-limited cathode. Near 0% SoC (full discharge), LiCoO<sub>2</sub> undergoes a hexagonal-to-monoclinic phase transformation, which dramatically changes both the density and bulk modulus of the cathode, leading to a spike in both the transmitted and reflected acoustic intensities.

Cyclic voltammetry and differential capacity plots can provide an electrochemical fingerprint of a battery system. Light transmission and reflectance spectra can provide an optical fingerprint of battery electrode materials. Here, it is shown that ultrasonic measurements can provide an acoustic fingerprint of the battery system under analysis in real-time using a simple methodology in a nondestructive fashion. The acoustic fingerprint is denoted by the ToF of the waves which occur in discrete materials based on the density within the cell. Change in lithiation and therefore SoC alter the acoustic fingerprint, changes which with further research can potentially be quantified based on the change in density and modulus of the material. Currently, there are significant limitations to the model. Many assumptions are made, such as the exclusion of many known non-linear processes which occur during cycling, along with more cell layers.<sup>229,230</sup> Beyond SoC, density changes indicate underlying physical processes affecting electrode degradation. ToF echo profiles and acoustic signal amplitudes shown as a function of cycle number are key indicators of battery SoC and SoH, indicating inter- and intra-particle stress and strain along with alterations to layer composition of the cell. Physical correlations for large-scale, complex, commercial batteries that have only been probed using high energy x-ray techniques to date are achieved. The method is a fraction of the cost of photonic analysis and negates the need for electrical contact.

Ultrasonic transmittance is particularly useful for detecting wetting and dewetting phenomena in Li-ion cells as the presence or absence of the electrolyte at any given position has a significant effect on the ultrasonic transmission at that point. Dewetting in his context refers to the swelling of an electrode stack to the point where there is insufficient electrolyte to completely fill the expanded pore space, a phenomenon that occurs as lithium intercalation of IO electrodes occurs during LIB operation. Unlike the techniques discussed previously where initially the techniques are applied *ex situ* and then the required adjustments (e.g., cell design) are made to obtain *in situ*

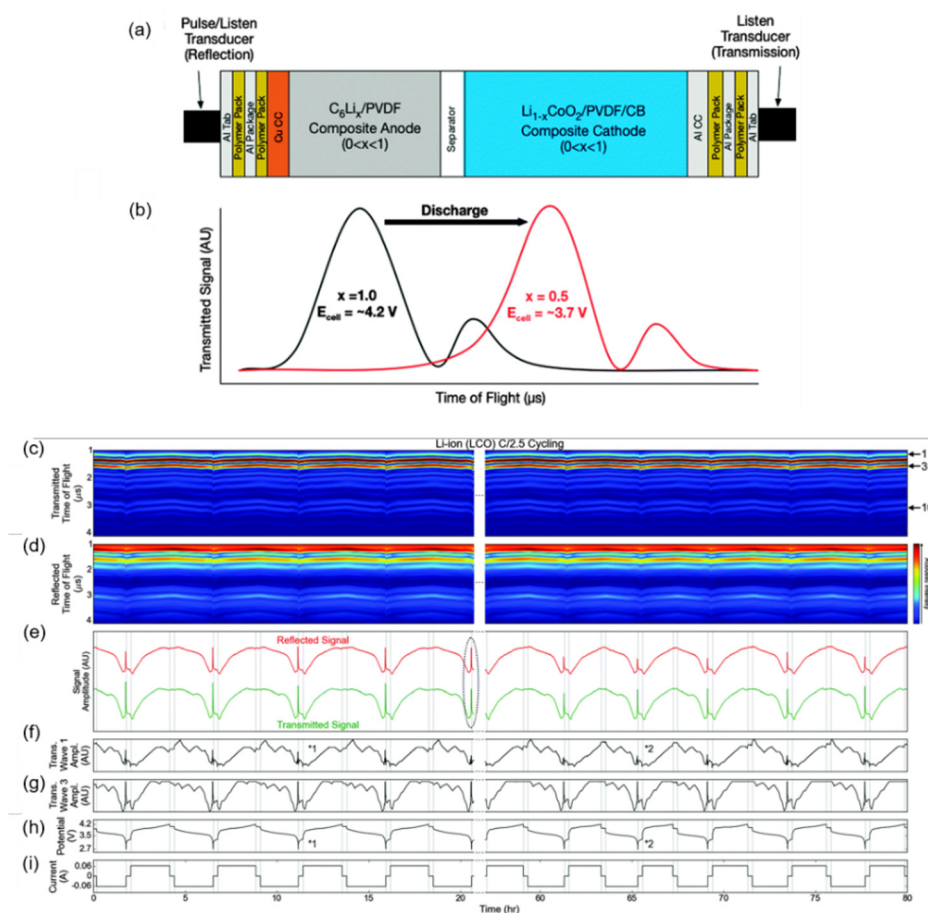


**FIG. 24.** Ultrasonic probe of a representative battery. (a) Schematic representation of the battery stack used for acoustic modeling and experimental measurements, shown with packaging, current collector, electrode, separator layers, and two acoustic transducers. (b) Example illustration of the increase in time of flight (ToF) of the transmitted signal as a function of SOC that occurs during discharge; this shift is a result of the changes in electrode densities as the SOC (i.e., Li content,  $x$ ) changes. Acoustic behavior of a  $LiCoO_2$ /graphite prismatic cell. (c) and (d) ToF maps for transmission and reflection modes, respectively, (e) total reflected (red) and transmitted (green) signal amplitudes, (f) and (g) traces for the amplitudes of transmitted waves 1 and 3, respectively, (h) cell potential, and (i) applied current as a function of cycling time. The vertical gray lines in panels (e)–(i) represent transitions between charge, discharge, and rest steps. From D. A. Steingart, *Instrumentation and Measurement*. Copyright 2020 Physics World. Adapted with permission from IOP Publishing.

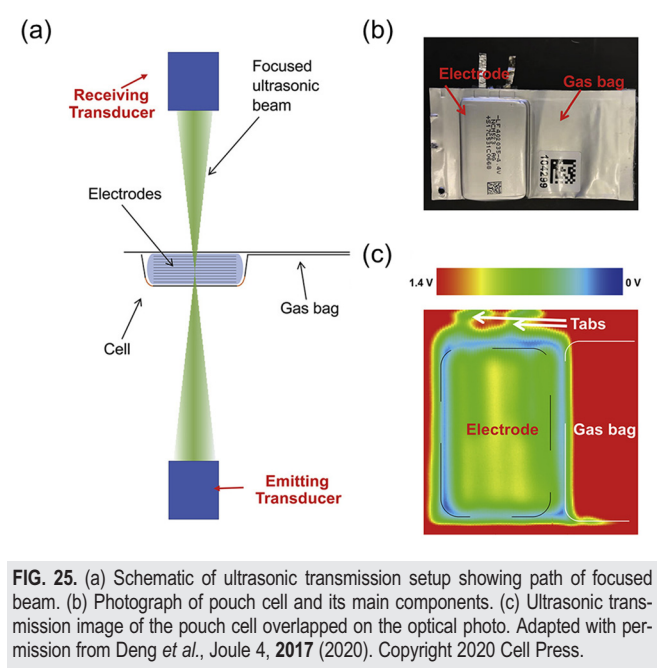
measurements, the ultrasonic transmission method is *in situ* (and *operando*) by nature. In this case, the advancements that have been made to the analytical power of the technique have been in its spatial resolution.

Earlier reports employed a fixed-point method, where the ultrasonic transmittance was measured using a beam focused on a particular point or multiple successive points across the cell, providing results averaged over the area of the cell.<sup>202,231</sup> These approaches limited the spatial resolution as the beam width was too wide to probe the micro-scale structural features, which are formed and changed during cycling of a Li-ion cell. One route that has shown success is the use of acoustic measurements to identify defects within battery systems and use complementary techniques to analyze the properties of the defects. Robinson *et al.* used ultrasonic time-of-flight analysis to identify defects and SoH in a Li-ion pouch cell, by examining the acoustic transmission signal through the cell and x-ray tomography was used to determine the location and scale of the defects.<sup>232</sup> Several studies have taken a similar approach, using ultrasonic transmittance measurements to probe a certain physical/structural change while also being probed using complementary techniques.<sup>202</sup>

A state-of-the-art approach to *operando* ultrasonic analysis of the Li-ion cells was taken in Deng *et al.*, with an ultrasonic scanning approach that employed a narrow beam with a diameter less than

1 mm that provided sub millimeter resolution. The beam was scanned across the cell with a position control accuracy of 0.2 mm.<sup>233</sup> Here, complementary techniques were not required. Figures 25(a) and 25(b) show a schematic and photograph of the setup used for the ultrasonic scanning of electrolyte wetting and dewetting in a Li-ion pouch cell.<sup>41</sup> Gassing and dewetting can be observed in aged cells, which helps to explain their loss in capacity after extended testing. A full map of the ultrasonic transmittance throughout the cell is shown in Fig. 25(c). The ultrasonic scanning technique developed here is cheap, fast, non-destructive and can be applied to large pouch and prismatic cells to monitor the degradation of Li-ion cells on an industrial scale.

Ultrasonic transmittance measurements can be used to monitor the electrochemical-acoustic behavior and the underlying physical processes can be interrogated in real-time using a cheap, simple, non-destructive method that can be integrated easily into electric vehicles and mobile devices. Acoustic monitoring lacks the ability to resolve microstructural electrode features due to the relatively large photon wavelengths. While the method does not compete with capability of the higher energy techniques for microscopic examination, acoustic measurements constitute a valuable addition to the arsenal of the battery analyst on the lower end of the energy spectrum for electrode size length scale, providing the ability to listen to a battery's health during operation. Acoustic sensing at cell-level length scales has the advantage



of being relative simple. Nondestructive in nature, measurements can be acquired without requiring state-of-the-art cell designs or cell disassembly. Insight into the degree of wetting within is of major importance to experimental-phase cell methodologies, and new materials, where the structural specifications result in an ambiguity surrounding the extent to which the electrolyte infiltrates the corresponding electrode materials (Table IV).

VIII. BATTERY OPERATION IN A DYNAMIC SERVICE ENVIRONMENT: BUILDING A SENSOR NETWORK

While operando analysis of individual cells and their components provides information on battery performance, it is also necessary to examine batteries under dynamic conditions. Operando measurements tend to be performed under optimal conditions in a lab-based setting. Often, batteries are used as components of larger battery pack systems. In Li *et al.*,<sup>242</sup> Li-ion battery monitoring was performed operando using a sensor-based network. The network was used to examine the effects of vibration and impact on battery performance during cycling, to provide a simulation of the conditions the system may experience during transport. The relationships of both temperature variance and deformation to capacity degradation during cycling in various dynamic environments are established. The network identifies critical points during cycling where high heat generation and stress

TABLE IV. Summary of the application of state-of-the-art operando techniques based on low energy radio wave penetration of battery systems.

Technique	Operando Cell Setup	Capabilities	Limitations	Local Resolution
Nuclear Magnetic Resonance (NMR) Imaging	Bellcore-type flat bag cell <sup>234–237</sup>	Particle sizes	Skin depth effect	Spatial:
		Surface changes		< 1 cm <sup>226</sup>
	Swagelok-type cylindrical plastic cell capsule <sup>238</sup>	Elemental oxidation states	Dendrite interference	
		Applicable to amorphous materials		
Electrochemical-Acoustic Time-of-Flight (ToF)	Pouch cell <sup>44,230,239–241</sup>	Spatial resolution of dead Li build-up	Radio frequency penetration difficult due to cell components/ dimensions	Temporal:
			Resolution limited by RF detection coil	3 ns – 20 ns
	Cylindrical cell <sup>227</sup>	Shifting of mass within cell	Inapplicable to resolution of microstructural features	
		Detection of electrode material dewetting	More detailed model required to decouple individual events	
	AA alkaline cell <sup>227</sup>	Monitoring of electrolyte gassing		Spatial:
		Applicable to any battery chemistry or form factor		< 1 mm
		Intraparticle and interparticle stress and strain		
		Performance without electrical contact		



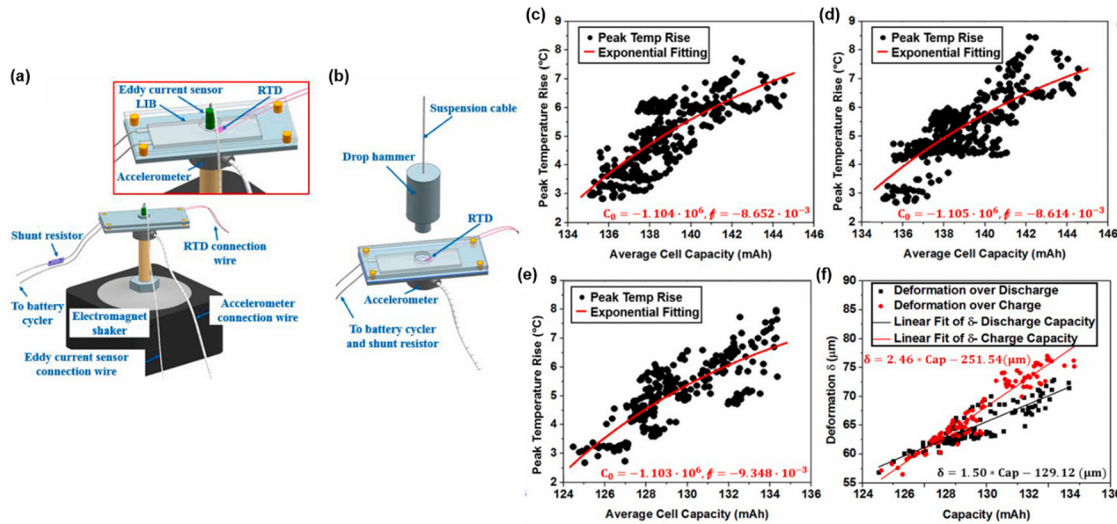


**FIG. 26.** Operando testing platform for LIBs: (a) setup for operando vibration test and (b) setup for operando impact test analysis. Relation between maximum temperature increase and capacity of (c) cell 1, (d) cell 2, and (e) cell 3. Relation between maximum deformation and capacity of cell 3. Reproduced with permission from Li *et al.*, J. Power Sources **486**, 229349 (2021). Copyright 2021 Elsevier B.V.

accumulation may lead to thermal runaway and potential explosion. The comparison between single cell and battery pack performance is also explored.

In Fig. 26, the operando testing platform used for (a) the vibration test and (b) the impact test of the LIBs is shown. An electromagnet shaker was used to simulate vibration, while a drop hammer simulated impact. In the sensor network, capacity degradation was measured using the internal resistance temperature detector (RTD) and eddy current sensor. Vibration and impact testing investigated the changes in battery capacity over the typical service life of 500 cycles.

The testing results showed capacity retention immediately after impact, with gradual capacity degradation observed after continuous cycling. Low momentum impact can release compressive stress in the electrodes, while high momentum impacts can cause severe cracking, each leading to degradation and capacity loss. The evidence indicates that dynamic loading has little effect on battery performance in the short term, but repeated stress leads to electrode degradation and battery failure.<sup>242</sup>

Cell deterioration and the role of electrode degradation is explored in this work by examining the relationships between capacity and two of the key physical properties which affect it, temperature change and deformation, for both a single cell and two-cell pack. In Figs. 24(c)–24(e), the temperature–capacity relationship is shown for each of the three cells. The relationship provides an indirect method to measure temperature, eliminating the requirement for dedicated temperature monitoring, reducing the number of components consuming power in the network, and reducing cost. However, for a multi-cell battery, the effects of adjacent cells must also be considered. Figure 24(f) shows the deformation–capacity relationship, specifically on the structural changes to the cell. Following the theme of this review, the study links structural changes to the electrochemical processes which occur during cycling, via operando analysis. For the sensor network designed here, deformation indicates the level of stress accumulation during service which can lead to dendrite formation causing internal

short circuits. The evidence shows greater deformation occurs during charge than during discharge, which causes the cell to swell over its cycle life. The overall deformation growth can be attributed to several factors. These factors can be broken down into two categories: gas generation and electrode thickness change. By mapping deformation to electrode thickness change, the role of electrode degradation to cell performance can be established. The sensor network can not only detect degradation but identify and quantify its source. Here, the results show that deformation is greater than thickness change, which occurs only in the graphite anode and not the lithium cobalt oxide (LCO) cathode. The results demonstrate that anode degradation and gas generation (due primarily to electrolyte decomposition) are the key factors leading to deformation of the cell.

As the inevitable move toward renewable energy gains momentum, energy storage requirements mean that battery performance assessment methods must fall behind. The use of a sensor network as described above which can pinpoint performance issues in a multi-cell configuration can support the employment of battery systems at the grid level, a key component in the move toward global decarbonization. The methods outlined in this short review highlight how many cross-disciplinary studies are now being conducted to benefit the electric future, from materials choice and abundance, to long-term high performance battery response, while in parallel gaining better understanding of issues and safety concerns from new battery chemistry and designs to detailed microstructure, interface and localized reactions that govern, control, improve, and impede safe, efficient cyclic charging and discharging over a long lifetime.

## IX. CONCLUSIONS AND OUTLOOK: WHERE OPERANDO METHODS MATTER TO BATTERY DEVELOPMENT

Many of the achievements using operando XRD, NMR, and synchrotron techniques<sup>243</sup> have provided useful capabilities and new insight in terms of operando detail and understanding of critical

processes in batteries and electrochemical materials science. However, they do not readily translate into real-time monitoring of batteries in the field because of the nature of the infrastructural requirements. These methods do provide very detailed and powerful ways of assessing material and cell-chemistry behavior in real-time. Methods that will allow detection, in real-time, of the complex combination of intended chemical and electrochemical processes and of the panoply of side reactions that significantly affect long-term performance will be useful and complement synchrotron-based methods when used for material prediction, screening, and safety diagnostics. This could facilitate the materials science, chemistry, electrochemistry, and battery communities to optimize cycling regimes or identify failure mechanisms more rapidly.

Battery history can then be determined and a health “check-up” be performed, allowing appropriate pricing and insurance for a battery as it enters its second-life application. Grid and transport demonstration projects and battery tests are already in progress to link traditional electrochemical responses (such as current, voltage, and impedance) with test routines appropriate to the technology and produce the “big data” needed to extract new correlations and, ultimately, predict future performance. Current examples at the time of writing are large-scale European projects under the Battery2030+ initiative that is focused on real-time, passive, and other methods to monitor battery performance, safety, and cell health. An inside-the-battery-material analogue of today’s battery management systems would prove useful too. Deriving useful information from the thousands of batteries used commercially via data-driven consumer apps and coordinated mapping of testing procedures from lab-based tests of new systems are ways being investigated now to obtain a big-data map of all that affect batteries and battery components. The details of these larger scale, forward looking initiatives are outside the scope of this review and the reader is directed to available internet resources on these initiatives.<sup>244–250</sup> Diagnostics are required that can couple electronic with chemical traceability and can identify key reactions that are critical to both short- and long-term cell failure.

These methods will be vital for Na-ion, solid state batteries, and related battery formulations as well as many electrochemical systems where solid–solution interfaces are common and where dynamic processes in materials control and affect the nature of their response and behavior. Li-ion technologies are now proven from data to in principle power an EV for a “million miles,” a reference to seminal work by Dahn and co-workers,<sup>251</sup> where crystalline  $\text{Li}[\text{Ni}_{0.5}\text{Mn}_{0.3}\text{Co}_{0.2}]\text{O}_2$  (NMC532) cathodes and balanced artificial graphite cell were demonstrated. The cells used in that study were never turned off and are still cycling at the time of writing to many tens of thousands of cycles within the optimized voltage window. Similar cells are also developed with long life, with suggestions of a century of operation<sup>252</sup> based on exceptional long life characterization at the time of writing. The same group have also demonstrated that an ionic liquid electrolyte and choice voltage window can allow similar cells to run for effectively more than a century at 25 °C, and state-of-the-art stability and longevity at extremely high (~70 °C and higher) temperatures.<sup>252</sup> As Na-ion is now becoming commercially available, screening, prediction and real-time analysis will be essential in its future to fast-track its developments, performance, and safety. Safety matters will always be obviously important and leveraging many of these techniques as predictive or real-time monitoring methods in test and also in commercial

battery systems with communication functionality to the user will be key components that help battery technology users, such as EV drivers, to better understand the battery and its health, as much as has been learned by users of internal combustion engine (ICE) equivalents.

Ultimately, big-data analysis and prediction of battery behavior and new materials, together with large-scale high-resolution operando methods with built-in analytical sensors in consumer batteries will form a trifecta of analysis that can help to optimize existing and future battery use and development beyond Li-ion, and of course for many other areas in the electrochemical and solid-state science and technology sectors.

## ACKNOWLEDGMENTS

We acknowledge support from the Irish Research Council Advanced Laureate Award under Grant No. IRCLA/2019/118.

## AUTHOR DECLARATIONS

### Conflict of Interest

The authors have no conflicts to disclose.

## Author Contributions

**Alex Grant:** Conceptualization (equal); Data curation (lead); Methodology (equal); Validation (equal); Writing – original draft (lead); Writing – review & editing (supporting). **Colm O’Dwyer:** Conceptualization (equal); Data curation (supporting); Funding acquisition (lead); Methodology (equal); Project administration (equal); Supervision (lead); Writing – original draft (supporting); Writing – review & editing (lead).

## DATA AVAILABILITY

Data sharing is not applicable to this article as no new data were created or analyzed in this study.

## REFERENCES

- <sup>1</sup>M. S. Whittingham, *Chem. Rev.* **114**, 11414 (2014).
- <sup>2</sup>Y. Li, Q. Zhou, S. Weng, F. Ding, X. Qi, J. Lu, Y. Li, X. Zhang, X. Rong, Y. Lu, X. Wang, R. Xiao, H. Li, X. Huang, L. Chen, and Y.-S. Hu, *Nat. Energy* **7**, 511 (2022).
- <sup>3</sup>B. Yin, S. Liang, D. Yu, B. Cheng, I. L. Egun, J. Lin, X. Xie, H. Shao, H. He, and A. Pan, *Adv. Mater.* **33**, 2100808 (2021).
- <sup>4</sup>M. A. Rahman, X. Wang, and C. Wen, *J. Electrochem. Soc.* **160**, A1759 (2013).
- <sup>5</sup>L. Ma, T. Yu, E. Tzoganakis, K. Amine, T. Wu, Z. Chen, and J. Lu, *Adv. Energy Mater.* **8**, 1800348 (2018).
- <sup>6</sup>Y. X. Ren, L. Zeng, H. R. Jiang, W. Q. Ruan, Q. Chen, and T. S. Zhao, *Nat. Commun.* **10**, 3249 (2019).
- <sup>7</sup>Z. Shen, X. Jin, J. Tian, M. Li, Y. Yuan, S. Zhang, S. Fang, X. Fan, W. Xu, H. Lu, J. Lu, and H. Zhang, *Nat. Catal.* **5**, 555 (2022).
- <sup>8</sup>Y. Liang, H. Dong, D. Aurbach, and Y. Yao, *Nat. Energy* **5**, 646 (2020).
- <sup>9</sup>D. Chao, W. Zhou, F. Xie, C. Ye, H. Li, M. Jaroniec, and S.-Z. Qiao, *Sci. Adv.* **6**, eaba4098 (2020).
- <sup>10</sup>C. Zhu, R. E. Usiskin, Y. Yu, and J. Maier, *Science* **358**, eaao2808 (2017).
- <sup>11</sup>O. Pecher, J. Carretero-González, K. J. Griffith, and C. P. Grey, *Chem. Mater.* **29**, 213 (2017).
- <sup>12</sup>M. Armand and J. Tarascon, *Nature* **414**, 359 (2001).
- <sup>13</sup>E. Pomerantseva, F. Bonaccorso, X. Feng, Y. Cui, and Y. Gogotsi, *Science* **366**, eaan8285 (2019).

- <sup>14</sup>N. Nitta, F. Wu, J. T. Lee, and G. Yushin, *Mater. Today* **18**, 252 (2015).
- <sup>15</sup>B. Key, R. Bhattacharyya, M. Morcrette, V. Seznéc, J.-M. Tarascon, and C. P. Grey, *J. Am. Chem. Soc.* **131**, 9239 (2009).
- <sup>16</sup>R. Bhattacharyya, B. Key, H. Chen, A. Best, A. Hollenkamp, and C. Grey, *Nat. Mater.* **9**, 504 (2010).
- <sup>17</sup>V. K. Peterson and L. Stievano, *Batteries Supercaps* **4**, 1789 (2021).
- <sup>18</sup>Y. Wu and N. Liu, *Chem* **4**, 438 (2018).
- <sup>19</sup>L. Mai, M. Yan, and Y. Zhao, *Nature* **546**, 469 (2017).
- <sup>20</sup>F. Blanc, M. Leskes, and C. P. Grey, *Acc. Chem. Res.* **46**, 1952 (2013).
- <sup>21</sup>S. Chandrashekar, N. M. Trease, H. J. Chang, L. S. Du, C. P. Grey, and A. Jerschow, *Nat. Mater.* **11**, 311 (2012).
- <sup>22</sup>M. Sathiy, M. Sathiy, M. Sathiy, M. Sathiy, M. Sathiy, and M. Sathiy, *Nat. Commun.* **6**, 6276 (2015).
- <sup>23</sup>D. X. Liu, L. Cao, and A. C. Co, *Chem. Mater.* **28**, 556 (2016).
- <sup>24</sup>D. X. Liu and A. C. Co, *J. Am. Chem. Soc.* **138**, 231 (2016).
- <sup>25</sup>D. X. Liu, J. Wang, P. Ke, J. Qiu, M. Canova, L. Cao, and A. C. Co, *Angew. Chem. Int. Ed.* **53**, 9498 (2014).
- <sup>26</sup>F. Wang, F. Wang, F. Wang, F. Wang, F. Wang, and F. Wang, *Nat. Commun.* **3**, 1201 (2012).
- <sup>27</sup>J. Y. Huang, L. Zhong, C. M. Wang, J. P. Sullivan, W. Xu, L. Q. Zhang, S. X. Mao, N. S. Hudak, X. H. Liu, A. Subramanian, H. Fan, L. Qi, A. Kushima, and J. Li, *Science* **330**, 1515 (2010).
- <sup>28</sup>S. C. Chao, S. C. Chao, S. C. Chao, S. C. Chao, S. C. Chao, and S. C. Chao, *Electrochem. Commun.* **12**, 234 (2010).
- <sup>29</sup>A. Ulvestad, A. Singer, J. N. Clark, H. M. Cho, J. W. Kim, R. Harder, J. Maser, Y. S. Meng, and O. G. Shpyrko, *Science* **348**, 6241 (2015).
- <sup>30</sup>A. Molinari, P. M. Leufke, C. Reitz, S. Dasgupta, R. Witte, R. Kruk, and H. Hahn, *Nat. Commun.* **8**, 15339 (2017).
- <sup>31</sup>C. Reitz, P. M. Leufke, R. Schneider, H. Hahn, and T. Brezesinski, *Chem. Mater.* **26**, 5745 (2014).
- <sup>32</sup>S.-H. Kim, S. Antonov, X. Zhou, L. T. Stephenson, C. Jung, A. A. El-Zoka, D. K. Schreiber, M. Conroy, and B. Gault, *J. Mater. Chem. A* **10**, 4926 (2022).
- <sup>33</sup>A. C. Marschilok, A. M. Bruck, A. Abraham, C. A. Stackhouse, K. J. Takeuchi, E. S. Takeuchi, M. Croft, and J. W. Gallaway, *Phys. Chem. Chem. Phys.* **22**, 20972 (2020).
- <sup>34</sup>W. Zhu, D. Liu, A. Paoletta, C. Gagnon, V. Gariépy, A. Vijh, and K. Zaghib, *Front. Energy Res.* **6**, 1 (2018).
- <sup>35</sup>Y. Xie, H. Wang, G. Xu, J. Wang, H. Sheng, Z. Chen, Y. Ren, C.-J. Sun, J. Wen, J. Wang, D. J. Miller, J. Lu, K. Amine, and Z.-F. Ma, *Adv. Energy Mater.* **6**, 1601306 (2016).
- <sup>36</sup>X.-M. Zheng, J.-H. You, J.-J. Fan, G.-P. Tu, W.-Q. Rong, W.-J. Li, Y.-X. Wang, S. Tao, P.-Y. Zhang, S.-Y. Zhang, S.-Y. Shen, J.-T. Li, L. Huang, and S.-G. Sun, *Nano Energy* **77**, 105123 (2020).
- <sup>37</sup>J. Zhang, L. Lai, H. Wang, M. Chen, and Z. X. Shen, *Mater. Today Energy* **21**, 100747 (2021).
- <sup>38</sup>Y. Yan, C. Cheng, L. Zhang, Y. Li, and J. Lu, *Adv. Energy Mater.* **9**, 1900148 (2019).
- <sup>39</sup>Y.-C. Chien, A. S. Menon, W. R. Brant, M. J. Lacey, and D. Brandell, *J. Phys. Chem. C* **126**, 2971 (2022).
- <sup>40</sup>J. B. Robinson, M. Maier, G. Alster, T. Compton, D. J. L. Brett, and P. R. Shearing, *Phys. Chem. Chem. Phys.* **21**, 6354 (2019).
- <sup>41</sup>K. Kirshenbaum, D. Bock, C.-Y. Lee, Z. Zhong, K. Takeuchi, A. Marschilok, and E. Takeuchi, *Science* **347**, 149 (2015).
- <sup>42</sup>R. D. Schmidt and J. Sakamoto, *J. Power Sources* **324**, 126 (2016).
- <sup>43</sup>W. Chang, C. Bommier, T. Fair, J. Yeung, S. Patil, and D. Steingart, *J. Electrochem. Soc.* **167**, 090503 (2020).
- <sup>44</sup>Z. Deng, Z. Huang, Y. Shen, Y. Huang, H. Ding, A. Luscombe, M. Johnson, J. E. Harlow, R. Gauthier, and J. R. Dahn, *Joule* **4**, 2017 (2020).
- <sup>45</sup>H. Liu, F. C. Strohbridge, O. J. Borkiewicz, K. M. Wiaderek, K. W. Chapman, P. J. Chupas, and C. P. Grey, *Science* **344**, 1252817 (2014).
- <sup>46</sup>X. Lu, A. Bertei, D. P. Finegan, C. Tan, S. R. Daemi, J. S. Weaving, K. B. O'Regan, T. M. M. Heenan, G. Hinds, E. Kendrick, D. J. L. Brett, and P. R. Shearing, *Nat. Commun.* **11**, 2079 (2020).
- <sup>47</sup>X. Lu, S. R. Daemi, A. Bertei, M. D. R. Kok, K. B. O'Regan, L. Rasha, J. Park, G. Hinds, E. Kendrick, D. J. L. Brett, and P. R. Shearing, *Joule* **4**, 2746 (2020).
- <sup>48</sup>J. Scharf, M. Chouchane, D. P. Finegan, B. Lu, C. Redquest, M. c. Kim, W. Yao, A. A. Franco, D. Gostovic, Z. Liu, M. Riccio, F. Zelenka, J.-M. Daux, and Y. S. Meng, *Nat. Nanotechnol.* **5**, 446 (2022).
- <sup>49</sup>J. Scharf, L. Yin, C. Redquest, R. Liu, X. L. Quinn, J. Ortega, X. Wei, J. Wang, J.-M. Daux, and Y. S. Meng, *Adv. Energy Mater.* **11**, 2101327 (2021).
- <sup>50</sup>O. J. Borkiewicz, B. Shyam, K. M. Wiaderek, C. Kurtz, P. J. Chupas, and K. W. Chapman, *J. Appl. Crystallogr.* **45**, 1261 (2012).
- <sup>51</sup>H. Liu, P. K. Allan, O. J. Borkiewicz, C. Kurtz, C. P. Grey, K. W. Chapman, and P. J. Chupas, *J. Appl. Crystallogr.* **49**, 1665 (2016).
- <sup>52</sup>Y.-N. Zhou, J.-L. Yue, E. Hu, H. Li, L. Gu, K.-W. Nam, S.-M. Bak, X. Yu, J. Liu, J. Bai, E. Dooryhee, Z.-W. Fu, and X.-Q. Yang, *Adv. Energy Mater.* **6**, 1600597 (2016).
- <sup>53</sup>Z. Yang, L. Trahey, Y. Ren, M. K. Y. Chan, C. Lin, J. Okasinski, and M. M. Thackeray, *J. Mater. Chem. A* **3**, 7389 (2015).
- <sup>54</sup>M. M. Storm, R. E. Johnsen, R. Younesi, and P. Norby, *J. Mater. Chem. A* **3**, 3113 (2015).
- <sup>55</sup>S. Waluś, C. Barchasz, R. Bouchet, J.-C. Lepêtre, J.-F. Colin, J.-F. Martin, E. Elkaim, C. Baetz, and F. Alloin, *Adv. Energy Mater.* **5**, 1500165 (2015).
- <sup>56</sup>K. P. C. Yao, J. S. Okasinski, K. Kalaga, I. A. Shkrob, and D. P. Abraham, *Energy Environ. Sci.* **12**, 656 (2019).
- <sup>57</sup>X. H. Liu, Y. Liu, A. Kushima, S. Zhang, T. Zhu, J. Li, and J. Y. Huang, *Adv. Energy Mater.* **2**, 722 (2012).
- <sup>58</sup>M. T. McDowell, I. Ryu, S. W. Lee, C. Wang, W. D. Nix, and Y. Cui, *Adv. Mater.* **24**, 6034 (2012).
- <sup>59</sup>S. Basak, K. Dzieciol, Y. E. Durmus, H. Tempel, H. Kungl, C. George, J. Mayer, and R.-A. Eichel, *Chem. Phys. Rev.* **3**, 031303 (2022).
- <sup>60</sup>Z. Zeng, W.-I. Liang, H.-G. Liao, H. L. Xin, Y.-H. Chu, and H. Zheng, *Nano Lett.* **14**, 1745 (2014).
- <sup>61</sup>M. E. Holtz, Y. Yu, D. Gunceler, J. Gao, R. Sundaraman, K. A. Schwarz, T. A. Arias, H. D. Abruña, and D. A. Muller, *Nano Lett.* **14**, 1453 (2014).
- <sup>62</sup>M. Gu, L. R. Parent, B. L. Mehdi, R. R. Unocic, M. T. McDowell, R. L. Sacci, W. Xu, J. G. Connell, P. Xu, P. Abellan, X. Chen, Y. Zhang, D. E. Perea, J. E. Evans, L. J. Laughton, J.-G. Zhang, J. Liu, N. D. Browning, Y. Cui, I. Arslan, and C.-M. Wang, *Nano Lett.* **13**, 6106 (2013).
- <sup>63</sup>F. Wu and N. Yao, *Nano Energy* **11**, 196 (2015).
- <sup>64</sup>H.-W. Lee, Y. Li, and Y. Cui, *Curr. Opin. Chem. Eng.* **12**, 37 (2016).
- <sup>65</sup>K. A. Taylor and R. M. Glaeser, *Science* **186**, 1036 (1974).
- <sup>66</sup>X. Wang, Y. Li, and Y. S. Meng, *Joule* **2**, 2225 (2018).
- <sup>67</sup>X. Wang, M. Zhang, J. Alvarado, S. Wang, M. Sina, B. Lu, J. Bouwer, W. Xu, J. Xiao, J.-G. Zhang, J. Liu, and Y. S. Meng, *Nano Lett.* **17**, 7606 (2017).
- <sup>68</sup>Y. Li, Y. Li, A. Pei, K. Yan, Y. Sun, C.-L. Wu, L.-M. Joubert, R. Chin, A. L. Koh, Y. Yu, J. Perrino, B. Butz, S. Chu, and Y. Cui, *Science* **358**, 506 (2017).
- <sup>69</sup>D. Aurbach, Y. Ein-Ely, and A. Zaban, *J. Electrochem. Soc.* **141**, L1 (1994).
- <sup>70</sup>R. F. Ziesche, T. Arlt, D. P. Finegan, T. M. M. Heenan, A. Tengattini, D. Baum, N. Kardjilov, H. Markötter, I. Manke, W. Kockelmann, D. J. L. Brett, and P. R. Shearing, *Nat. Commun.* **11**, 777 (2020).
- <sup>71</sup>B. Gault, A. Chiaramonti, O. Cojocaru-Mirédin, P. Stender, R. Dubosq, C. Freysoldt, S. Kumar Makineni, T. Li, M. Moody, and J. M. Cairney, *Nat. Rev. Methods Primers* **1**, 51 (2021).
- <sup>72</sup>A. N. Chiaramonti, L. Miaja-Avila, P. T. Blanchard, D. R. Diercks, B. P. Gorman, and N. A. Sanford, *MRS Adv.* **4**, 2367 (2019).
- <sup>73</sup>Z. Peng, F. Vurpillot, P.-P. Choi, Y. Li, D. Raabe, and B. Gault, *Ultramicroscopy* **189**, 54 (2018).
- <sup>74</sup>D. N. Seidman, *Annu. Rev. Mater. Res.* **37**, 127 (2007).
- <sup>75</sup>T. T. Tsong, *Surf. Sci.* **85**(1), 1 (1979).
- <sup>76</sup>B. Gault, A. La Fontaine, M. P. Moody, S. P. Ringer, and E. A. Marquis, *Ultramicroscopy* **110**, 1215 (2010).
- <sup>77</sup>S. K. Sundaram and E. Mazur, *Nat. Mater.* **1**, 217 (2002).
- <sup>78</sup>J. Houard, A. Vella, F. Vurpillot, and B. Deconihout, *Phys. Rev. B* **84**, 033405 (2011).
- <sup>79</sup>M. Müller, D. Saxey, G. Smith, and B. Gault, *Ultramicroscopy* **111**, 487 (2011).
- <sup>80</sup>I. E. McCarroll, P. A. J. Bagot, A. Devaraj, D. E. Perea, and J. M. Cairney, *Mater. Today Adv.* **7**, 100090 (2020).
- <sup>81</sup>A. Devaraj, C. Szymanski, P. Yan, C. M. Wang, V. Murgesan, J. M. Zheng, J. Zhang, T. Tyliczszak, and S. Thevuthasan, *Microsc. Microanal.* **21**, 685 (2015).
- <sup>82</sup>B. Gault and J. D. Poplawsky, *Nat. Commun.* **12**, 3740 (2021).
- <sup>83</sup>D. Santhanagopalan, D. K. Schreiber, D. E. Perea, R. L. Martens, Y. Janssen, P. Khalifah, and Y. S. Meng, *Ultramicroscopy* **148**, 57 (2015).



- <sup>84</sup>A. Devaraj, R. Colby, W. P. Hess, D. E. Perea, and S. Thevuthasan, *J. Phys. Chem. Lett.* **4**, 993 (2013).
- <sup>85</sup>Y. Zhang, J. A. Alarco, A. S. Best, G. A. Snook, P. C. Talbot, and J. Y. Nerkar, *RSC Adv.* **9**, 1134 (2019).
- <sup>86</sup>C. Dette, M. A. Pérez-Osorio, C. S. Kley, P. Punke, C. E. Patrick, P. Jacobson, F. Giustino, S. J. Jung, and K. Kern, *Nano Lett.* **14**, 6533 (2014).
- <sup>87</sup>X. H. Liu, S. Huang, S. T. Picraux, J. Li, T. Zhu, and J. Y. Huang, *Nano Lett.* **11**, 3991 (2011).
- <sup>88</sup>S. Lee, Y. Oshima, E. Hosono, H. Zhou, K. Kim, H. M. Chang, R. Kanno, and K. Takayanagi, *ACS Nano* **9**, 626 (2015).
- <sup>89</sup>Y. Gong, J. Zhang, L. Jiang, J.-A. Shi, Q. Zhang, Z. Yang, D. Zou, J. Wang, X. Yu, R. Xiao, Y.-S. Hu, L. Gu, H. Li, and L. Chen, *J. Am. Chem. Soc.* **139**, 4274 (2017).
- <sup>90</sup>J. Maier, B. Pfeiffer, C. A. Volkert, and C. Nowak, *Energy Technol.* **4**, 1565 (2016).
- <sup>91</sup>L. Meyer, N. Saqib, and J. Porter, *J. Electrochem. Soc.* **168**, 090561 (2021).
- <sup>92</sup>V. Stancovski and S. Badilescu, *J. Appl. Electrochem.* **44**, 23 (2014).
- <sup>93</sup>P. Jiang, J. F. Bertone, K. S. Hwang, and V. L. Colvin, *Chem. Mater.* **11**, 2132 (1999).
- <sup>94</sup>E. Armstrong, D. McNulty, H. Geaney, and C. O'Dwyer, *ACS Appl. Mater. Interfaces* **7**, 27006 (2015).
- <sup>95</sup>L. Mai, Y. Dong, L. Xu, and C. Han, *Nano Lett.* **10**, 4273 (2010).
- <sup>96</sup>Y. Akita, M. Segawa, H. Munakata, and K. Kanamura, *J. Power Sources* **239**, 175 (2013).
- <sup>97</sup>A. Mauger and C. M. Julien, *AIMS Mater. Sci.* **5**, 349 (2018).
- <sup>98</sup>H. Nakagawa, Y. Domi, T. Doi, M. Ochida, S. Tsubouchi, T. Yamanaka, T. Abe, and Z. Ogumi, *J. Power Sources* **206**, 320 (2012).
- <sup>99</sup>W. Zhu, A. Paoletta, C. S. Kim, D. Liu, Z. Feng, C. Gagnon, J. Trottier, A. Vjih, A. Guerfi, A. Mauger, C. M. Julien, M. Armand, and K. Zaghib, *Sustainable Energy Fuels* **1**, 737 (2017).
- <sup>100</sup>Z. Wei, A. Salehi, G. Lin, J. Hu, X. Jin, E. Agar, and F. Liu, *J. Power Sources* **449**, 227361 (2020).
- <sup>101</sup>Z. Gao, H. Sun, L. Fu, F. Ye, Y. Zhang, W. Luo, and Y. Huang, *Adv. Mater.* **30**, 1705702 (2018).
- <sup>102</sup>S. Randau, D. A. Weber, O. Kötz, R. Koerver, P. Braun, A. Weber, E. Ivers-Tiffée, T. Adermann, J. Kulisch, W. G. Zeier, F. H. Richter, and J. Janek, *Nat. Energy* **5**, 259 (2020).
- <sup>103</sup>X. Yao, D. Liu, C. Wang, P. Long, G. Peng, Y.-S. Hu, H. Li, L. Chen, and X. Xu, *Nano Lett.* **16**, 7148 (2016).
- <sup>104</sup>Y. Zhou, C. Doerrer, J. Kasemchainan, P. G. Bruce, M. Pasta, and L. J. Hardwick, *Batteries Supercaps* **3**, 647 (2020).
- <sup>105</sup>Y. Matsuda, N. Kuwata, T. Okawa, A. K. Dorai, O. Kamishima, and J. Kawamura, *Solid State Ionics* **335**, 7 (2019).
- <sup>106</sup>D. Liu, Z. Shadike, R. Lin, K. Qian, H. Li, K. Li, S. Wang, Q. Yu, M. Liu, S. Ganapathy, X. Qin, Q.-H. Yang, M. Wagemaker, F. Kang, X.-Q. Yang, and B. Li, *Adv. Mater.* **31**, 1806620 (2019).
- <sup>107</sup>Y. Deng, S. Dong, Z. Li, H. Jiang, X. Zhang, and X. Ji, *Small Methods* **2**, 1700332 (2018).
- <sup>108</sup>G. Collins, E. Armstrong, D. McNulty, S. O'Hanlon, H. Geaney, and C. O'Dwyer, *Sci. Technol. Adv. Mater.* **17**, 563 (2016).
- <sup>109</sup>D. McNulty, E. Carroll, and C. O'Dwyer, *Adv. Energy Mater.* **7**, 1602291 (2017).
- <sup>110</sup>E. Armstrong and C. O'Dwyer, *J. Mater. Chem. C* **3**, 6109 (2015).
- <sup>111</sup>G. Mayonado, S. Mian, V. Robbiano, and F. Cacialli, *Investigation of the Bragg-Snell Law in Photonic Crystals* (American Association of Physics Teachers, 2015).
- <sup>112</sup>J.-L. Xu, K. V. Thomas, Z. Luo, and A. A. Gowen, *TrAC Trends Anal. Chem.* **119**, 115629 (2019).
- <sup>113</sup>A. Götz, R. Nikzad-Langerodi, Y. Staedler, A. Bellaire, and J. Saukel, *Spectrochim. Acta, Part A* **224**, 117460 (2020).
- <sup>114</sup>J. Grdadolnik, *Acta Chim. Slov.* **49**, 631 (2002).
- <sup>115</sup>F. Shi, P. N. Ross, G. A. Somorjai, and K. Komvopoulos, *J. Phys. Chem. C* **121**, 14476 (2017).
- <sup>116</sup>S. G. Kazarian and K. L. Chan, *Analyst* **138**, 1940 (2013).
- <sup>117</sup>C. Marino, A. Boulaoued, J. Fullenwarth, D. Maurin, N. Louvain, J.-L. Bantignies, L. Stievano, and L. Monconduit, *J. Phys. Chem. C* **121**, 26598 (2017).
- <sup>118</sup>D. Alves Dalla Corte, G. Caillon, C. Jordy, J.-N. Chazalviel, M. Rosso, and F. Ozanam, *Adv. Energy Mater.* **6**, 1501768 (2016).
- <sup>119</sup>W. Ren, X. Chen, and C. Zhao, *Adv. Energy Mater.* **8**, 1801413 (2018).
- <sup>120</sup>S. A. Freunberger, Y. Chen, N. E. Drewett, L. J. Hardwick, F. Bardé, and P. G. Bruce, *Angew. Chem. Int. Ed.* **50**, 8609 (2011).
- <sup>121</sup>J. Manuel, T. Salguero, and R. P. Ramasamy, *J. Appl. Electrochem.* **49**, 529 (2019).
- <sup>122</sup>T. Köhler, J. Hanzig, and V. Koroteev, *Phys. Sci. Rev.* **4**, 20170154 (2019).
- <sup>123</sup>D. McNulty, H. Geaney, E. Armstrong, and C. O'Dwyer, *J. Mater. Chem. A* **4**, 4448 (2016).
- <sup>124</sup>S. Chiluwal, A. M. Rao, and R. Podila, *Nanotechnol. Rev.* **10**, 1993 (2021).
- <sup>125</sup>C. O'Dwyer, *Adv. Mater.* **28**, 5681 (2016).
- <sup>126</sup>V. N. Astratov, Y. A. Vlasov, O. Z. Karimov, A. A. Kaplyanskii, Y. G. Musikhin, N. A. Bert, V. N. Bogomolov, and A. V. Prokofiev, *Phys. Lett. A* **222**, 349 (1996).
- <sup>127</sup>K. Köhler and S. John, *Phys. Rev. E* **58**, 3896 (1998).
- <sup>128</sup>C. Cheng, A. Scherer, R.-C. Tyan, Y. Fainman, G. Witzgall, and E. Yablonovitch, *J. Vac. Sci. Technol., B* **15**, 2764 (1997).
- <sup>129</sup>D. Gaillot and T. Yamashita, *Phys. Rev. B* **72**, 205109 (2005).
- <sup>130</sup>S. A. Asher, J. M. Weissman, A. Tikhonov, R. D. Coalson, and R. Kesavamoorthy, *Phys. Rev. E* **69**, 066619 (2004).
- <sup>131</sup>V. Golubev, *Phys. Rev. B* **72**, 205417 (2005).
- <sup>132</sup>W. Wu, M. Wang, J. Ma, Y. Cao, and Y. Deng, *Adv. Electron. Mater.* **4**, 1800185 (2018).
- <sup>133</sup>T. Kuno, Y. Matsumura, K. Nakabayashi, and M. Atobe, *Angew. Chem. Int. Ed.* **55**, 2503 (2016).
- <sup>134</sup>S.-L. Kuai, G. Bader, and P. V. Ashrit, *Appl. Phys. Lett.* **86**, 221110 (2005).
- <sup>135</sup>D. McNulty, H. Geaney, and C. O'Dwyer, *Sci. Rep.* **7**, 42263 (2017).
- <sup>136</sup>D. McNulty, H. Geaney, E. Carroll, S. Garvey, A. Lonergan, and C. O'Dwyer, *Mater. Res. Express* **4**, 025011 (2017).
- <sup>137</sup>A. Esmanski and G. A. Ozin, *Adv. Funct. Mater.* **19**, 1999 (2009).
- <sup>138</sup>J.-H. Kim, S. H. Kang, K. Zhu, J. Y. Kim, N. R. Neale, and A. J. Frank, *Chem. Commun.* **47**, 5214 (2011).
- <sup>139</sup>B. Ding, M. Pemble, A. Korovin, U. Peschel, and S. Romanov, *Phys. Rev. B* **82**, 065119 (2010).
- <sup>140</sup>Z.-Y. Li and Z.-Q. Zhang, *Phys. Rev. B* **62**, 1516 (2000).
- <sup>141</sup>A. Lonergan, D. McNulty, and C. O'Dwyer, *J. Appl. Phys.* **124**, 095106 (2018).
- <sup>142</sup>S. Romanov, H. Yates, M. Pemble, and R. De La Rue, *J. Phys.: Condens. Matter* **12**, 8221 (2000).
- <sup>143</sup>S. G. Romanov, A. V. Fokin, V. Y. Butko, N. P. Johnson, H. M. Yates, M. E. Pemble, and C. M. S. Torres, *Opal-Based Photonic Crystals: Control of the Optical Properties by Modifying the Dielectric Nature of the Structure* (IEEE, 1997), p. 527.
- <sup>144</sup>R. K. Cersonsky, J. Antonaglia, B. D. Dice, and S. C. Glotzer, *Nat. Commun.* **12**, 2543 (2021).
- <sup>145</sup>K. Busch and S. John, *Phys. Rev. Lett.* **83**, 967 (1999).
- <sup>146</sup>Y. Nishijima, K. Ueno, S. Juodkazis, V. Mizeikis, H. Misawa, T. Tanimura, and K. Maeda, *Opt. Express* **15**, 12979 (2007).
- <sup>147</sup>K. R. Phillips, N. Vogel, Y. Hu, M. Kolle, C. C. Perry, and J. Aizenberg, *Chem. Mater.* **26**, 1622 (2014).
- <sup>148</sup>M. Lanata, M. Cherchi, A. Zappettini, S. M. Pietralunga, and M. Martinelli, *Opt. Mater.* **17**, 11 (2001).
- <sup>149</sup>Y. Meng, F. Liu, M. M. Umair, B. Ju, S. Zhang, and B. Tang, *Adv. Opt. Mater.* **6**, 1701351 (2018).
- <sup>150</sup>H. Chen, R. Lou, Y. Chen, L. Chen, J. Lu, and Q. Dong, *Drug Delivery* **24**, 775 (2017).
- <sup>151</sup>S. Kim, A. N. Mitropoulos, J. D. Spitzberg, D. L. Kaplan, and F. G. Omenetto, *Opt. Express* **21**, 8897 (2013).
- <sup>152</sup>W. Chen, Z. Meng, M. Xue, and J. Shea Kenneth, *Mol. Imprinting* **4**, 1 (2016).
- <sup>153</sup>W. S. Lee, T. Kang, S.-H. Kim, and J. Jeong, *Sensors* **18**, 307 (2018).
- <sup>154</sup>Y. S. Zhang, C. Zhu, and Y. Xia, *Adv. Mater.* **29**, 1701115 (2017).
- <sup>155</sup>C. López, *Adv. Mater.* **15**, 1679 (2003).
- <sup>156</sup>S. Amrehn, X. Wu, C. Schumacher, and T. Wagner, *Physica Status Solidi A* **212**, 1266 (2015).
- <sup>157</sup>M. Danaie and B. Kiani, *Photonics Nanostruct.—Fundam. Appl.* **31**, 89 (2018).
- <sup>158</sup>A. Cumbo, B. Lorber, P. F. X. Corvini, W. Meier, and P. Shahgaldian, *Nat. Commun.* **4**, 1503 (2013).

- <sup>159</sup>A. Chutinan, N. P. Kherani, and S. Zukotynski, *Opt. Express* **17**, 8871 (2009).
- <sup>160</sup>K. Xie, M. Guo, and H. Huang, *J. Mater. Chem. C* **3**, 10665 (2015).
- <sup>161</sup>Y. Yu *et al.*, *Nano Lett.* **15**, 4282 (2015).
- <sup>162</sup>F. C. Strobbridge *et al.*, *Chem. Mater.* **27**, 2374 (2015).
- <sup>163</sup>A. Senyshyn, M. J. Mühlbauer, K. Nikolowski, T. Pirling, and H. Ehrenberg, *J. Power Sources* **203**, 126 (2012).
- <sup>164</sup>K. Ogata *et al.*, *Nat. Commun.* **5**, 3217 (2014).
- <sup>165</sup>B. R. Long, M. K. Y. Chan, J. P. Greeley, and A. A. Gewirth, *J. Phys. Chem. C* **115**, 18916 (2011).
- <sup>166</sup>K. Hongyou, T. Hattori, Y. Nagai, T. Tanaka, H. Nii, and K. Shoda, *J. Power Sources* **243**, 72 (2013).
- <sup>167</sup>A. Vu, Y. Q. Qian, and A. Stein, *Adv. Energy Mater.* **2**, 1056 (2012).
- <sup>168</sup>E. Armstrong, M. Osiak, H. Geaney, C. Glynn, and C. O'Dwyer, *CrystEngComm* **16**, 10804 (2014).
- <sup>169</sup>M. J. Armstrong, D. M. Burke, T. Gabriel, C. O'Regan, C. O'Dwyer, N. Petkov, and J. D. Holmes, *J. Mater. Chem. A* **1**, 12568 (2013).
- <sup>170</sup>C. O'Dwyer, V. Lavayen, D. A. Tanner, S. B. Newcomb, E. Benavente, G. Gonzalez, and C. M. Sotomayor Torres, *Adv. Funct. Mater.* **19**, 1736 (2009).
- <sup>171</sup>F. Wang, L. Feng, Y. Qin, T. Zhao, H. Luo, and J. Zhu, *J. Mater. Chem. C* **7**, 11972 (2019).
- <sup>172</sup>P. Ladpli, F. Kopsaftopoulos, R. Nardari, and F.-K. Chang, "Battery charge and health state monitoring via ultrasonic guided-wave-based methods using built-in piezoelectric transducers," *Proc. SPIE* **10171**, 1017107 (2017).
- <sup>173</sup>A. Navid and L. Pilon, *Thin Solid Films* **516**, 4159 (2008).
- <sup>174</sup>N. J. Hutchinson, T. Coquil, A. Navid, and L. Pilon, *Thin Solid Films* **518**, 2141 (2010).
- <sup>175</sup>A. Lonergan, C. Hu, and C. O'Dwyer, *Phys. Rev. Mater.* **4**, 065201 (2020).
- <sup>176</sup>L. Mishchenko, B. Hatton, M. Kolle, and J. Aizenberg, *Small* **8**, 1904 (2012).
- <sup>177</sup>P. V. Braun, *Chem. Mater.* **26**, 277 (2013).
- <sup>178</sup>E. Armstrong, W. Khunsin, M. Osiak, M. Blömker, C. M. S. Torres, and C. O'Dwyer, *Small* **10**, 1895 (2014).
- <sup>179</sup>C. O'Dwyer, M. Szachowicz, G. Visimberga, V. Lavayen, S. B. Newcomb, and C. M. S. Torres, *Nat. Nanotechnol.* **4**, 239 (2009).
- <sup>180</sup>M. Osiak, W. Khunsin, E. Armstrong, T. Kennedy, C. M. S. Torres, K. M. Ryan, and C. O'Dwyer, *Nanotechnology* **24**, 065401 (2013).
- <sup>181</sup>W. Zhang, M. Anaya, G. Lozano, M. E. Calvo, M. B. Johnston, H. Míguez, and H. J. Snaith, *Nano Lett.* **15**, 1698 (2015).
- <sup>182</sup>A. Ghannoum, R. C. Norris, K. Iyer, L. Zdravkova, A. Yu, and P. Nieva, *ACS Appl. Mater. Interfaces* **8**, 18763 (2016).
- <sup>183</sup>A. Ghannoum and P. Nieva, *J. Energy Storage* **28**, 101233 (2020).
- <sup>184</sup>J. Hedman, D. Nilebo, E. Larsson Langhammer, and F. Björefors, *ChemSusChem* **13**, 5731 (2020).
- <sup>185</sup>D. Krotkov, D. Schneider, S. Menkin, Y. Horowitz, E. Peled, D. Golodnitsky, and S. Fleischer, *Batteries Supercaps* **5**, e20100183 (2022).
- <sup>186</sup>M. E. Layani-Tzadka, D. Krotkov, E. Tirosh, G. Markovich, and S. Fleischer, *Nanotechnology* **30**, 215702 (2019).
- <sup>187</sup>K. S. C. Kuang, R. Kenny, M. P. Whelan, W. J. Cantwell, and P. R. Chalker, *Compos. Sci. Technol.* **61**, 1379 (2001).
- <sup>188</sup>L. Alberio Blanquer, F. Marchini, J. R. Seitz, N. Daher, F. Bétermier, J. Huang, C. Gervillie, and J.-M. Tarascon, *Nat. Commun.* **13**, 1153 (2022).
- <sup>189</sup>J. Huang, L. Alberio Blanquer, J. Bonefacino, E. R. Logan, D. Alves Dalla Corte, C. Delacourt, B. M. Gallant, S. T. Boles, J. R. Dahn, H.-Y. Tam, and J.-M. Tarascon, *Nat. Energy* **5**, 674 (2020).
- <sup>190</sup>J. A. Guemes and J. M. Menéndez, *Compos. Sci. Technol.* **62**, 959 (2002).
- <sup>191</sup>A. J. Louli, L. D. Ellis, and J. R. Dahn, *Joule* **3**, 745 (2019).
- <sup>192</sup>C. J. Bae, A. Manandhar, P. Kiesel, and A. Raghavan, *Energy Technol.* **4**, 851 (2016).
- <sup>193</sup>Y. D. Su, Y. Preger, H. Burroughs, C. Sun, and P. R. Ohodnicki, *Sensors* **21**, 1397 (2021).
- <sup>194</sup>X. Cheng and M. Pecht, *Energies* **10**, 591 (2017).
- <sup>195</sup>A. Bertholds and R. Dandliker, *J. Lightwave Technol.* **6**, 17 (1988).
- <sup>196</sup>Y. Wang, B. Yun, N. Chen, and Y. Cui, *Meas. Sci. Technol.* **17**, 939 (2006).
- <sup>197</sup>R. Gafsi and M. A. El-Sherif, *Opt. Fiber Technol.* **6**, 299 (2000).
- <sup>198</sup>M. Inaba, H. Yoshida, and Z. Ogumi, *J. Electrochem. Soc.* **143**, 2572 (1996).
- <sup>199</sup>A. Vizintin, J. Bitenc, A. Kopač Lautar, K. Pirnat, J. Grdadolnik, J. Stare, A. Randon-Vitanova, and R. Dominko, *Nat. Commun.* **9**, 661 (2018).
- <sup>200</sup>M. Matsui, S. Deguchi, H. Kuwata, and N. Imanishi, *Electrochemistry* **83**, 874 (2015).
- <sup>201</sup>R. Sharabi, E. Markevich, V. Borgel, G. Salitra, D. Aurbach, G. Semrau, and M. A. Schmidt, *Electrochem. Solid-State Lett.* **13**, A32 (2010).
- <sup>202</sup>A. Ghannoum, K. Iyer, P. Nieva, and A. Khajepour, "Fiber optic monitoring of lithium-ion batteries: a novel tool to understand the lithiation of batteries," in *IEEE Sensors* (IEEE, 2016), p. 1.
- <sup>203</sup>M. Patel, R. Demir-Cakan, M. Morcrette, J.-M. Tarascon, M. Gaberscek, and R. Dominko, *ChemSusChem* **6**, 1177 (2013).
- <sup>204</sup>K. Yue, C. Zhai, S. Gu, Y. He, J. Yeo, and G. Zhou, *Electrochim. Acta* **368**, 137535 (2021).
- <sup>205</sup>P. Lanz, C. Villevieille, and P. Novak, *Electrochim. Acta* **109**, 426 (2013).
- <sup>206</sup>T. Gross, L. Giebler, and C. Hess, *Rev. Sci. Instrum.* **84**, 073109 (2013).
- <sup>207</sup>M. Inaba, Y. Iriyama, Z. Ogumi, Y. Todzuka, and A. Tasaka, *J. Raman Spectrosc.* **28**, 613 (1997).
- <sup>208</sup>K. Shen, Z. Wang, X. Bi, Y. Ying, D. Zhang, C. Jin, G. Hou, H. Cao, L. Wu, G. Zheng, Y. Tang, X. Tao, and J. Lu, *Adv. Energy Mater.* **9**, 1900260 (2019).
- <sup>209</sup>X. Xu, S. Wang, H. Wang, B. Xu, C. Hu, Y. Jin, J. Liu, and H. Yan, *J. Energy Storage* **13**, 387 (2017).
- <sup>210</sup>F. Wu, Y.-X. Yuan, X.-B. Cheng, Y. Bai, Y. Li, C. Wu, and Q. Zhang, *Energy Storage Mater.* **15**, 148 (2018).
- <sup>211</sup>L. Kong, Y. Xing, and M. G. Pecht, *IEEE Access* **6**, 8387 (2018).
- <sup>212</sup>Y. Wu, C. Zhang, Y. Yuan, Z. Wang, W. Shao, H. Wang, and X. Xu, *Langmuir* **29**, 14017 (2013).
- <sup>213</sup>X.-B. Cheng, R. Zhang, C.-Z. Zhao, and Q. Zhang, *Chem. Rev.* **117**, 10403 (2017).
- <sup>214</sup>J. Liu, Z. Bao, Y. Cui, E. J. Dufek, J. B. Goodenough, P. Khalifah, Q. Li, B. Y. Liaw, P. Liu, A. Manthiram, Y. S. Meng, V. R. Subramanian, M. F. Toney, V. V. Viswanathan, M. S. Whittingham, J. Xiao, W. Xu, J. Yang, X.-Q. Yang, and J.-G. Zhang, *Nat. Energy* **4**, 180 (2019).
- <sup>215</sup>M. D. Tikekar, S. Choudhury, Z. Tu, and L. A. Archer, *Nat. Energy* **1**, 16114 (2016).
- <sup>216</sup>A. B. Gunnarsdóttir, C. V. Amanchukwu, S. Menkin, and C. P. Grey, *J. Am. Chem. Soc.* **142**, 20814 (2020).
- <sup>217</sup>R. Pigliapochi, S. Benders, E. V. Silletta, S. L. Glazier, E. Lee, J. Dahn, and A. Jerschow, *Batteries Supercaps* **4**, 322 (2020).
- <sup>218</sup>A. J. Iloft, M. Mohammadi, C. M. Schauerma, M. J. Ganter, and A. Jerschow, *Nat. Commun.* **9**, 1776 (2018).
- <sup>219</sup>A. L. Sukstanskii and D. A. Yablonskiy, *J. Magn. Reson.* **151**, 107 (2001).
- <sup>220</sup>E. Banguero, A. Correcher, Á. Pérez-Navarro, E. García, and A. Aristizabal, *Renewable Energy* **146**, 2438 (2020).
- <sup>221</sup>S. Tikole, V. Jaravine, V. Y. Orekhov, and P. Güntert, *PLoS One* **8**, e68567 (2013).
- <sup>222</sup>J.-H. Chen, H. Zhang, S. M. Althaus, and M. Boudjatit, *Fuel* **297**, 120777 (2021).
- <sup>223</sup>G. E. Möhl, E. Metwalli, and P. Müller-Buschbaum, *ACS Energy Lett.* **3**, 1525 (2018).
- <sup>224</sup>G. Subramania, R. Biswas, K. Constant, M. M. Sigalas, and K. M. Ho, *Phys. Rev. B* **63**, 235111 (2001).
- <sup>225</sup>D. McNulty, A. Lonergan, S. O'Hanlon, and C. O'Dwyer, *Solid State Ionics* **314**, 195 (2018).
- <sup>226</sup>V. Roscher and K. Riemschneider, *IEEE Trans. Instrum. Meas.* **67**, 735 (2018).
- <sup>227</sup>A. G. Hsieh, S. Bhadra, B. J. Hertzberg, P. J. Gjeltema, A. Goy, J. W. Fleischer, and D. A. Steingart, *Energy Environ. Sci.* **8**, 1569 (2015).
- <sup>228</sup>D. A. Steingart, in *Instrumentation and Measurement* (Physics World, 2020), Vol. 2020.
- <sup>229</sup>J. B. Robinson, M. Pham, M. D. R. Kok, T. M. M. Heenan, D. J. L. Brett, and P. R. Shearing, *J. Power Sources* **444**, 227318 (2019).
- <sup>230</sup>W. Chang, R. Mohr, A. Kim, A. Raj, G. Davies, K. Denner, J. H. Park, and D. Steingart, *J. Mater. Chem. A* **8**, 16624 (2020).
- <sup>231</sup>H.-S. Kitzerow, H. Matthias, S. L. Schweizer, H. M. van Driel, and R. B. Wehrspohn, *Adv. Opt. Technol.* **2008**, 780784.
- <sup>232</sup>R. Norris, K. Iyer, V. Chabot, P. Nieva, A. Yu, A. Khajepour, and J. Wang, "Multi-band reflectance spectroscopy of carbonaceous lithium iron phosphate battery electrodes versus state of charge," *Proc. SPIE* **8982**, 898214 (2014).
- <sup>233</sup>A. Messina, A. Greenstein, and A. Katzir, *Appl. Opt.* **35**, 2274 (1996).
- <sup>234</sup>J. M. Tarascon, A. S. Gozdz, C. Schmutz, F. Shokoohi, and P. C. Warren, *Solid State Ionics* **86–88**, 49 (1996).

- <sup>235</sup>M. Letellier, F. Chevallier, C. Clinard, E. Frackowiak, J.-N. Rouzaud, F. Béguin, M. Morcrette, and J.-M. Tarascon, *J. Chem. Phys.* **118**, 6038 (2003).
- <sup>236</sup>F. Chevallier, M. Letellier, M. Morcrette, J. M. Tarascon, E. Frackowiak, J. N. Rouzaud, and F. Béguin, *Electrochem. Solid-State Lett.* **6**, A225 (2003).
- <sup>237</sup>M. Letellier, F. Chevallier, F. Béguin, E. Frackowiak, and J.-N. Rouzaud, *J. Phys. Chem. Solids* **65**, 245 (2004).
- <sup>238</sup>F. Poli, J. S. Kshetrimayum, L. Monconduit, and M. Letellier, *Electrochem. Commun.* **13**, 1293 (2011).
- <sup>239</sup>G. Davies, K. W. Knehr, B. Van Tassell, T. Hodson, S. Biswas, A. G. Hsieh, and D. A. Steingart, *J. Electrochem. Soc.* **164**, A2746 (2017).
- <sup>240</sup>C. Bommier, W. Chang, Y. Lu, J. Yeung, G. Davies, R. Mohr, M. Williams, and D. Steingart, *Cell Rep. Phys. Sci.* **1**, 100035 (2020).
- <sup>241</sup>L. Gold, T. Bach, W. Virsik, A. Schmitt, J. Müller, T. E. M. Staab, and G. Sextl, *J. Power Sources* **343**, 536 (2017).
- <sup>242</sup>B. Li, C. M. Jones, T. E. Adams, and V. Tomar, *J. Power Sources* **486**, 229349 (2021).
- <sup>243</sup>J. McBreen, *J. Solid State Electrochem.* **13**, 1051 (2009).
- <sup>244</sup>J. Amici, P. Asinari, E. Ayerbe, P. Barboux, P. Bayle-Guillemaud, R. J. Behm, M. Bercibar, E. Berg, A. Bhowmik, S. Bodoardo, I. E. Castelli, I. Cekic-Laskovic, R. Christensen, S. Clark, R. Diehm, R. Dominko, M. Fichtner, A. A. Franco, A. Grimaud, N. Guillet, M. Hahlin, S. Hartmann, V. Heiries, K. Hermansson, A. Heuer, S. Jana, L. Jabbour, J. Kallo, A. Latz, H. Lorrmann, O. M. Løvvik, S. Lyonnard, M. Meeus, E. Paillard, S. Perraud, T. Placke, C. Punckt, O. Raccurt, J. Ruhland, E. Sheridan, H. Stein, J.-M. Tarascon, V. Trapp, T. Vegge, M. Weil, W. Wenzel, M. Winter, A. Wolf, and K. Edström, *Adv. Energy Mater.* **12**, 2102785 (2022).
- <sup>245</sup>D. Atkins, E. Ayerbe, A. Benayad, F. G. Capone, E. Capria, I. E. Castelli, I. Cekic-Laskovic, R. Ciria, L. Dudy, K. Edström, M. R. Johnson, H. Li, J. M. G. Lastra, M. L. De Souza, V. Meunier, M. Morcrette, H. Reichert, P. Simon, J.-P. Rueff, J. Sottmann, W. Wenzel, and A. Grimaud, *Adv. Energy Mater.* **12**, 2102687 (2022).
- <sup>246</sup>D. Atkins, E. Capria, K. Edström, T. Famprikis, A. Grimaud, Q. Jacquet, M. Johnson, A. Matic, P. Norby, H. Reichert, J.-P. Rueff, C. Villevieille, M. Wagemaker, and S. Lyonnard, *Adv. Energy Mater.* **12**, 2102694 (2022).
- <sup>247</sup>A. Benayad, D. Diddens, A. Heuer, A. N. Krishnamoorthy, M. Maiti, F. L. Cras, M. Legallais, F. Rahmanian, Y. Shin, H. Stein, M. Winter, C. Wölke, P. Yan, and I. Cekic-Laskovic, *Adv. Energy Mater.* **12**, 2102678 (2022).
- <sup>248</sup>A. Bhowmik, M. Bercibar, M. Casas-Cabanas, G. Csanyi, R. Dominko, K. Hermansson, M. R. Palacin, H. S. Stein, and T. Vegge, *Adv. Energy Mater.* **12**, 2102698 (2022).
- <sup>249</sup>M. Fichtner, K. Edström, E. Ayerbe, M. Bercibar, A. Bhowmik, I. E. Castelli, S. Clark, R. Dominko, M. Erakca, A. A. Franco, A. Grimaud, B. Horstmann, A. Latz, H. Lorrmann, M. Meeus, R. Narayan, F. Pammer, J. Ruhland, H. Stein, T. Vegge, and M. Weil, *Adv. Energy Mater.* **12**, 2102904 (2022).
- <sup>250</sup>J. Schaarschmidt, J. Yuan, T. Strunk, I. Kondov, S. P. Huber, G. Pizzi, L. Kahle, F. T. Bülle, I. E. Castelli, T. Vegge, F. Hanke, T. Hickel, J. Neugebauer, C. R. C. Rêgo, and W. Wenzel, *Adv. Energy Mater.* **12**, 2102638 (2022).
- <sup>251</sup>J. E. Harlow, X. Ma, J. Li, E. Logan, Y. Liu, N. Zhang, L. Ma, S. L. Glazier, M. M. E. Cormier, M. Genovese, S. Buteau, A. Cameron, J. E. Stark, and J. R. Dahn, *J. Electrochem. Soc.* **166**, A3031 (2019).
- <sup>252</sup>C. P. Aiken, E. R. Logan, A. Eldesoky, H. Hebecker, J. M. Oxner, J. E. Harlow, M. Metzger, and J. R. Dahn, *J. Electrochem. Soc.* **169**, 050512 (2022).